ABSTRACT

Title of Thesis: NEAR THRESHOLD SEDIMENT TRANSPORT BY A FORCED JET IMPINGING ON A MOBILE SEDIMENT BED

Kyle Corfman, Master of Science, 2015

Thesis directed by: Professor Kenneth Kiger
Department of Mechanical Engineering

Although sediment transport has been extensively studied in the past, flows such as rotorcraft brownout with large-scale coherent structures call many of the simplifying assumptions into question. The objective of this study is to develop a model for the prediction of sediment removal, referred to as erosion, based on independent measurements of the single-phase flow and the evolution of bedforms on the surface of a mobile sediment bed. A series of phase-resolved particle image velocimetry (PIV) flow measurements have been conducted to quantify the stress induced by an acoustically forced impinging jet, analagous to tip-vortices within the rotor wake. The threshold conditions for incipient particle motion are quantified through a series of PIV measurements of the single-phase flow at conditions found to produce quantifiable erosion of the surface. A force balance approach is used to develop a model, following the theory presented by Bagnold (1966), to predict the transport of sediment due to the stress above the theshold. A series of surface elevation measurements are analyzed to quantify the removal of sediment, for the

evaluation of the predicted model. An additional series of PIV measurements are performed on a prototype bedform, modeled after the observed bedforms, to quantify the changes in the flow field caused by their developement. The proposed model is shown to provide a better prediction of the observed erosion than classical sediment transport models, especially for cases close to the threshold conditions. For higher speed cases however, the model dramatically over predicts the observed erosion. Several physcially-based explanations are provided for this kink in the trend.

NEAR THRESHOLD SEDIMENT TRANSPORT BY A FORCED JET IMPINGING ON A MOBILE SEDIMENT BED

by

Kyle Corfman

Thesis submitted to the Faculty of the Graduate School of the
University of Maryland, College Park in partial fulfillment
of the requirements for the degree of
Master of Science
2015

Advisory Committee:
Dr. Kenneth Kiger, Chair/Advisor
Dr. Johan Larsson
Dr. Jim Duncan

Acknowledgments

I would like to sincerely thank my adivsor and professor, Dr. Ken Kiger for his guidance, advice, and patience throughout my education and research. His enthusiasm for research drew me into the field, and his experience and wisdom taught me how to excel within it. Working with him has been an honor and I cannot thank him enough for givng me this opporutnity. I would also like to thank Dr. Jim Duncan and Dr. Johan Larsson for their valuable time and constant mentorship through this process.

I would also like to thank my colleagues Jayson Geiser, Rahul Mulinti, Dana Ehyaei, Chang Liu, Farhad Saffaraval, Nate Washuta, Martin Erinin, An Wang, Naeem Masnadi, Ren Liu for their continuous support.

I would also like to thank my parents. Even though they cannot be here to share in this accomplishment, it was only possible with the values they instilled in me.

This work would not have been possible without the constant motivation and patience of my girlfriend, Rosie Myers. She has put up with countless late nights, turbulence lectures, and even helping me with some experiments.

Finally, I would like to thank the entire Mechanical Engineering Department at the University of Maryland. Over my 7 year career at the university there have been a number of people who have helped me, whether they be classmates, teachers, or adiministrators, and I would like to thank all of them.

Contents

List of Tables

List of Figures

Chapter 1: **Introduction**

The study of sediment transport aims to understand the motions of sediment particles and the surrounding fluid flow, as well as their interactions. As such it is already a complex, multi-dimensional, and multi-scale problem. The pimary focus of research in the field is to better understand geomorphological processes such as the movement of sand dunes, sedimentation within river beds, drifting of snow, or the erosion of beaches. The difficulty in studying these processes is that the mechanisms driving them are at the particle scale and are dependent on the unique flow surrounding it. For this reason, the early works on sediment transport were based on simple theoretical assumptions or empirical results and were focused on statistically steady open channel flows, for which the flow is well understood. However there exist many flows, both in nature and industy, which large-scale coherent vortices complicate the flow significantly.

One industrial application that exemplifies this phenomenon is rotorcraft brownout. Rotorcraft brownout is the development of a dust cloud surrounding a rotorcraft operating close to a mobile sediment surface by the intesne downwash wake. The problem with rotorcraft brownout is the suspension of sand and silt drastiaclly imapairs the pilots' visibility (Leishman (2008)). The downwash wake is comprised of larg-scale coherernt vortical filaments shed from the blade tips, which are comvected

downward by the rotor downwash and eventually interacting with the sediment surface. This interaction is though to be the primary mechanism in the formation of the brownout cloud, which poses a significant problem with the accurate prediction of the flow as most sediment transport models are based on assumptions of a statistically steady flow.

The objective of this study is to develop a model for the prediction of sediment transport in experimentally replicated brownout conditions. Though adapting a small-scale rotor is the most realistic approach, the vortices generated by a rotor are complex. To imporove the repeatability of the vortex/wall interaction, a prototype flow is generated by acoustically forcing an impinging jet, mainting the mean downwash and the coherent tip vortices. Although this flow maintains the primary features, it is nominally axisymmetric and not helical as in rotorcraft flow.

An emphasis is placed on the treatment of periodic large-scale vortices contained within the flow. The current models are generally based on assumptions of a fully-developed and steady flow, which have a predictable boundary layer. Assumptions like this may not be valid in a flow such as brownout with these coherent vortices, highlighting the need for a new model. In order to develop this model a series of separate measurements are performed to relate the stress induced by the vortex/wall interaction, the threshold stress required to mobilize the sediment, and the removal rate of sediment.

The induced fluid stress on the surface is quantified through a parametric study of nine different flow conditions, in the absence of the sediment particles. These are referred to as the single-phase flow conditions, and are divided into three groups:

1) a "dimensionally-similar" set, with a constant circulation and increasing mean flow; 2) a "self-similar" set, with a constant relationship between the circulation and the mean flow; and 3) a set with no external forcing and increasing mean flow. The comparison of the first two sets will shed light on the coupling effect of the mean flow and the entrained vortices and its implications for sediment transport. Comparing the last two will provide detail on the role the forcing plays in the sediment transport.

The threshold stress required to mobilize three different particles size classes is studied through a series of complimentray studies of each of the phases indepdently. The critical flow conditions are are found by gradually increasing the mean flow until particles begin to move. These flow conditions are then quantified through single-phase measurements, in order to obtain the critical stress threshold. These observed values will then be compared to some of the empirical models for predicting the threshold conditions.

The threshold stress and the induced stress by the nine flow conditions will be used to develop a model for the prediction of the transport of sediment. The model is developed following Bagnold's (1966) work transport rate method, which is reduced to a force balance between the weight of the particles and the excess stress imposed by the fluid. This model will show that typical averaging methods will under predict the transport rate by smearing out the coherent structures and suggest a new method for thresholding the stress.

The effect the bedforms have on the single-phase flow is quantified through PIV measurements of a single-phase flow on a prototype bedform. These results will be compared to the similar flow imposed on a flat plate.

The proposed model is then evaluated against observed erosion rates for each of the flows imposed on a mobile sediment bed. In order to obtain the erosion rates, a time sequence of surface elevation measurements are performed. These measurements will show the development of bedforms on the surface and their evolution in time. The difference in the surface elevation over time is converted to a bulk erosion rate, which can be compared to the rate predicted by the model.

Chapter 2: **Background and Motivation**

Although two-phase flows are common in nature and industry, there are large gaps in the current understanding of them. This chapter will provide a background in rotorcraft brownout and an overview of the basic concepts of multi-phase flows including the relevant parameters, the mechanisms involved in the transport of particles, and the approaches taken in predicting it. Several theoretical, numerical, and experimental approaches will be outlined. From this, the necessity for more advanced studies of the complex underlying physics of rotorcraft brownout will become evident.

2.1 Motivation

Rotorcraft downwash is a complex combination of a turbulent wall jet bounded by large vortical filaments shed from the blade tips. These filaments are convected downward by the mean flow from the blades, until they reach the ground. As the structures interact with the ground they undergo a series of complex interactions, including vortex pairing, rebound, particle/turbulence interactions, generation of three dimensional instabilities, and eventually viscous dissipation. The complexity of this interaction requires more detailed research into the mechanisms involved at the interface that drive the transport and suspension of particles, leading to the

development of the dust cloud (Figure 2.1).

Figure 2.1: Formation of a dust cloud in the landing zone, Johnson *et al.* (2010)

The dust cloud has costly implications to the operation and design or rotorcraft. The first concern is the loss the pilot's visibility. As the dust cloud envelopes the craft, the pilots visibility becomes severely impaired. This leads to a loss of visual queues and disorientation, reducing his/her ability to maneuver the craft safely. According to the Department of Defense estimates, rotorcraft brownout conditions are the leading cause of human related errors in rotorcraft operations, Couch and Lindell (2010). In addition to this, it has been found that fine sediment can remain in suspension long enough to be re-ingested by the prevailing flow, causing significant pitting damage on the blades and wear on engine components.

Although several mitigation techniques have been implemented with varying success, it is necessary to understand the root cause of the phenomenon to obtain a more feasible solution. Figure 2.2 shows a schematic of the complex mechanisms involved in the formation of the brownout cloud. Of these mechanisms, the most

complex is the saltation and scour casued by the vortex/wall interaction. As the tip vortices reach the sediment surface, the smallest particle sizes become completely suspended and potentially reingested in the rotor downwash. Slightly larger particles in this region can become suspended breifly before bombarding the surface. This bombardment causes more particles to be readily suspended, forming the sediment trapping region of the cloud. In the furthest outward region the tip vortices have largely disspated and the flow begins to resemble a wall-jet containing mostly bedload or groundwash transport mechanisms.

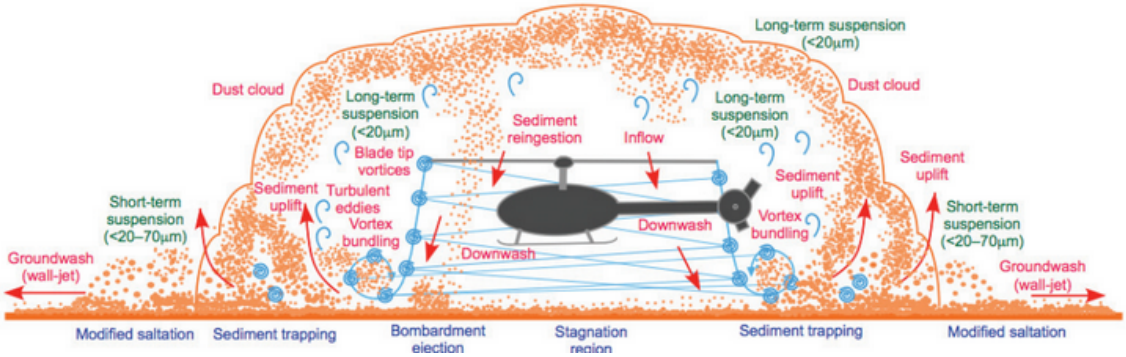

Figure 2.2: Schematic of the transport mechanisms of the brownout cloud, Syal (2012)

Rotorcraft flows are complicated further by the development of surface features caused by rapid erosion. The bed forms manifest at two predominant length scales. The first is the large scale crater produced by the spike in the stress under the vortex as it interacts with the sediment bed. The second is small scale streaks contained within the primary crater produced by instabilities caused by the three dimensionalization of the flow throughout the interaction. These surface features can be seen in Figure 2.3.

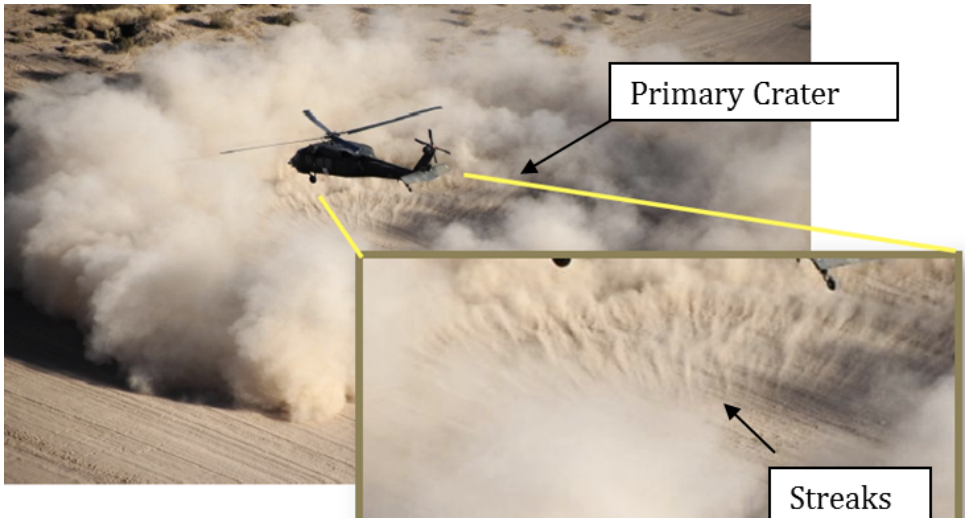

Figure 2.3: Schematic of the transport mechanisms of the brownout cloud, Johnson *et al.* (2010)

2.2 Sediment Transport from a Bed

Aeolian transport, transport of sand specifically by wind over dry land, is caused when the aerodynamic loads (lift and drag) on a single particle overcome its weight and interparticle cohesive forces. The presence of surrounding particles induces surface tension forces due to moisture within the bed, the particle size distribution and packing, and the van der Waals attractive forces. In combination with the weight of individual particles these forces lead to a threshold force, which must be exceeded by the aerodynamic loads in order for the particle to mobilize. The aerodynamic load can be divided into lift and drag. The lift forces, caused by a fluid velocity normal to the bed surface, encourage particles to enter into suspension. The drag forces, caused by the fluid velocity along the bed surface, result in particles being dragged or rolled along the surface. The relative magnitude and direction of these forces determine the trajectory a particle will take within the flow.

Based on the trajectory particles take the transport is characterized into one of three modes: 1) creep, in which particles roll along the surface; 2) saltation, in which particles are stochastic stress events suspend particles briefly leading to a bouncing trajectory but lift forces are not sufficient to fully suspend the particle; and 3) suspension, in which the particle becomes fully entrained in the flow. Although it is possible to separate these regimes theoretically, each provides unique challenges for experimental measurements. In creep flows, the near bed region of moving particles is difficult to measure because it is small and contains a relatively high concentration of particles. In saltating flows, the time and length scales of the stochastic stress events in the fluid are difficult to measure and are altered by the presence of the particles. In general, the presence of sediment particles renders most optical and acoustic measurement techniques inaccurate. For this reason, most early experiments used pitot tubes and suction samplers away from the bed surface. For measurements close to the bed, the bed load transport is measured by bed load traps.

2.3 Threshold Conditions for Motion

In sediment transport two important quantities are the buoyant weight and the bed shear stress. The weight of the particle encourages a particle to settle out of suspension. The bed shear stress is the primary mechanism of momentum transfer from the fluid to the particles causing them to mobilize. Shields (1936) proposed a non-dimensional number that describes the ratio of these forces, called the Shields

parameter:

$$\theta = \frac{\tau}{(\rho_p - \rho_f) g d_p} \tag{2.1}$$

Where ρ_f and ρ_p are the respective fluid and particle densities, g is the acceleration of gravity, d_p is the diameter of the particle, and τ is the bed shear stress. Shields proposed that there is a threshold value of this parameter above which, a particle will begin to move. The mechanism can be viewed as either a maximum of the bed shear stress a flow induces or as a minimum particle size that the flow can mobilize. Another important quantity for scaling is the friction Reynolds number:

$$Re_* = \frac{u_* d_p}{\nu} \tag{2.2}$$

Where u_* is the velocity just above the sediment bed surface, called the friction velocity, and ν is the kinematic viscosity of the fluid. Shields conducted channel flow experiments and fit a curve to show the relation between the θ_c and Re_* (Figure 2.4). The curve defines the range of flow velocities and particle sizes for which particle motion is possible.

In practice however, it is difficult to apply this empirical model for more complex flows because it relies on an accurate measure of u_*. In statistically steady flows, u_* can be accurately extrapolated based on a well-defined boundary layer. Wiggs *et al.* (2004) measured the onset of sediment transport on a beach due to natural winds and found that the time scale used for averaging the wind speed measurements can result in errors up to 30% in the value for u_*. They hypothesized

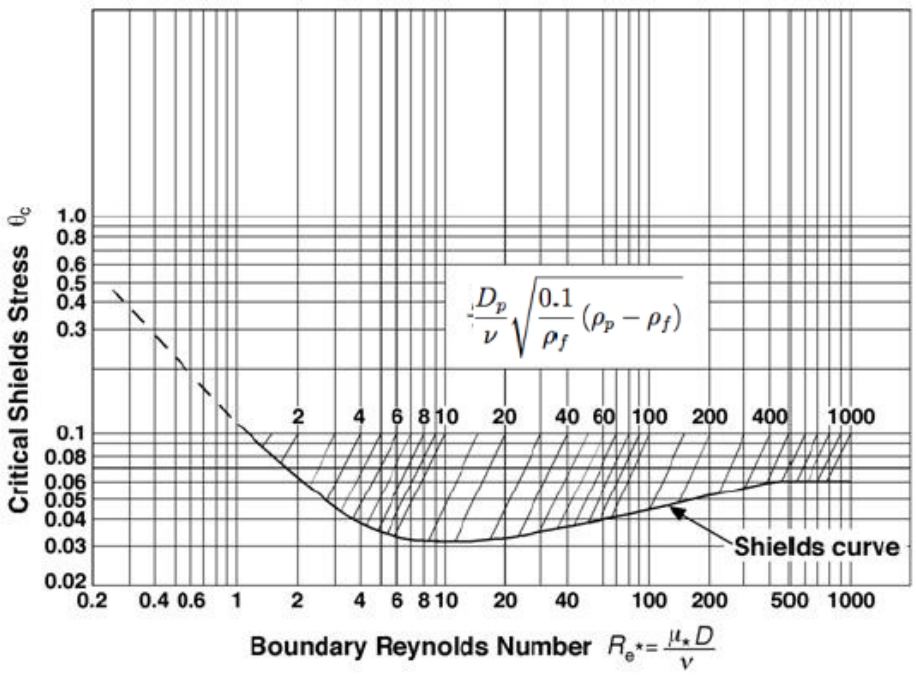

Figure 2.4: Shields curve for sediment transport Shields (1936)

that this indicated that the turbulent fluctuations were not captured by the coarse temporal resolution of the wind speed measurements. This severely limits the application of such threshold models in unsteady flows, such as brownout, where the structure of the boundary layer is not well known.

2.4 Sediment Transport Models

Once the threshold for motion has been exceeded, the sediment transport is classified into two modes based on the proximity to the bed. The first is bed-load transport (Q_b), which includes the region close to the bed and includes particles that are scouring, saltating, and rolling along the surface. In this relatively small region, the concentration of particles is high and the motion is dominated by the bed shear stress as well as the particle-bed interactions of saltation events. The second is

the suspended load (Q_s), which includes the particles that have become completely entrained in the flow. In this region the concentration is considerably lower than in the bed load region, and fluid velocity fluctuations become dominant. As the suspended concentration of particles increase, the particles require more momentum from the fluid to maintain suspension and thus they begin to augment or attenuate the fluid turbulence level. The total transport rate (Q_t) of particles is the summation of the suspended and bed-load transport rates.

Many studies have been performed to relate the transport rate to the bed shear stress. In general these models rely on the boundary layer assumptions used in Shields work, and take a piecewise form based on the threshold condition for motion. The piecewise nature of these models makes them very sensitive to measurements of the bed shear stress as well as the critical conditions for motion.

Meyer-Peter and Müller (1948) measured the bed-load transport rate in channel flows and found an empirical model relating the bed-load transport to the Shields parameter:

$$\phi = \begin{cases} m(\theta - \theta_c)^{\frac{3}{2}} & : \theta > \theta_c \\ 0 & : \theta \leq \theta_c \end{cases} \tag{2.3}$$

Where $m = 8$. Wilson (1966) conducted similar experiments for sheet flow conditions ($\theta > 0.8$) and found $m = 12$.

DuBoys (1879) took a theoretical approach to the bed-load transport, assuming that particles move in layers along the surface (Figure 2.5). Under equilibrium conditions the frictional resistance between the layers should balance with the trac-

tive shear stress by the fluid. This relation yields:

$$\tau = C_f m \epsilon (\gamma_p - \gamma) \tag{2.4}$$

Where C_f is the friction coefficient, m is the total number of layers, ϵ is the thickness of the layers, and γ_p and γ are the specific weights of the particles and the fluid respectively. DuBoys formulated the approach for water with a fixed depth, D.

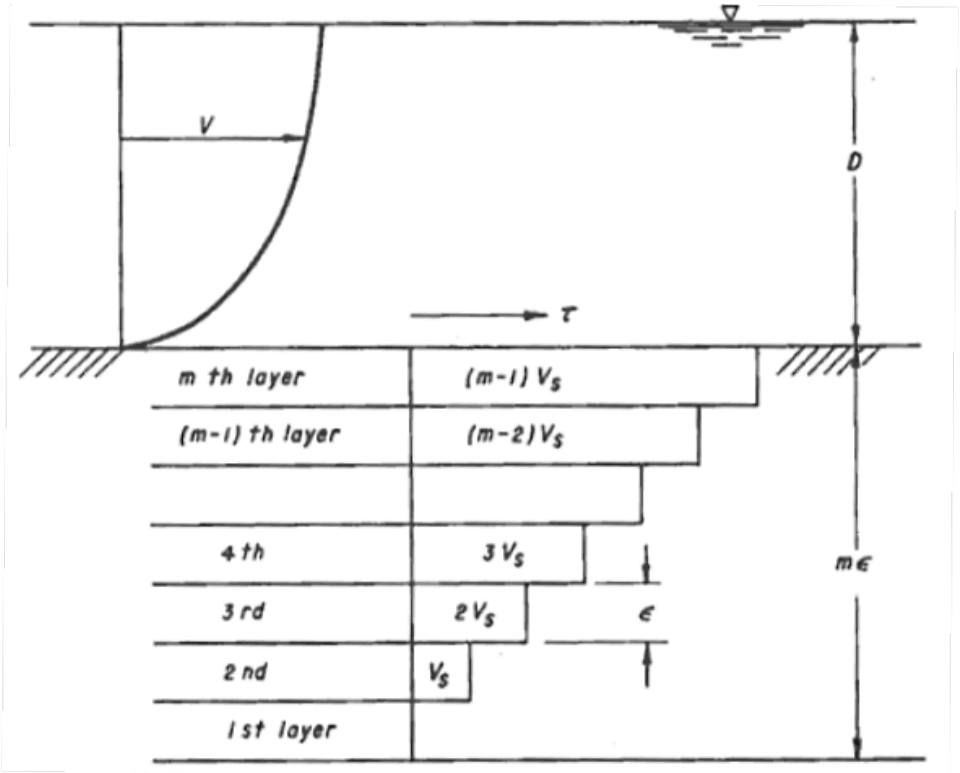

Figure 2.5: Schematic sketch of DuBoys' bed-load model, DuBoys (1879)

If the velocity of these layers varies linearly between the first and mth layer than the total bed load transport rate per unit channel width is:

$$q_b = \epsilon V_s \frac{m(m-1)}{2} \tag{2.5}$$

Where Vs is the velocity of second layer. At incipient motion ($m = 1$) equation 2.4 can be used to find that $m = \frac{\tau}{\tau_c}$. Combining this with equation 2.5 yields DuBoys' equation:

$$q_b = \frac{\epsilon V_s}{2\tau_c^2}\tau(\tau - \tau_c) = K\tau(\tau - \tau_c) \tag{2.6}$$

Where K is an empirical constant. Straub (1935) measured the bed load transport rate for channel flows and found that K varies with particle size. The application of this empirical model is limited however, because the relationship for K was found based on experiments with a relatively small range of particle sizes.

Einstein (1942) took a statistical approach, expressing the beginning and ceasing of transport in terms of probabilities. This approach had two major advantages over the previous formulations because the critical conditions for motion were avoided and the transport is related to the turbulent fluctuations rather than average values of stress imposed on the particles. Brown (1950) developed a bed load transport model based on the formula derived by Einstein:

$$q_b = 40\gamma_p K\left[g(\frac{\gamma_p}{\gamma} - 1)d_p^3\right]^{\frac{1}{2}}(\theta)^3 \tag{2.7}$$

where

$$K = \left[\frac{2}{3} + \frac{36\nu^2}{gd_p^3(\frac{\gamma_p}{\gamma} - 1)}\right]^{\frac{1}{2}} - \left[\frac{36\nu^2}{gd_p^3(\frac{\gamma_p}{\gamma} - 1)}\right]^{\frac{1}{2}} \tag{2.8}$$

2.5 Sediment Transport by Vortex Impingement

Over the years there have been a number of studies on the interaction of vortices interacting with a sediment bed. Although these flows are idealized from the more natural flows, they represent a more repeatable experiment for measurement and there is an analytical solution for the inviscid flow field. This allows for a better understanding of the role the coherent turbulent structures play in transporting sediment.

Sutherland (1967) was the first to qualitatively study the sediment transport under pulsating jets. He discovered that the impinging vortex rings disrupt the viscous sub-layer, resulting in an increase in the local bed shear. He hypothesized that the exposed particles are subjected to the vertical velocity component of the vortex ring and can be expected to lift off from the surface.

Munro *et al.* (2009) confirmed these results more recently, with a study of the scour caused by solitary vortex rings impinging on a mobile sediment bed. Based on the resulting crater, they determined that the strong radial component of the velocity induced by the vortex was responsible for the majority of the transport. They also observed radial scarring features within the crater, caused by the rapid growth of instabilities as the ring begins to break down and loses its initial axisymmetric shape. Bethke and Dalziel (2012) continued this work and found that the radial velocity induced by the interaction of the vortex with the surface is in good agreement with the inviscid solution obtained from a line vortex. This result suggested a free-slip condition at the bed surface and that the induced velocity is independent of viscous

effects. To provide a better understanding of this free-slip condition, they performed similar experiments for a range of particle sizes. They found that for smaller particles ($d_p = 90\ \mu m$) the bed is effectively impermeable and the slip at the bed surface is dominant, resulting in mostly bed-load transport. For larger particles ($d_p = 1100\ \mu m$) however, they found that the increased permeability of the bed results in more flow penetration, and results in primarily suspended transport and a reduced free-slip condition at the boundary. They also found that the presence of the sediment bed significantly alters the structure of the boundary layer, limiting the application of traditional approaches to extrapolate the bed shear stress from boundary layer theory.

Nepf (2012) outlines the potential difficulties with traditional approaches to estimating the bed shear stress in flows with coherent turbulent structures. She performed a numerical study of the sediment transport within a vegetated channel and found that the mixing layer at the edge of the vegetation causes large coherent turbulent structures to propagate through the vegetation increasing the bed shear stress on the surface. She presents five methodologies for calculating the bed shear stress. The first is directly calculating the time averaged velocity gradient near the wall, which as previously discussed is rarely possible or practical to resolve at the laboratory scale. The second, commonly used in statistically steady channel flows, is extrapolating the bed shear stress from the local turbulent stresses. However they found that the near-bed turbulent stress is zero or close to it, so this estimator is difficult to resolve accurately in the field. The third is a balance between the bed shear stress and the turbulent kinetic energy; however since the contribution of

bed shear due to turbulence generation within the vegetation is small to negligible there is no physical reason the turbulent kinetic energy should balance with the bed shear stress. The fourth is estimating the bed shear stress from the difference in the potential forcing and the drag of the vegetation. This method however is prone to large errors because the bed shear stress is significantly smaller than either of the other terms. The fifth, which she suggests may be the most appropriate, is assuming the flow in the near-bed region is laminar and can be inferred from outer measurable quantities. Although the assumption of laminar flow near the boundary is likely not applicable to all flows, she argued it is reasonable that the viscous effects near the wall will damp the turbulence. This simplifies the problem because the bed shear stress can be estimated at the experimental scale using outer variables.

2.6 Reynolds Triple Decomposition

The periodic nature of rotorcraft flow can be viewed using a triple decomposition of the flow field. This breaks down the instantaneous velocity into three components: 1) the time average; 2) the periodic; and 3) the stochastic components. The flow field is then the summation of the three components:

$$u = \bar{u} + \widetilde{u} + u' \tag{2.9}$$

Where u is the instantaneous velocity, $\bar{u}$ is the time-averaged mean flow; $\widetilde{u}$ is the periodic component, and u' is the stochastic turbulent fluctuation. The phase-average is then an average over an ensemble of measurements with the same phase

as the reference oscillator (the speaker forcing). The phase-average then includes the time-averaged and periodic components of the flow field:

$$< u >= \bar{u} + \widetilde{u} \tag{2.10}$$

This frame of reference proves useful for flows that are dominated by periodic coherent structures, as in brownout. This decomposition can be combined with the Navier-Stokes equation of momentum by substituting the summation for the flow velocity. This yields a phase-averaged and time-averaged form of the conservation of momentum:

Phase-averaged:

$$\begin{aligned} \frac{\delta\widetilde{u_i}}{\delta t} + \bar{u_j}\frac{\delta\bar{u_i}}{\delta x_j} + \widetilde{u_j}\frac{\delta\bar{u_i}}{\delta x_j} + \bar{u_j}\frac{\delta\widetilde{u_i}}{\delta x_j} + \frac{\delta}{\delta x_j} < u_i'u_j' > + \frac{\delta}{\delta x_j}\left(\widetilde{u_i}\widetilde{u_j}\right) = \\ -\left(\frac{\delta\bar{p}}{\delta x_i} + \frac{\delta\widetilde{p}}{\delta x_i}\right) + \frac{1}{Re}\left(\frac{\delta^2\bar{u_i}}{\delta x_j\delta x_i} + \frac{\delta^2\widetilde{u_i}}{\delta x_j\delta x_i}\right) \end{aligned} \tag{2.11}$$

Time-averaged:

$$\begin{aligned} \bar{u_j}\frac{\delta\bar{u_i}}{\delta x_j} + \frac{\delta}{\delta x_j}\overline{(u_i'u_j')} + \frac{\delta}{\delta x_j}\overline{(\widetilde{u_i}\widetilde{u_j})} = \\ -\frac{\delta\bar{p}}{\delta x_i} + \frac{1}{Re}\frac{\delta^2\bar{u_i}}{\delta x_j\delta x_i} \end{aligned} \tag{2.12}$$

The new form of the momentum equation introduces a periodic form of the Reynolds stresses:

$$\widetilde{\tau_{ij}} = \widetilde{u_i'u_j'} + \widetilde{u_i}\widetilde{u_j} \tag{2.13}$$

The triple decomposition lends itself to the understanding of the periodic and stochastic contributions of the fluid stresses responsible for sediment transport. In flows like brownout, the periodic and stochastic fluctuations of the stress tend to dominate the time-averaged stresses and must be quantified for an accurate prediction of sediment transport.

2.7 Additions from this Research

This research aims to advance the understanding of the interaction of large-scale coherent vortices with a mobile sediment bed. The data obtained will be used to develop a new approach to modeling sediment transport in flows, which the mean component of the stress may be insufficient to initiate motion. A parametric study is performed to show how the relative strength of the periodic fluctuations and the mean flow affect sediment transport modeling. The results of this work, in conjunction with complimentary two-phase measurements of the sediment suspension, will aim to quantify the effectiveness of rotorcraft brownout mitigation techniques.

The outcome of this research will include a detailed study of the single-phase flow field and the resulting transport of sediment. A series of two sets of experiments are conducted to quantify the stress induced by the vortex/wall interaction and the rate at which sediment is removed from the surface. The single-phase flow fields are measured using a series of phase-locked, high-resolution, planar PIV measurements at a range of Reynolds numbers. The effect of two scaling methodologies will be

examined to extract the relative contributions to sediment transport of the coherent structures and the mean flow. The sediment transport rate is measured by a time series of surface height measurements showing the evolution of prominent bed forms. The effect these bed forms have on the flow field will also be explored through single-phase PIV measurements on a prototype bedform, representative of the observed bedforms.

The data will be used to develop a model for predicting the sediment transport. It will be shown that the developed model does a better job predicting the sedimet transport than traditional approaches by accounting for the fluctuations in the stress associated with the coherent vortices in the flow. This will provide a basis for comparison of numerical techniques in modeling the sediment transport in unsteady spatially developing flows, such as brownout.

Chapter 3: **Experimental Setup and Measurement Techniques**

3.1 Introduction

The purpose of this study is to quantify the sediment transport of a flow analog to rotorcraft downwash. Rotorcraft flow is comprised of a steady turbulent jet bounded by vortex filaments shed from the rotor tips, seen in Figure 3.1. The vortex filaments become entrained within the mean flow until interacting violently with the sediment bed. Studying the interactions between these vortices and the sediment layer are key to understanding the sediment transport within the brownout cloud.

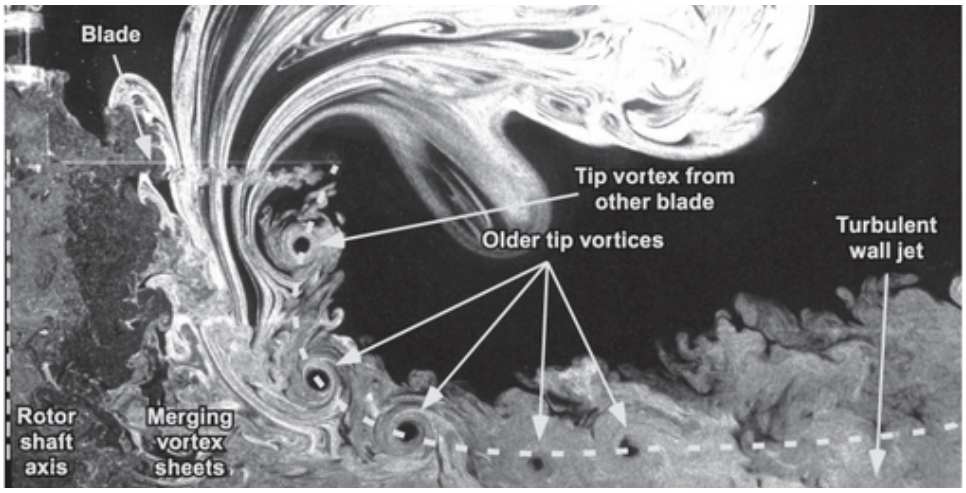

Figure 3.1: Flow visualization of a single bladed rotor Johnson *et al.* (2010)

Many sediment transport models used to understand this interaction require simultaneous measurements of the sediment transport rate and the overlying fow

field. The complex nature of rotorcraft flow and the rapid development of bedforms on the surface, which alter the stress induced on the bed, make measureing the fluid and sediment phases simulatneously impractical. For this reason, this study will focus on studying the phases indepdently and compare the results.

Even in the absence of the mobile sediment bed, rotorcraft flow is complex and three-dimensional. The helical nature of the vortex filaments, shown in Figure 3.2, induces a swirl component to the vorticity and generates instabilities even before the interaction with the ground plane. Because of this, a prototype rotorcraft flow is developed. With multiple rotor blades operating at high rotational velocities, the tip vortices can be approximated as vortex rings. Even though this flow is nominally axisymmetric, it maintains the basic physics of the rotor wake, while reducing the instabilities and providing greater control of the important parameters governing the flow.

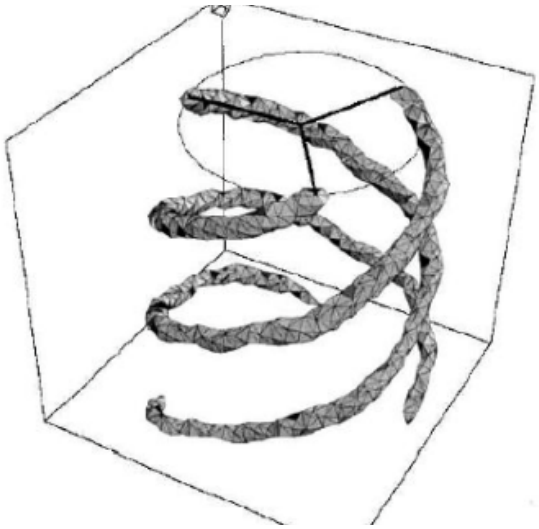

Figure 3.2: Helical vortex filaments convecting towards a ground plane Brown and Houston (2004)

There are two common methods for generating vortex rings in the laboratory

environment. The first is the classical piston method, however this method is more common for low Reynolds number flows with the medium being a liquid. The latter is the acoustic forcing of an axial jet. This technique uses an acoustic driver to produce a pressure pules, which organizes the natural shear layer at the outlet of the jet into coherent vortex rings. This method is chosen because it more closely resembles rotorcraft flow and is capable of operating at the desired Reynolds numbers.

The objective of the current work is to develop a model for the sediment transport of the prototype rotorcraft flow. To this end, three quantities need to be measured: 1) the stress induced by the flow on the surface, extracted from single-phase planar PIV measurements of the flow field; 2) the critical stress required to mobilize the sediment, obtained through a combination of single-phase PIV measurements and surface elevation measurements; and 3) the rate at which sediment is transported away from the bed, calculated from a time series of surface elevation measurements. The first two measurements can be combined to quantify the excess stress available for sediment transport. The latter is to test the developed model against observed erosion rates.

3.2 Flow Generation

The prototype rotorcraft flow is produced by an experimental rig (Figure 3.3) consisting of an inlet blower, a forcing loudspeaker, a turbulence management section, and an outlet nozzle. Each section of the rig is designed to generate an axisymmetric flow with highly-organized and repeatable vortex rings. This section will

detail each component and the respective performance testing.

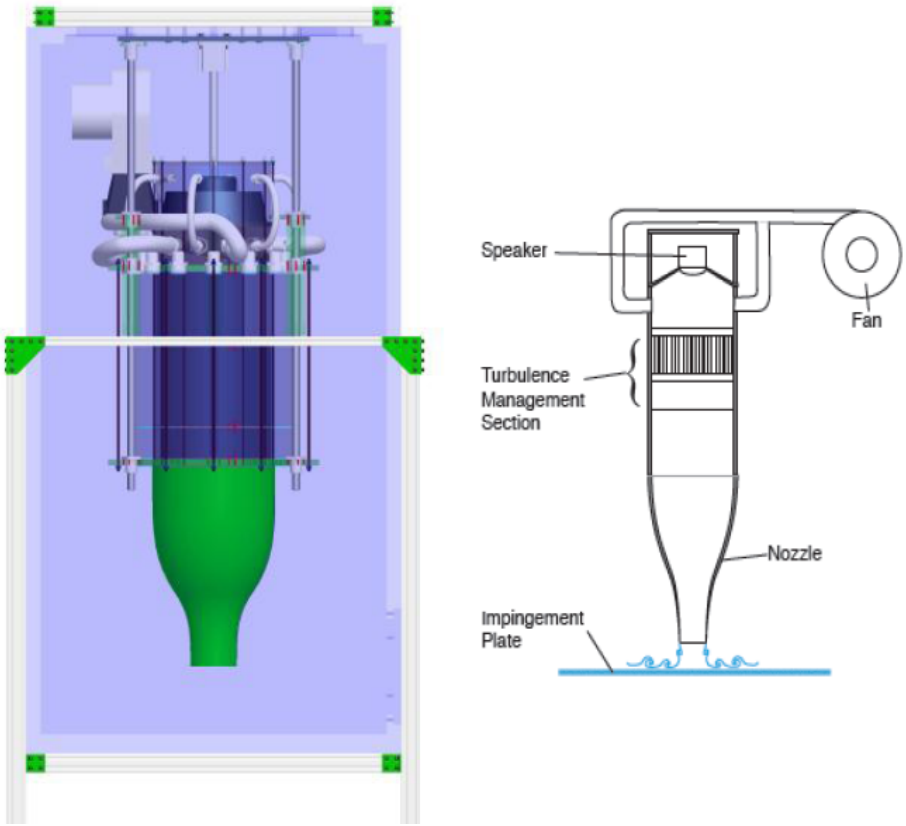

Figure 3.3: Schematic of experimental test rig

Mean Flow:

A Nautilar 12.3 variable speed, DC brushless blower, located just above the tank to avoid sediment ingestion, generates a high inlet pressure. The flow is distributed evenly by a diffuser to the plenum through three inlet tubes. The inlet tubes were equal in length and evenly spaced around the plenum to provide an axisymmetric flow to the plenum. The flow then passes through a turbulence management section, consisting of screens and a honeycomb, before exiting the outlet nozzle.

The outlet nozzle was designed based on the parameters specified by Morel (1975), with a contraction ratio of 3:1. The nozzle reduces non-uniformities in the outlet flow, the turbulence of the mean flow, and pressure losses across the screens and honeycomb. The nozzle standoff height is fixed for all experiments at $h/R = 2$ (10 cm). Single-phase PIV measurements were performed at the outlet of the nozzle to test the performance of the set up. A calibration curve was developed to relate the input voltage with the centerline velocity of the jet, shown in Figure 3.4. The root-mean-square (rms) of remaining turbulent fluctuations of the centerline velocity were found to be less than 0.8% of the mean, which is less than the uncertainty of the PIV measurements (discussed later in this section). The planar measurements of the outlet velocity show that the flow is indeed axisymmetric.

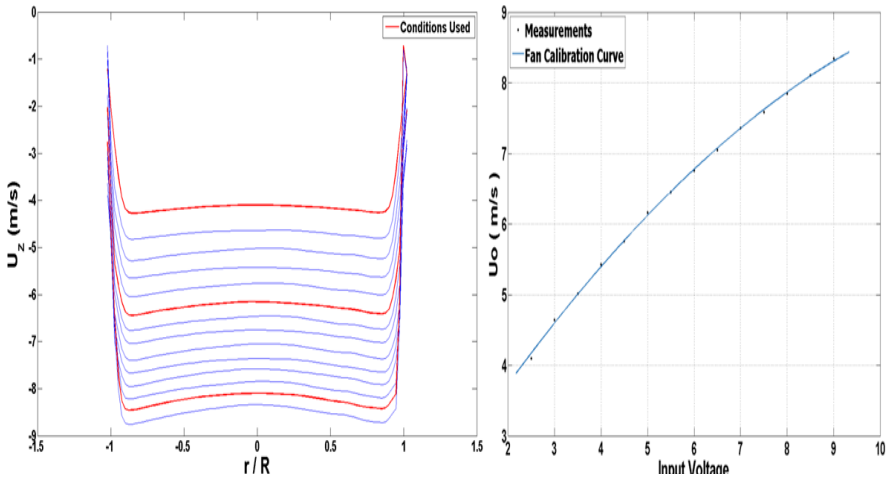

Figure 3.4: Mean nozzle outlet velocity profiles (left) and voltage calibration curve (right)

In the absence of external forcing, the nozzle outlet naturally sheds vortices formed by the Kelvin-Helmholtz instability on the boundary of the jet core flow and the surrounding environment. This resembles the desired flow; however the

vortices shed unpredictably and may pair randomly before reaching the ground plane, highlighting the need for the acoustic forcing to organize the flow.

Vortex Generation:

Vortex rings are continuously generated by a pure harmonic tone from a Ciare 12 2000 W subwoofer. The Ciare subwoofer was chosen because it showed a high-quality performance at the frequency range desired for this experiment (35-75 Hz). The frequency range was chosen to match a subharmonic of the natural shedding frequency of the unforced jet and to maintain similar Strouhal numbers. The Strouhal number is a dimensionless number that represents the periodicity of the flow and is defined as:

$$St = \frac{fR}{U_o} \tag{3.1}$$

Signal amplification is necessary for stable generation of vortex rings. An AE Techron DV.1 Experimental Amplifier was employed to amplify the forcing signal. At low speeds, forcing at high amplitudes can result in the development of a trailing vortex of opposite sign. The trailing vortex is generated as the loudspeaker return stroke creates too strong of a suction and results in a local flow reversal at the nozzle tip. In this process, the trailing vortex becomes wrapped around the primary vortex interfering with the generation of a repeatable vortex array. Because of this, it is desirable to force the jet close to a subharmonic of its natural shedding frequency to minimize the required input signal amplitude for stable vortex formation. An estimation of the natural shedding frequency is attained by calculating the distance between two naturally shed vortices propagating at about half of the mean jet flow,

shown in Figure 3.5. This estimation of the propagation velocity is based on phase locked data of the forced flow and is valid only in the region before the interaction with the wall. A discussion of the vortex tracking process is reserved for Chapter 4.

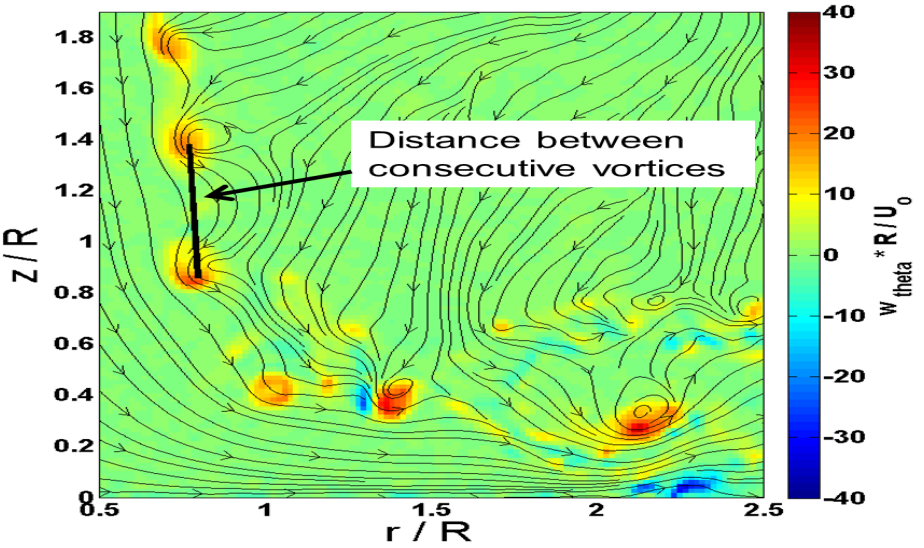

Figure 3.5: Naturally shed vortices formed by the Kelvin-Helmholtz instability at the outlet of the unforced jet

Scaling Analysis

In order to apply this research to the brownout problem, it is necessary to view quantities in relevant rotorcraft scales. Thus the data is non-dimensionalized based on known rotorcraft dimensions. Length scales are normalized by the outlet radius (R=5cm), which is analogous to the blade length. The mean downwash velocity (U_o) is used to scale velocities and fluctuations. The presence of the sediment particles introduces another length for scaling, the particle diameter (d_p). This represents a mean of the particle size class, with 50% of the particles in the class being larger than this diameter.

3.3 Data Acquisition

The current work is comprised of a series of four separate experiments. The first is a series of phase-locked PIV measurements of single-phase forced airflow on a flat plate. The second is a combination of multi-phase and single-phase flows measurements near the critical conditions for sediment transport. The third is a time sequence of the sediment bed surface evolution under the same flow conditions. The last is a series of PIV measurements on a prototype bedform. The measurement techqniue used in each experiment is discussed in this section.

3.3.1 Single-Phase Measurements

Experimental data of the airflow was obtained through planar PIV measurements. PIV relies on the imaging of seeding particles, which are chosen to have a sufficient density and size in order to faithfully follow the flow. These particles are illuminated by two consecutive laser light sheet pulses, separated by a very small amount of time such that the displacement of the tracer particles can be assumed to be linear. The tracer particles in this experiment were 1 micron droplets of Bis (2-ethylhexyl) sebacate, atomized into an aerosol following the procedure outlined by Kahler *et al.* (2002).

For this study, the light sheet is generated by a Litron nanoPIV Nd:Yag laser, which produces coherent light at a wavelength of 532 nm and can reach repetition rates of up to 15 *Hz*, with a maximum output of 1200 mJ, and a pulse duration of 4 ns. The axisymmetric Gaussian beam output from the laser is converted to

a vertical sheet using a 500 mm focal length cylindrical lens located 1.575 meters from the center of the imaging planes. For easier manipulation of the sheet, it was reflected off two mirrors before entering the tank, adding 50 mm to the working distance. Figure 3.6 shows the orientation of the light sheet with respect to the nozzle and the imaging planes for PIV measurements.

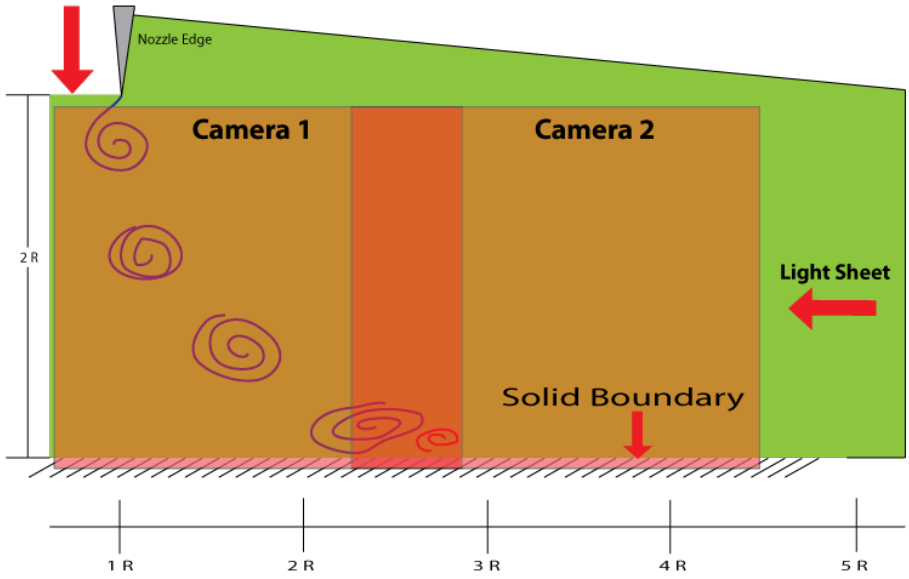

Figure 3.6: Schematic of imaging planes and light sheet orientation for PIV measurements

Images were captured using two LaVision Imager Pro X cameras with overlapping co-planar fields of view, using two 105 mm Sigma Ex lenses with the aperture set at f/5.6. Shown in Figure 2.6, the upstream camera captures the shedding and development of the vortex ring, while the downstream camera captures its rebound and rapid decay. The field of view was centered about the location where the vortex impacts the ground plane, the location of the peak stress induced by the flow. The

imaging system is synchronized with the periodic forcing signal in order to phase lock measurements to the vortex generation.

The PIV measurements of the single-phase flow was were processed using DaVis PIV software. The images are pre-processed using a sliding minimum subtraction routine. This routine subtracts the minimum intensity of each pixel in the first five images from the entire data set. This routine removes background noise and stray reflections from the ground plane from each image. Although this removes significant intensity information near the ground plane, the resulting images have a uniform background. A simple rectangular mask was applied to these images to remove reflected particles below the surface. The images are then passed on for cross-correlation. The cross-correlation was calculated using a multipass algorithm, beginning with an initial pass of a 64 x 64 pixel (1600 x 1600 μm) interrogation window with 50% overlap. The vectors from this pass then serve as an estimate for two following passes of a smaller 32 x 32 pixel windows with a 50% overlap. Between each pass, a 3 x 3 median filter is applied to remove any erroneous vectors that lead to larger errors. The 32 x 32 pixel window size was seen as a compromise between the larger scale motions of the vortex and the large velocity gradients near the surface. The vector fields were post-processed using a 3x3 median filter removing vectors greater than 2x the rms of the surrounding vectors (LaVision (2007)). The final processing routine consisted of a stitching of the vector fields from each camera using the spatial calibration of each camera. The final vector fields were passed to Matlab using the readimx tool, provided by LaVision, for the necessary calculations.

3.3.2 Threshold Conditions

A key to any sediment transport model is the critical condition for motion. This condition can be approximated based on the properties, however due to its variability and significance in predicting transport, it is valuable to measure it for the current conditions. It is extremely challenging experimentally to measure the exact conditions for which a single particle on the surface begins to move. For this reason, the critical condition is considered to be when the imposed flow results in a measureable change in the surface, following a similar procedure to Munro *et al.* (2009).

To perform these measurements, an initially planar sediment bed is exposed to the unforced jet for 300 seconds. The flow is then halted and the resulting surface is imaged. If the surface remains unchanged, the surface is screeded and the fan voltage is increased by .1 volts (.9 m/s). This increment was the smallest resolution of the DC power source. When the flow eventually produces a change in the surface the previous step is considered to be the onset condition.

Since the flow under the unforced jet is unsteady and spatially developing, it is important to understand more detail about the local flow field at these conditions. Single camera PIV measurements were performed in order to quantify the stress induced by the critical flow field. Since the larger scale flow field is less vital for these conditions, a smaller (7 cm x 7 cm) field of view was used. To achieve this field of view, a 200 mm focal length Nikon lens replaced the 105 mm lenses used for the previous PIV measurements. The resulting images were then processed similarly to

the previous PIV measurements.

3.3.3 Erosion Measurements

In order to study the erosion and development of surface structures on the sediment bed, an optical topology technique was implemented. The surface height was measured by imaging the intersection line of the sediment bed surface with an impinging laser light sheet. In order to illuminate the entire surface throughout the evolution, while minimizing glare from the surface of the bed, the light sheet was made to impinge at a glancing angle closely aligned to the horizontal plane. The sheet was directed at an angle slightly greater than the angle of repose of the sediment, which was found to be approximately 34°. Figure 3.7 shows a schematic drawing of the imaging planes and light sheet for surface profile measurements.

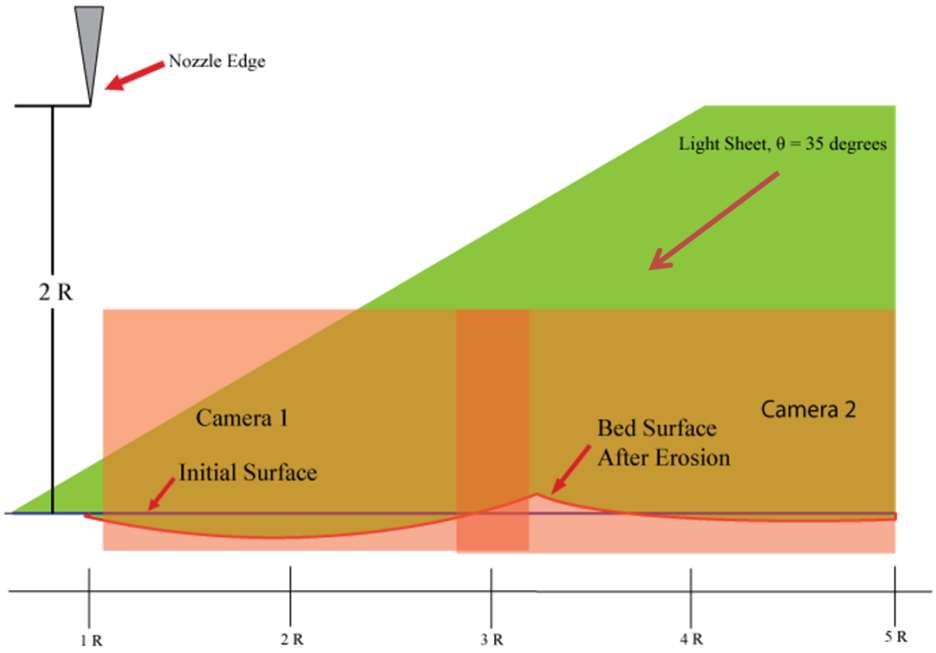

Figure 3.7: Schematic of imaging planes and light sheet orientation for surfcae elevation measurements

Because the sediment bed forms are three-dimensional, the cameras must also look down upon the surface in order to avoid obstructions produced by surface features between the camera and the region of interest. These obstructions produce discontinuities in surface profile measurements and must be eliminated. By looking down onto the region of interest, optical distortion is introduced and must be corrected for when processing the images. To account for this optical distortion, the cameras are calibrated prior to each set of measurements. This technique involves aligning a calibration target with dots of a known spacing with the light sheet, which is then imaged by the cameras. The spacing of the dots in the calibration images are then fit with third-order polynomial transformation functions by the DaVis software to map the pixel coordinates to real world dimensions, removing the optical distortions. This process is highly sensitive to the quality of the calibration images, so it is necessary to ensure the lighting conditions are uniform, the target is as parallel as possible to the camera sensor, and the images are in focus.

The 1.5 cm thick sediment bed, placed 2R below the nozzle outlet, is comprised of loosely packed glass spheres that have been sifted to remove clumps and heated to remove moisture. Moisture retained by the sediment has been found to promote clumping and irregular response to the fluid. For sediment diameters below 30 microns, clumping can also be caused by van der Waals attractive forces as well as electrostatic forces, Morrison (2013). For this reason, the smallest particle size class considered is 45-63 μm. On the other hand, for particles larger than 120 microns inertial effects dominate and the conditions to induce motion exceed the operational envelope of the flow facility.

Due to practical limitations, the sediment bed only covered a 20 degree wedge of the ground plane. In order to justify the use of a wedge to represent a semi-infinite plane of mobile sediment, surface erosion measurements were performed for both a wedge of sediment as well as a bed that covered the entire ground plane (35 cm radius). Figure 3.8 shows that the surface profile after a given period of erosion appears to be similar for both the truncated and full bed conditions, as well as axisymmetric. Therefore the term sediment bed will thus be used to refer to this wedge of sediment.

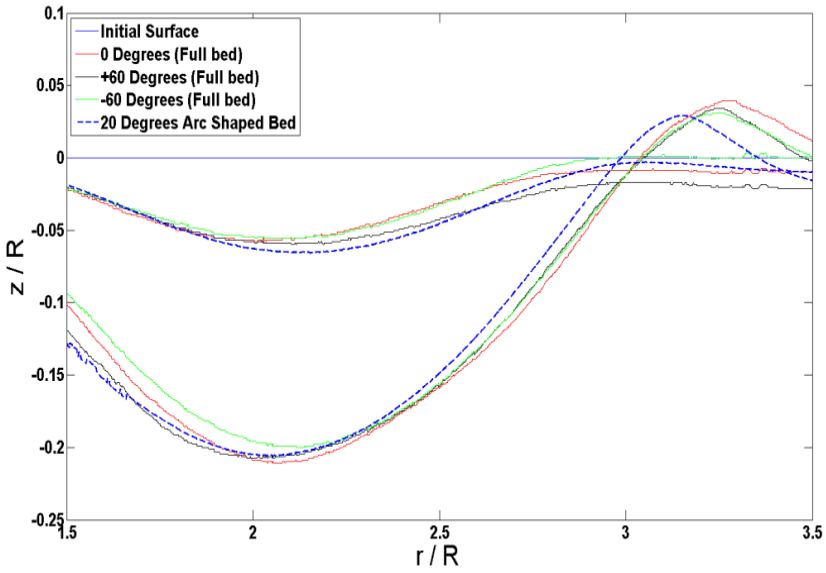

Figure 3.8: Surfaces after 15 and 60 seconds of erosion for both a full bed of sediment and a wedge

Prior to each test, the sediment bed was screeded to nominally flat and imaged before being exposed to the flow. Imaging the initial surface for each test removes any variability added by the screeding process. The sediment bed is then exposed to the flow for a period of time, scaled based on the mean flow. The flow is then halted, allowing any suspended sediment to settle out, before the surface is imaged

again. To prevent any erosion during the gradual jet decay once the blower has been shut off, a knife gate valve was added to the diffuser to suddenly, mechanically divert the flow from the surface. The process is repeated until the primary crater erodes to the lower limit of the mobile bed (just under 1.5 cm of depth).

The data collected for the surface evolution was processed by a combination of routines in DaVis and Matlab. The series of 10 images corresponding to one time step are averaged to remove any suspended sediment in a single image. The average image is then corrected for optical distortion using a dewarping algorithm based on the calibration images. This routine applies a third order polynomial transformation function to each image, stretching and rotating to produce an image with uniform magnification (linear scaling) between the camera imagepixel and real-world dimensions. This removes optical distortions due to the viewing angle of the camera.

The de-warped image is passed to Matlab using the readimx tool. In the current imaging conditions, the intersection of the planar light sheet with the sediment bed forms a curvilinear region of saturated pixels that extends across the horizontal extent of the field of view, shown in Figure 3.9.

The top and bottom boundaries of this saturated region exhibit a gradual decay with noisy gradients on either side. In order to extract an estimate of the true surface height, the image is smoothed using a Gaussian smoothing algorithm. The relevant measurement is the height of the surface, so an elliptical stencil (4 x 1 pixels) is used to smooth the vertical while leaving the horizontal resolution

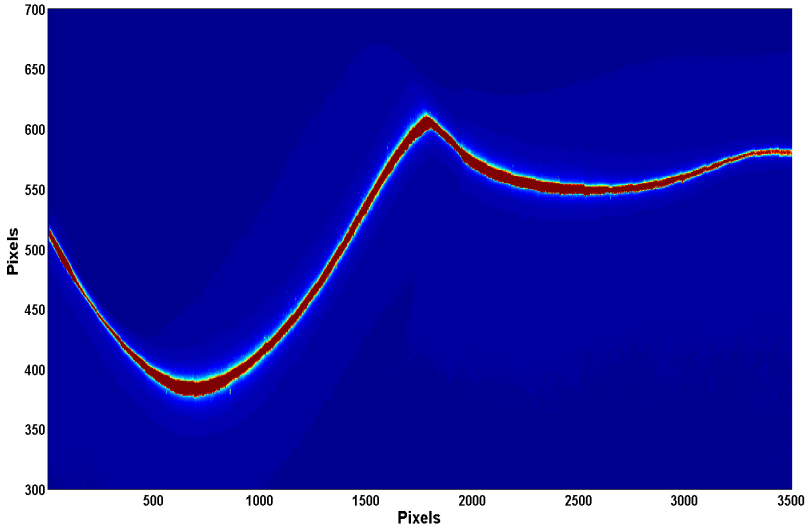

Figure 3.9: Raw image showing the illuminated surface profile

unchanged. The filter stencil is given by:

$$k = e^{\frac{-\left(x^2+\frac{y^2}{4^2}\right)}{2r}} \tag{3.2}$$

Where k is the smoothed value, x and y are the neighbouring points, and r is the smoothing radius. The smoothing removes noise around the edges of the profile and places the maximum intensity at the midpoint of the saturated region, seen in Figure 3.10. This point is then extracted as the best estimate of the surface height. Arguments can be made as to whether this midpoint is the true surface height, however the objective of measuring the relative change in surface height is unaltered by this convention.

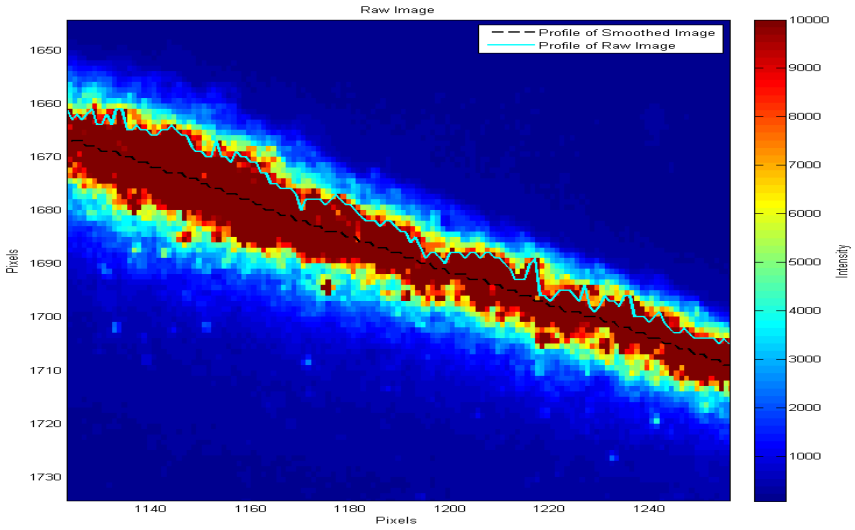

Figure 3.10: Raw image showing the improved surface elevatino measurements after smoothing

3.3.4 Single-Phase Measurements on Bedforms

The relatively constant shape of the bedforms throughout the erosion of the bed indicates there is a preferred shape of the bed boundary, which conforms to the stresses imposed by the fluid. This process leads to a more spatially unform transport of sediment. The development of this quasi-equilibrium state shows that there is a coupled effect between the stress imposed by the fluid and the shape of the bedform. Quantifying this effect experimentally is extremely difficult in the presence of the suspended particles and the constantly evolving bed. The particles refract significantly more light than the tracer particles in the PIV, resulting in errors near the bed or potential damage to the camera sensor due to over exposure. The constantly evolving bed leads to large uncertainties due to the repeatability of the crater shape and the phase-locking process. For this reason, a series of single

phase flow experiments were performed for flow conditions corresponding to case E imposed on a stationary prototype bedform to quantify the changes in the flow dynamics caused by the bedforms.

The prototype bedform was created by exposing a mobile bed to flow case E until the initial crater was 1 cm deep. The now eroded bed was then frozen by an aerosolized adhesive (hairspray), removed from the tank, and digitized by a 3D laser scanner. The laser scan of the bed surface was then 3D printed (Figure 3.11). The errors associated with the scanning and printing of the piece were found to be within the uncertainty of the surface elevation measurements, discussed in the next section.

Figure 3.11: Prototype bedform used in single-phase measurements.

The prototype bedform the was positioned on the test surface in place of the glass plate used in the single-phase measurements in section 3.3.1. This eliminates the variability associated with the crater shape. Fixing the crater shape also allows

for a more accurate phase-resolved data set as the surface does not change between data collection. The crater shape was found to be quantifiably similar to those in the erosion measurements experiments.

In order to perform PIV within the crater, the laser must be tilted as in the erosion measurements. This poses a risk to the camera and causes errors in the PIV measurements, as the surface refracts light. For this reason the bedform is painted with Rhodamine based paint. The paint is excited by the 532 nm wavelength light from the laser, and fluoresces at a wavelength between 510-710 nm. The increased wavelength light associated with refraction from the surface is then filtered out mechanically using a bandpass filter (522-542 nm 50% attenuation range). Even though every measure was taken to reduce the effects of the refracted light from the surface, there is still a significant trace of it in the images. For this reason, a mask was applied to the images to remove the area of excess refracted light. In order to prevent added three dimensional effects from the sharp step at the edge of the prototype bed, a surrounding bed of particles was maintained throughout the experiments.

A series of 18 phase angles containing 250 images each was collected, to provide a similar resolution to the results for the flat plate measurements. The total field of view was 16 cm by 8 cm, providing slightly better resolution near the wall. The data was processed using a sliding-minimum-subtraction, the passed to a multi-pass cross correlation. The window sizes used for the cross-correlation were 64 x 64 then 48 x4 8 (.63 mm x .63 mm and .47 mm x .47 mm respectively). An elliptical window, with a major-minor axis ratio of 4:1, was used in attempt to further resolve the near

wall gradient; however the remaining unattenuated light from the surface made this difficult. The data was then passed into Matlab for the necessary calculations.

3.4 Uncertainty Analysis

Common sources of error in PIV measurements are caused by the seeding density, velocity gradients within a single interrogation window, and out of plane loss of correlation due to the three dimensionality of the flow. In order to minimize effects of seeding density, the flow was reseeded every 500 image pairs to maintain a minimum of 4 particles per interrogation window. The delay time between the image pairs was calibrated to limit the maximum pixel displacement to less than of the interrogation window. The smallest interrogation window size of 32 x 32 pixels was used to minimize gradients within a single window. Although precautions are taken to minimize PIV associated errors, it is possible to make a conservative measurement of their impact on the velocity measurement. A region of no flow is expected outside the jet flow (Figure 3.12), so the time-averaged rms within this region is representative of the noise within the measurements since it is non-zero. This results in an uncertainty of 1.29% of the mean velocity, and is similar for each of the flow conditions.

Ideally each vortex will take an identical trajectory, however in reality the trajectory was found to vary greatly with each event. This phenomenon is also seen in realistic rotorcraft flows and is influenced by the mean flow (not random) so it should be considered as a general source of uncertainty. This uncertainty appears

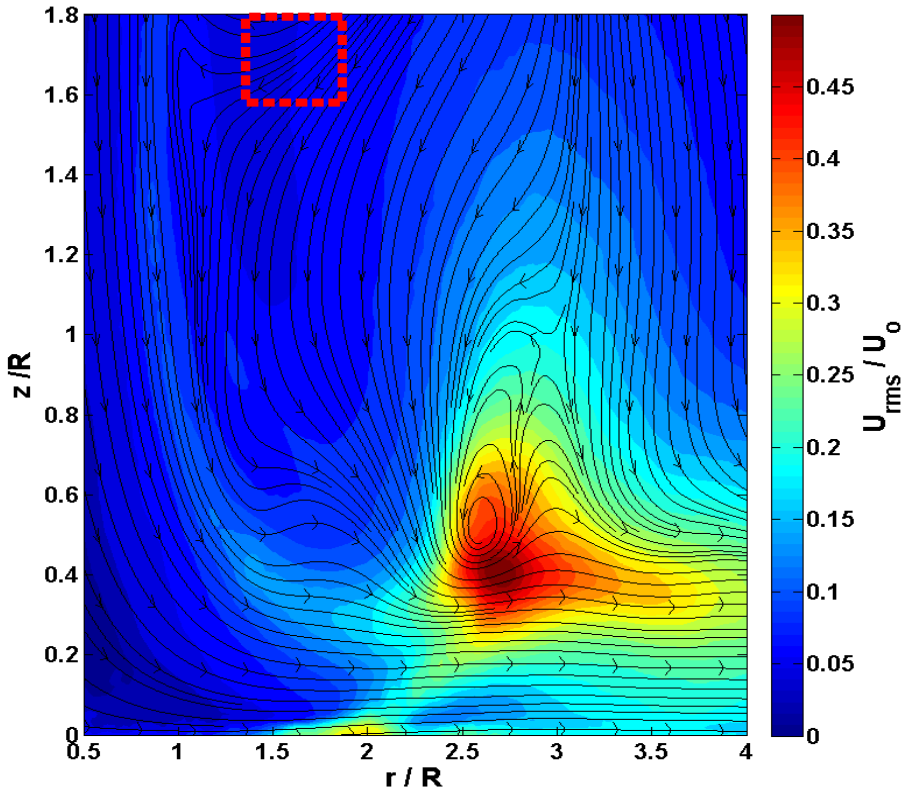

Figure 3.12: Contours of $||u_{rms}||$ showing region of no flow used for uncertainty estimation

in the form of the stochastic component in the Reynolds triple decomposition thus influencing the final result. The jitter is also influenced by the small natural vortices generated by the Kelvin-Helmholtz instability at the outlet of the jet. These two sources of uncertainty produce significant errors in the measurement of a vortex event and affect the ensemble averaging process. The maximum value of the phase-averaged rms was divided by the number of images in the ensemble to produce an estimate of the standard error in the mean velocity. This error was approximately 0.8% of the maximum reported velocity, bringing the total estimated uncertainty of 2.09% in the velocity measurements. The resulting propogated uncertainty (detailed

in Appendix A) in the vorticity measurements is 2.96% .

The largest source of error in the surface height measurements is the repeatability of the erosion. Every effort was taken to remove environmental affects such as moisture, however there is still a significant variance between successive tests. Figure 3.13 shows the mean profiles for one case and the 95% confidence interval for the true surface height defined by 10 repeated trails. The variability increases with time and varies case by case, so it has a significant affect on the final erosion rate measurement. The resulting uncertainties can reach up to 30% of the mean erosion rate for the unforced cases, however they are typically closer to 15% for the forced cases.

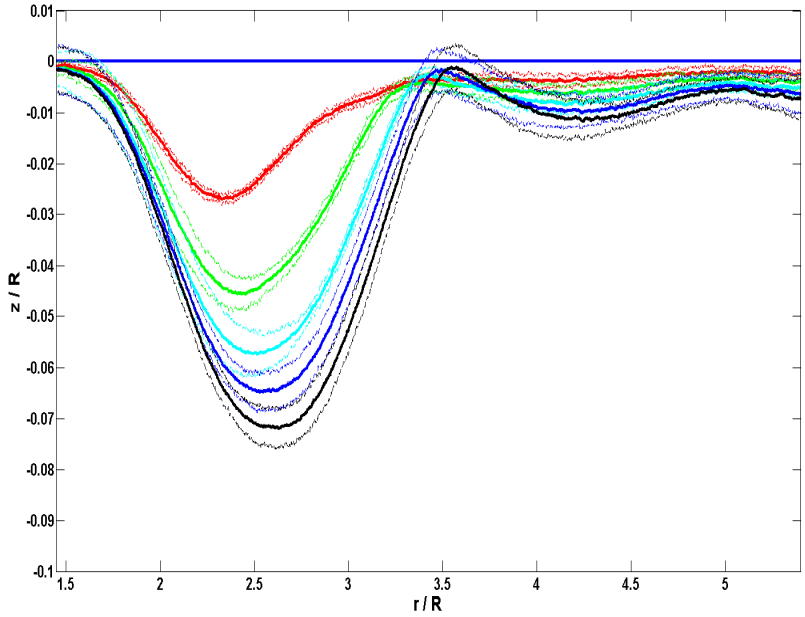

Figure 3.13: Surface profiles for case SP_D with the mean profiles (solid lines) and the 95% confidence interval (dashed lines)

Another soruce of uncertainty in the surface height measurements is the error produced by the assumption that the true surface height is the midpoint of the

saturated line. The thickness of this saturation line can be taken as an estimation of the error. In order to reduce the thickness of this line, the laser power is reduced to just 1% of the maximum power and the aperture of the camera is increased to $f/8$. Even with these steps, the error associated with this assumption is 5 pixels (250 μm) or 0.17% of the initial surface height.

Another source of error in the surface height measurements is the optical distortions associated with the viewing angle. Although the de-warping process minimizes the impact of these distortions, there is an error associated with the calibration process. The associated error in this process is, estimated by the DaVis software, as .1 pixel, bringing the total uncertainty of the surface height measurement 0.18% of the initial height. This uncertainty is not negligible, however it is an order of magnitude smaller than the uncertainty associated with the repeatability of the experiment.

3.5 Parametric Space

Although rotorcraft flow is extremely complex in nature, the two most important feature is s are the coupled effect of the mean downwash flow and the coherent tip vortex. In order to decouple these, a parametric space of 6 forced flow conditions is studied. The first three maintain a dimensionally similar vortex across all mean flow exit velocities, while. The latter scale the vortex proportionally to the mean flow exit velocity. Figure 3.14 shows how the forcing modulates the the mean jet velocity at a point close to the nozzle tip throughout the full period. Cases A-C

show a decreasing relationship between the added velocity from the vortex formation and the mean flow. Alternatively for Cases D-F the added velocity from the vortex accounts for the same percentage of the mean flow.

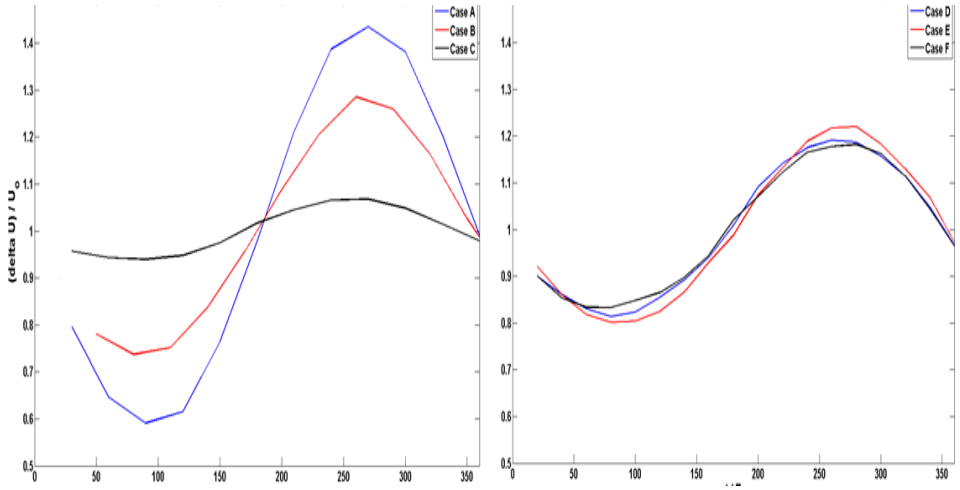

Figure 3.14: Phase-averaged velocity at a point close to the nozzle outlet throughout the forcing signal for cases A-C (left) and D-F (right) showing how the forcing is scaled within each set of conditions.

Table 3.1 summarizes the parametric space for the flow conditions considered. In addition to the forced flow measurements, 3 unforced conditions are also detailed. These conditions were chosen to give a range of Reynolds numbers and forcing conditions that are similar in their kinematics. The forcing signal waveform in all cases is the same and yielded simlar vortex development, as will be shown in the next section.

Another dimension to the parametric space is the particle size. Two monodispersed particle size classes were studied. The first is 45-63 μm, which was seen to be the lower limit before the onset of cohesive effects (Nairn (1998)). The latter being 90-120 μm, which were found to have a critical condition above the lowest

Table 3.1: Parameteric space of single-phase measurements

Case	U_{jet}	$\Delta U / U_{jet}$	Frequency (Hz)	St	Circulation (m^2/s)	Re_{Vortex}	Image Quantity	Field of View
A	4.9	0.44	35	0.357	0.3979	25900	250 image pairs for 12 phase angles	22 cm x 10 cm
B	6.24	0.29	55	0.441	0.3662	23800	250 image pairs for 12 phase angles	22 cm x 10 cm
C	7.89	0.07	75	0.475	0.3823	24900	250 image pairs for 12 phase angles	22 cm x 10 cm
D	4.63	0.19	35	0.378	0.2605	17000	500 image pairs for 18 phase angles	19 cm x 10 cm
E	6.82	0.22	50	0.367	0.4096	26600	500 image pairs for 18 phase angles	19 cm x 10 cm
F	8.43	0.18	65	0.386	0.5167	33600	500 image pairs for 18 phase angles	19 cm x 10 cm
$D_{unforced}$	4.46	0.076	89.5	1.003	0.1494	9700	500 image pairs	19 cm x 10 cm
$E_{unforced}$	6.75	0.07	145	1.074	0.2932	19000	500 image pairs	19 cm x 10 cm
$F_{unforced}$	8.34	0.063	168	1.007	0.4096	26600	500 image pairs	19 cm x 10 cm
G	6.82	0.23	50	0.367	0.4296	27900	250 image pairs for 18 phase angles	16 cm x 8 cm

flow conditions. For this reason, these particles were only tested at the two higher Reynolds number flows. It is unrealistic in real-world conditions for sediment layers to be composed of a single size class, so a third batch of mixed particle sizes was also tested. This batch was a 50/50 mixture by volume of the smaller and larger size classes.

To establish how effectively each flow condition transports sediment away from the surface, a series of complimentary experiments were performed to capture the surface evolution and the rate at which particles are removed, referred to as erosion. Table 3.2 details the conditions for these experiments.

The time between surface height measurements were scaled with the velocity and provided sufficient time for erosion to occur. The distinct erosion pattern for

Table 3.2: Parameteric space of erosion measurements

Abbreviation	Flow Case	Repeated Trials	Mean Particle Size (μm)	Time Step (s)	Vortex Passes
SP_A	A	3	54	30	1050
SP_B	B	3	54	15	825
SP_C	C	3	54	7.5	562.5
SP_D	D	10	54	30	1050
SP_E	E	10	54	15	750
SP_F	F	10	54	7.5	487.5
SP_{Du}	$D_{unforced}$	5	54	2	179
SP_{Eu}	$E_{unforced}$	5	54	2	290
SP_{Fu}	$F_{unforced}$	5	54	2	336
LP_E	E	5	105	15	750
LP_F	F	5	105	7.5	487.5
MP_E	E	5	82.5	15	750

each case will be discussed in Chapter 4, however several qualitative features of the erosion are the same for all cases. The surface begins to form ripples, with a major trough followed by a crest, which may be above the initial surface. The crest is followed by a second trough, which varied significantly from case to case. A series of plots showing the surface evolution for all the test conditions is included in Appendix B.

Chapter 4: **Results and Discussion**

4.1 Single-Phase Measurements

4.1.1 Flow Characterization

The continuous forcing of the speaker causes the free-shear layer emanating from the jet to roll up into coherent vortex rings. Figure 4.1 details the growth and eventual interaction with the wall. As seen in previous literature (Ayedimer *et al.* (2010)) the acoustic generation of vortex rings at frequencies far from their natural shedding frequencies can lead to the development of a coherent vortex tail trailing the primary vortex ring. The presence of this trailing vorticity can lead to random variations in the vortex interaction with the wall, so the forcing conditions are chosen to ensure this trail loses coherence prior to the vortex impacting the ground. This was done by forcing the jet as close as possible to a subharmonic of the natural frequency of the shear layer. The natural shedding frequencies were calculated from the unforced jet measurements, discussed in Chapter 3.

As the vortex ring reaches the ground, it accelerates the flow beneath it, causing an adverse pressure gradient and resulting in the eventual separation of the boundary layer. The separated boundary layer subsequently rolls up into a vortex of opposite sign, referred to as the secondary vortex. The secondary vortex produces an induced velocity that directs the primary vortex away from the wall. During this rebound, the weaker secondary ring becomes wrapped around the dominant pri-

mary core. The wrapping of secondary vortex causes a rapid dissipation of both the primary and secondary vortices.

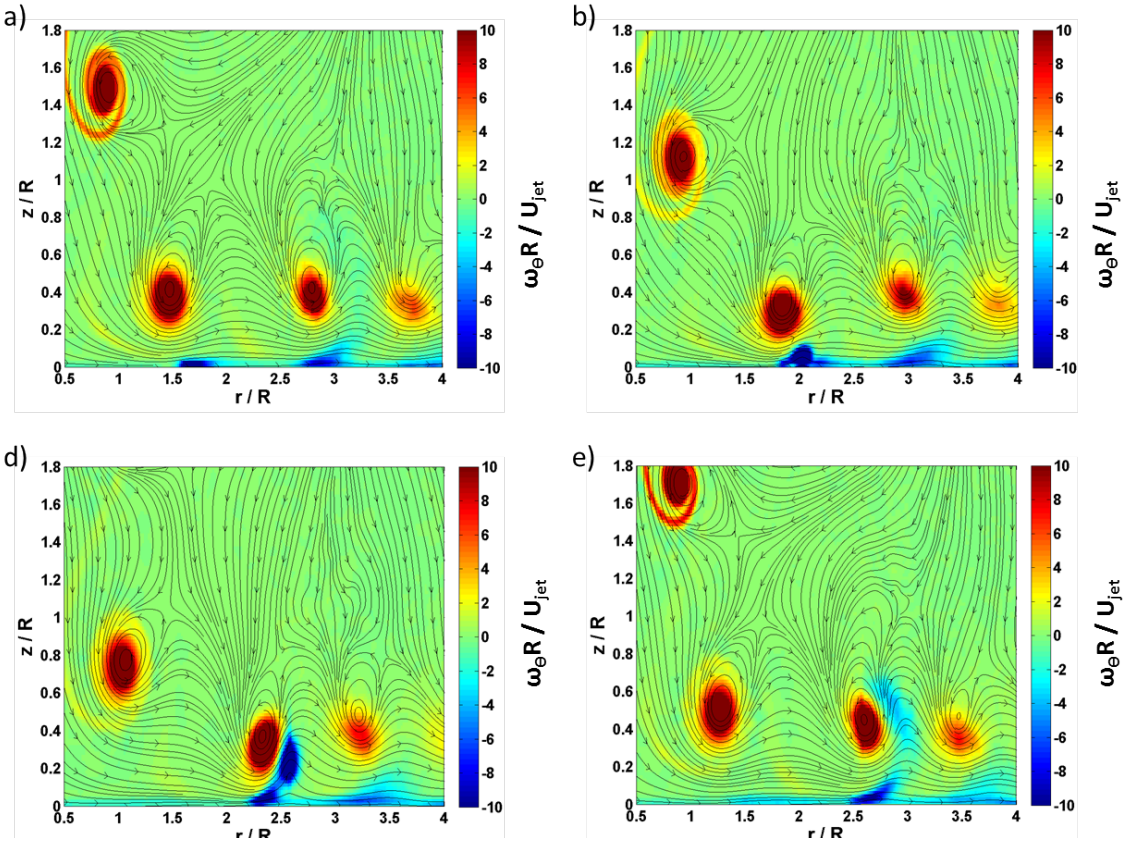

Figure 4.1: Contours of phase-averaged vorticity at $\frac{t}{T} = 0.06$ (a), 0.33 (b), 0.61 (c), 0.89 (d) overlapped by the corresponding phase-averaged streamlines

A vortex identification procedure was implemented for the calculation of circulation and vortex location. It is insufficient to calculate these quantities on phase-averaged images because the jitter in the vortex location from frame to frame becomes smoothed out by the averaging process. Because of this, the algorithm is applied to the instantaneous image of vorticity (Figure 4.2 a). The instantaneous image is converted to binary image (Figure 4.2 b) based on a threshold value. For consistency across each phase angle within a data set, the threshold value was taken as ten times the time-averaged background noise level of the vorticity measurement.

This background noise level was calculated as the rms of the time-aervaged vorticity in the same region used for the uncertainty analysis, shown in Figure 3.12 (the no flow region outside the jet flow and far away from the wall). The continuous ares of vorticity above (positive vorticity) or below (negative vorticity) the threshold are then ranked based on their respective size (Figure 4.2 c). Only the largest four areas, above a pixel size threshold that scales with radial position, for each sign are retained for calculation, and the rest of the image is zero padded. The ranked binary image is then multiplied by the original image of vorticity (Figure 4.2 d) to calculate the circulation and vorticity-weighted centroid.

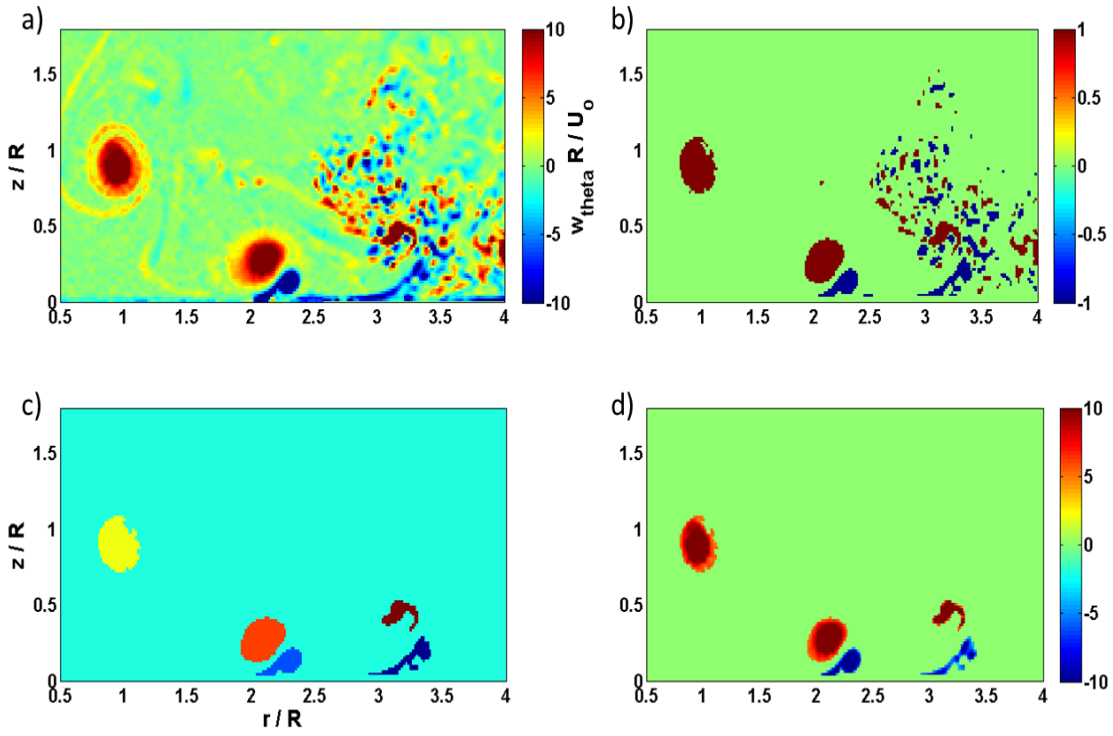

Figure 4.2: Contours showing the vortex tracking algorithim, with (a) being the original image of instantaneous vorticity, (b) being the binary thresholded image, (c) being the ranked image with only the three largest areas above size threshold, and (d) beign the product of the ranked binary image and the original image of vorticity used for calculations.

The difference in the resulting circulation for the instantaneous versus the phase-averaged values can be seen in Figure 4.3 a. The phase-averaged value consistently under predicts the circulation, specifically downstream when rapid three-dimensionalization and dissipation increase the jitter.

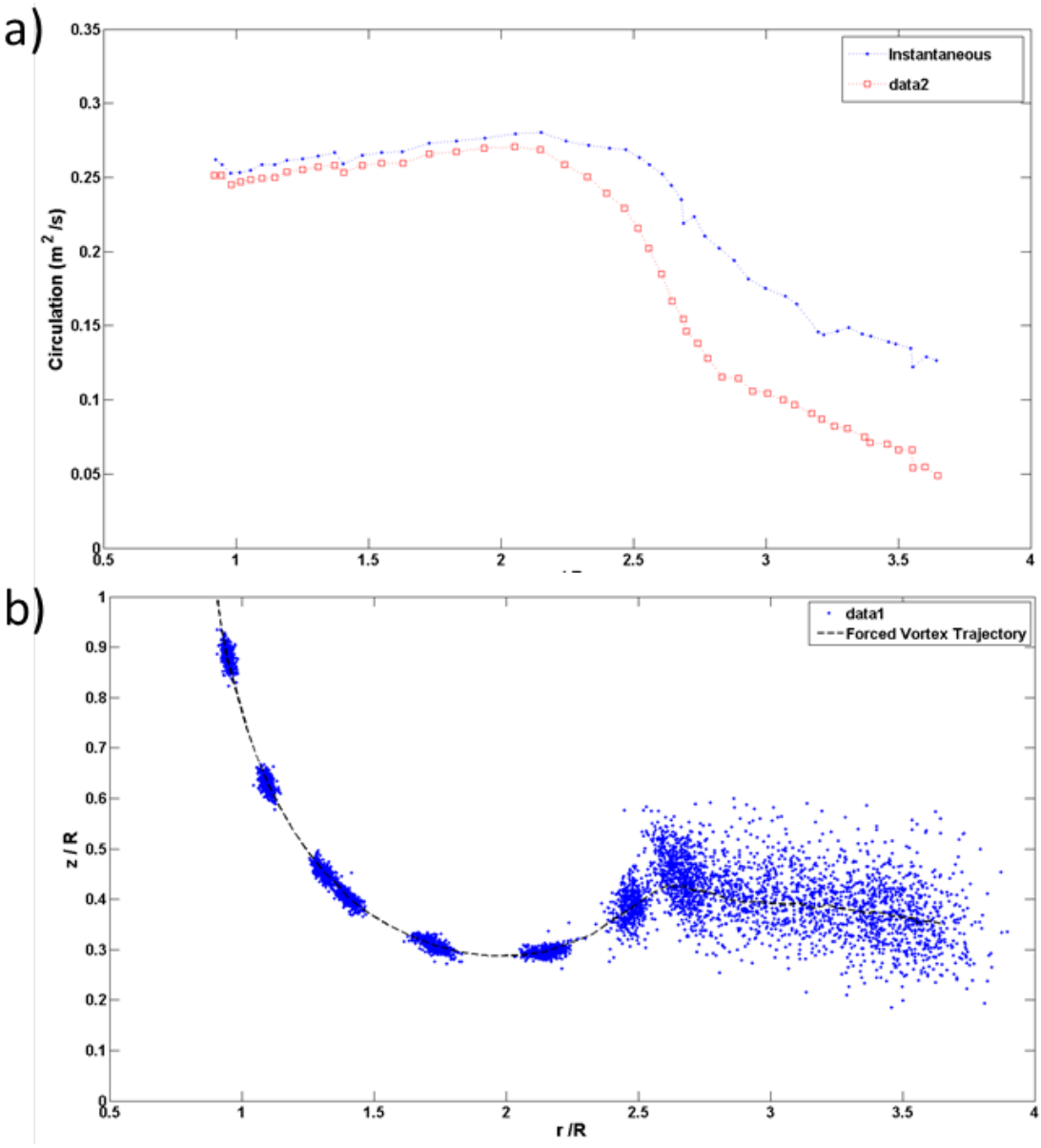

Figure 4.3: a) Resulting circulation from a phase-averaged image (red) versus calculated instantaneously then averaged over the ensemble (blue). b) Scatter plot of the instantaneous vorticity-weighted centroids of the primary vortex, with the phase-averaged trajectory (dashed black line)

The evolution of the jitter can be seen in Figure 4.3 b, which is generated by plotting the instantaneous vorticity-weighted centroid for each realization at several phase angles. This jitter has significant implications for the sediment transport because the local flow acceleration under the vortex core causes a spike in the wall stress, to be detailed later in this section.

The trajectories for cases D-F (Figure 4.4 b) are self-similar, as one would expect for conditions that are forced in a non-dimensionally similar manner. The trajectories showing a strong rebound with the secondary vortex being lifted from the wall. This self-similarity is due to the induced velocity from each vortex being similar (i.e. similar spacing and relative strengths), resulting in kinematically similar motions. The trajectories for cases A-C (Figure 4.4 a) are largely different from each other however, showing a significantly reducing rebound with increasing mean flow velocity. Comparing case C and F, the vortex in case C has a significantly weaker circulation, and thus a weaker induced velocity on the surface, so it does not separate as much of the boundary layer causing a weaker coupling between the primary and secondary rings. As a result the primary rings trajectory in case C is not altered significantly by the secondary and the separation does not occur until much further downstream.

Once the primary vortex rebounds from the wall, the secondary vortex begins to breakdown and induces a strong three-dimensional instability on the primary vortex, leading to a decay in the observed circulation (Figure 4.4 c and d). In line with the self-similar nature of the vortex trajectory, the rate of decay in cases D-F are also self-similar . In cases A-C, as the Reynolds number increases the primary

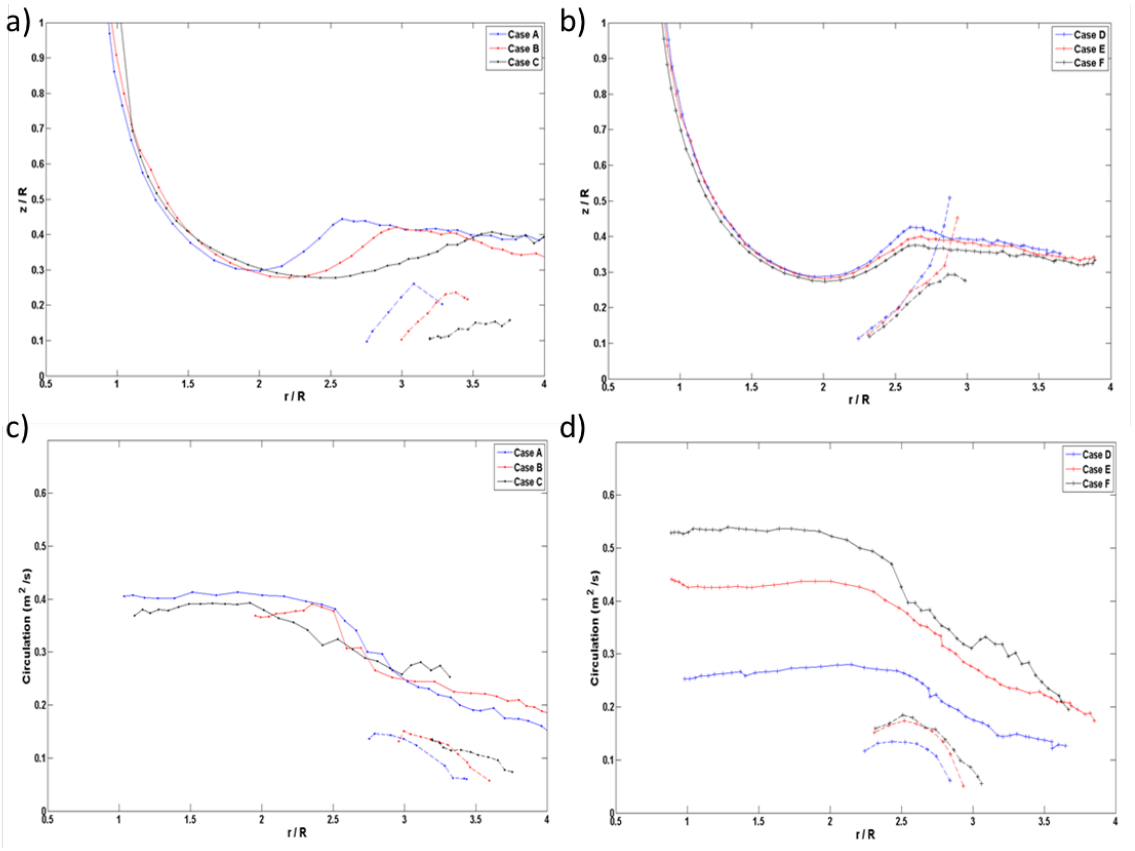

Figure 4.4: The vortex trajectories for cases A-C (a) and D-F (b) as well as the circulation development (A-C (c) and D-F (d))

vortex begins to decay further upstream, however at a similar rate.

4.1.2 Tractive Stress on Boundary

Sediment transport models traditionally relate the time averaged tractive stress on the boundary, above a given threshold, to the transport rate of sediment. For fully developed channel flows, this stress is extrapolated from the predictable variation in the Reynolds stress as it decays towards the wall, but still outside of the inner wall layers. This process relies on a fully developed boundary layer and a constant pressure gradient, neither of which are the case in this flow. For this reason

an attempt is made to quantify the wall stress directly from the PIV measurements.

The time averaged flow for each condition is similar, resembling an axisymmetric stagnation point flow decelerating as it expands outward radially. Figure 4.5 shows that there is still a slight trace of the forcing around r/R=2.5 as the rebounding vortex thickens the jet flow.

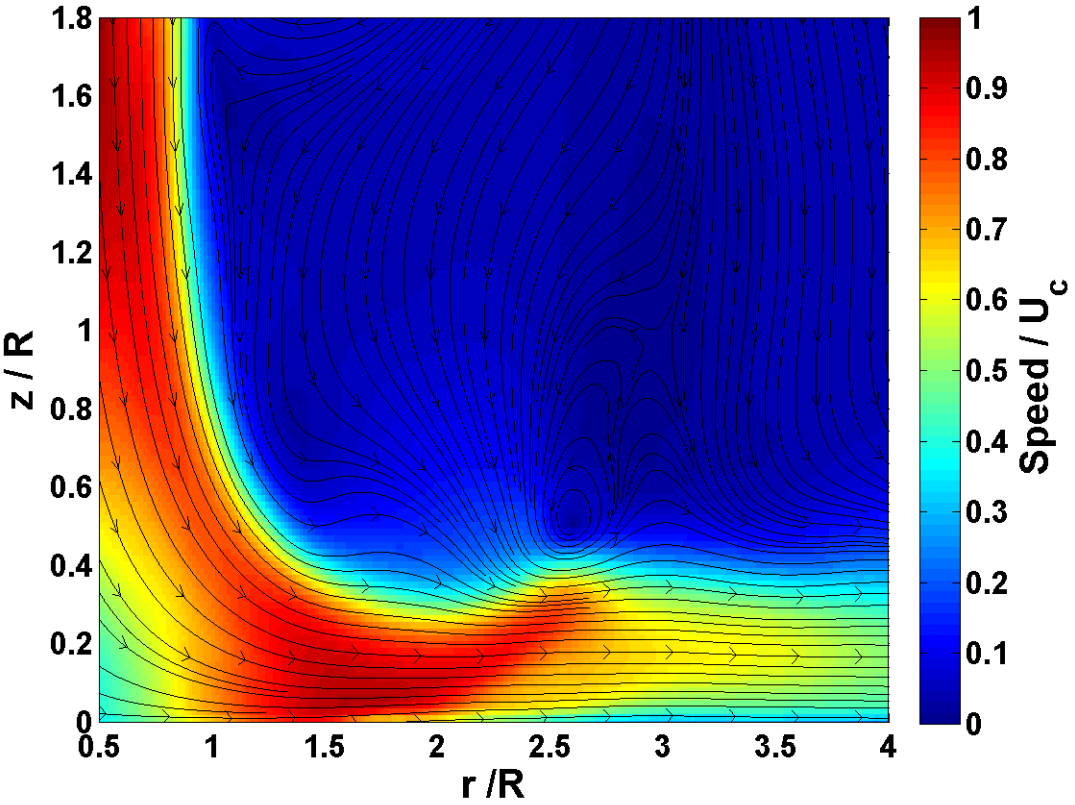

Figure 4.5: Contour of velocity magnitude for flow case D

Figure 4.6 shows time-averaged radial velocity profiles for all the forced flow conditions at several radial locations (the velocity profiles are shifted by the radial position for clarity). The profiles are similar outside the vortex impact region for all cases. Cases A-C show similar near wall gradients; however the flow away from the wall shows a significantly different development. For cases D-F, which maintain

a constant relationship between the vortex and the mean flow, the velocity profiles remain similar throughout the entire domain.

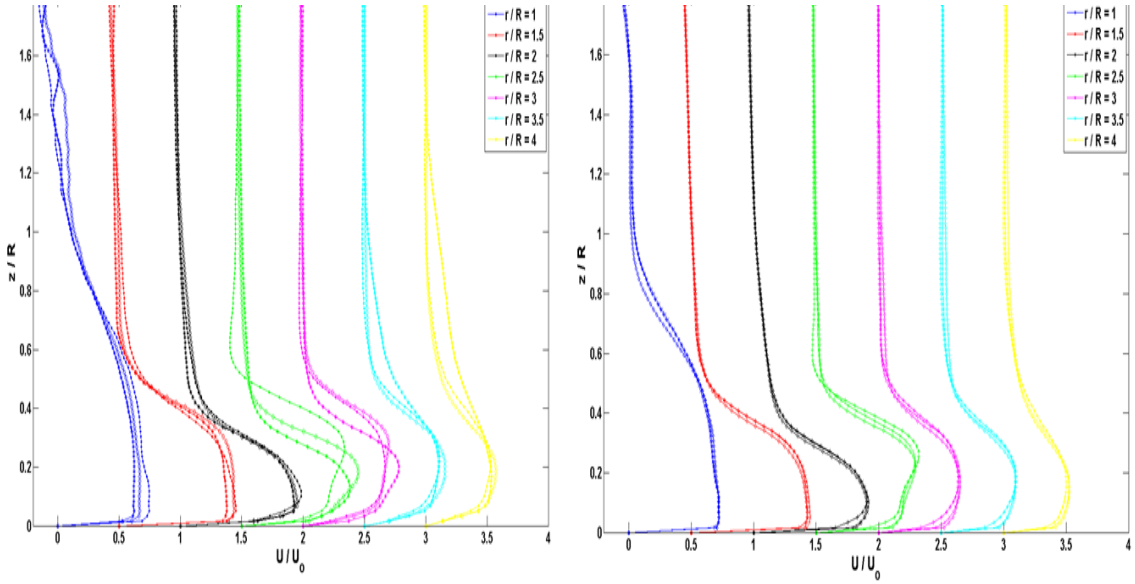

Figure 4.6: Time-averaged velocity profiles for flow cases A-C (left) and D-F (right)

As expected, the increase in the Reynolds number of cases D-F shows an increase in the near wall gradient. Accurately calculating this gradient is vital to predicting the sediment transport, because it is the mechanism by which the fluid passes momentum to the particles. This transfer of momentum occurs within the boundary layer formed on the surface. The boundary layer thickness can be estimated by measuring the height at which the velocity reaches 99% of its freestream magnitude. Applying this process to the time-averaged flow for flow case D yields a boundary layer thickness about 300 μm in the accelerating region up to about r/R = 2, then the boundary layer thickens to about a 1.45 mm by the downstream edge of the field of view. This thickness varies from case to case, with case F having the thinnest at about 1.28 mm at the downstream edge. The thickness of the boundary

layer is inversely related to the Reynolds number, so it follows that the highest speed flow case would have the thinnest boundary layer. This presents a problem for accurately calculating the wall shear stress from the experimental data, which has a liminting resolution of 800 μm.

Several possible means to extract the wall stress from the PIV measurements potentially exist: 1) use the near wall velocity gradient to calculate the viscous stress directly if all scales of motions are fully resolved, 2) use the outer flow conditions as input to an unsteady Reynolds-Average Navier Stokes (RANS) boundary layer simulation to calculate the wall stress, 3) correlate the outer flow variables (velocity, Reynolds stress, etc.) to the applied wall stress through an empirical model of the turbulence. The first of these options would be the most desirable, however this is rarely achieved in practice due to the excess spatial resolution requirements that are necessary. The second option is being explored, however for the purposes of the current work the third option is used.

An LES simulation of a similar flow by Wu and Piomelli (2015), with a Reynolds number of 33000 (based on $U_o R$), is used to develop a relationship between the outer flow variables and the wall shear stress. The simulating vortex rings were generated through a sinusoidal forcing function at the outlet of the jet, with the amplitude being 60% of the mean centerline velocity (St=0.75). The simulated domain was three-dimensional with a no-slip condition on the ground plane and periodic boundary conditions on the radial planes bounding the 45^o arc. However for the purposes of comparison to the planar measurements of this study only the azimuthally-averaged quantities are considered. The time-averaged velocity pro-

files (Figure 4.7) are qualitatively similar between the simulation and flow case C ($Re = 21500$), based on U_o and R. However, while the Reynolds number of the simulations are similar, they differ by a factor of approximately 1.5, and some differences in the boundary layer thickness can be expected as a result, in addition to any spatial resolution errors from the velocity measurement.

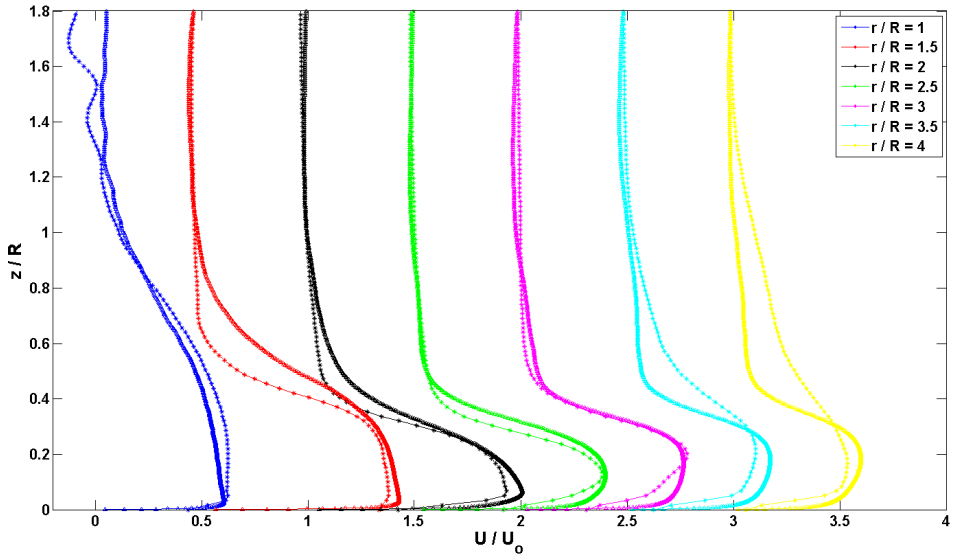

Figure 4.7: Comparison of the time-averaged velocity profiles for flow case C and the LES simulation by Wu and Piomelli (2015)

Figure 4.8 compares the time-averaged velocity profiles near the wall from the LES and the current experiment, showing that using the closest sampled velocity point in the experiment causes a biased under prediction of the wall velocity gradient and hence the wall stress. To estimate the relationship between the measurable stress (experimentally) and the wall stress, an effective stress is calculated within the LES data set at the experimental resolution. This relationship is likely to vary with the boundary layer. The boundary layer is confirmed to be turbulent through an eddy viscosity calculation within the LES simulation, with the turbulent fluctuations

becoming significant compared to the viscous stress around 100 μm (well within the boundary layer). This means the shape of the velocity profiles is dependent on Reynolds number, which varies temporally and spatially.

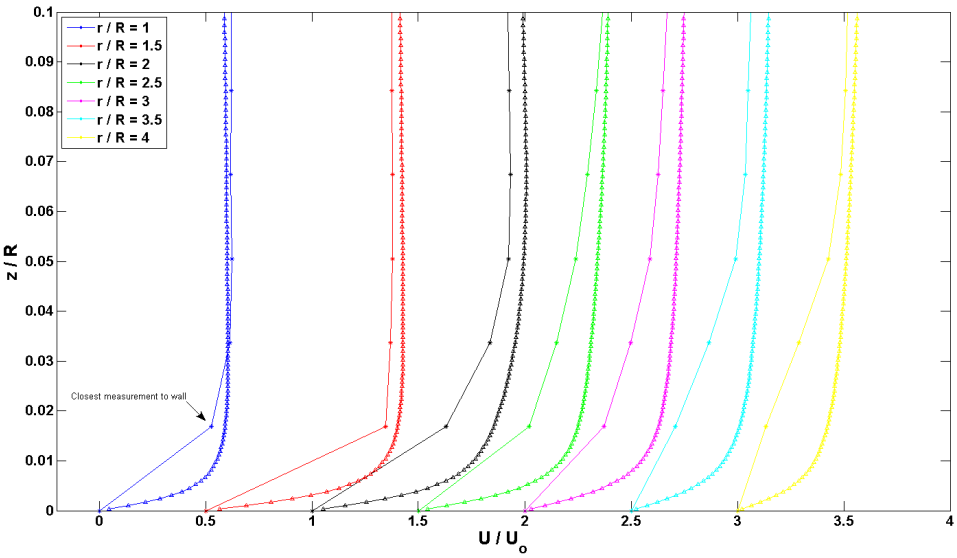

Figure 4.8: Comparison of the time-averaged velocity profiles for flow case C and the LES simulation by Wu and Piomelli (2015)

The magnitude of the effective stress is about a factor of 3.5 less than the true wall stress, both calculated from the LES data so that Reynolds number affects can be neglected. This factor is an average over the radial domain, as such it results in about a 12% under prediction of the stress in the accelerating region of the flow and about a 30% over prediction of the downstream stress. This provides a very rough estimate for the relationship between the stress that can be resolved by the PIV measurements and the true wall stress.

Applying this correction factor to the experimental results is only valid if the Reynolds number effects on the velocity profile are well known. In this case, the boundary layer is not well defined because the flow near the wall is unsteady, spa-

tially developing, and turbulent. However, this serves only as an estimate for the biased error associated with the experimental resolution. Figure 4.9 shows that the effective stress from the LES matches reasonably well with the experimentally measured stresses. This should be viewed skeptically because the relationship between the outer parameters and the wall stress is likely not as simple, and will vary with Reynolds number. These variations cannot be quantified with such a small parametric space of coarse experimental resolution and with a simulation at one Reynolds number, so more work is needed to improve the accurate prediction of near wall quantities from outer measurements. From this point on, the stresses reported are measured values multiplied by the scaling factor of 3.5.

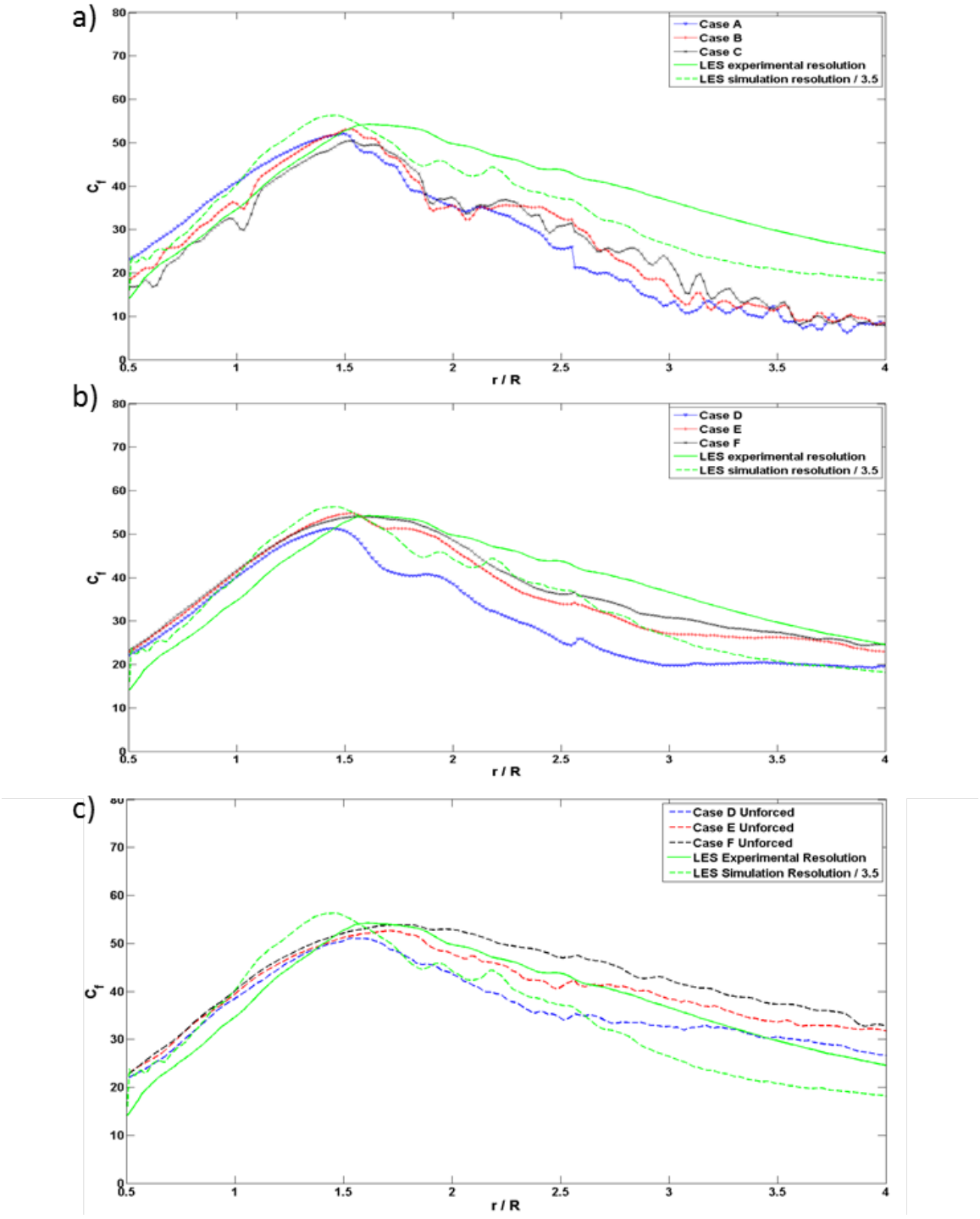

Figure 4.9: Comparison of the time-averaged wall shear stress for cases A-C (a), D-F (b), and D-F unforced with the effective and true wall stresses from the LES simulation by Wu and Piomelli (2015)

The time-averaged forced and unforced flows show similar wall stress profiles (Figure 4.10 a), however the stress in the forced flow drops off much more rapidly than in the unforced case. In the forced flow cases, the vortices impact over a small region ($1.6 < r/R < 2.2$). The vortices in the unforced flow impact over a relatively wider region ($1.6 < r/R < 3$), resulting in a more evenly distributed time-averaged stress. The trajectory of these naturally shed vortices is unpredictable because they pair randomly diverging from the path followed by the forced vortices, which have a much more regular spacing,Figure 4.10 b. shows the increased scattering of the vortices in the unforced flow. These results imply that the unforced flow produces a greater stress on the surface downstream than the forced and thus would more readily transport sediment.

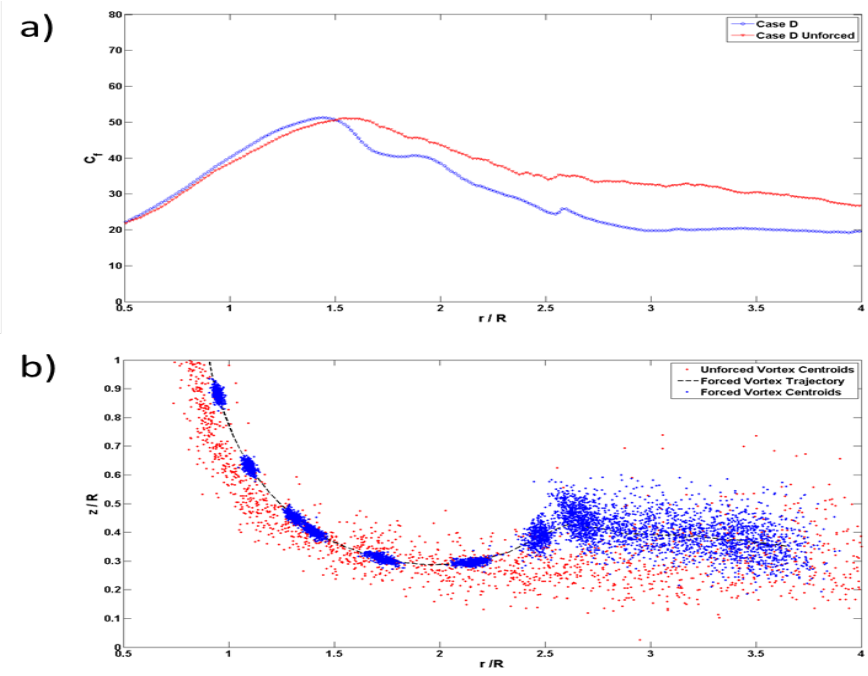

Figure 4.10: Comparison of the forced (blue) and unforced (red) time-averaged wall stress (a) and the instantaneous vortex locations (b)

The circulation of the random vortices shed from the unforced jet was calculated in a similar manner to the forced. The circulation for the vortices in the unforced jet shows significantly greater variation than the forced flow (Figure 4.11). The measured values of the unforced circulation are consistently lower than the forced vortices, confirming that they do indeed shed more frequently than the forced flow. However this is could be due to the unforced vortices being more diffuse, resulting in a larger area with a lower peak value being thresholded out in the vortex trackign algorithim. The unforced vortices do not show a significant decay downstream of $r/R = 2.5$, whereas the forced vortices begin to decay rapidly. The decay in circulation of the primary vortices is caused by the vortices interacting with the ground, which for the unforced vortices may not occur until further downstream due to the scatter in their trajectories.

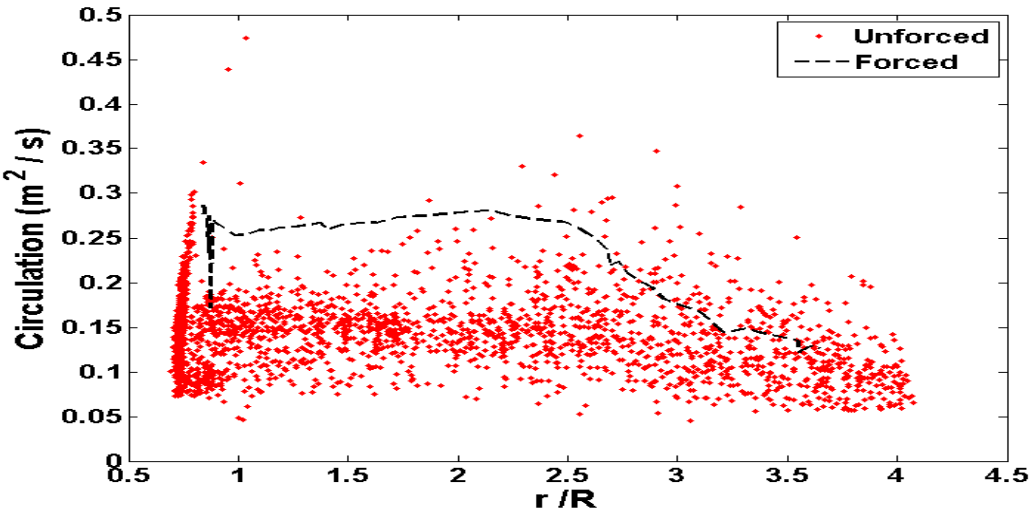

Figure 4.11: Instantaneous circulation of the unforced jet compared to the phase-averaed forced circulation, showing the reduced loss of coherence of the primary vortices in the unforced flow for flow case D

Decomposing the flow into its time and phase-averaged components allows for a better understanding of the role the vortex plays in the sediment transport. Figure 4.12 shows four phase angles of case D and the corresponding wall stress throughout the interaction. The phase-averaged wall stress increases dramatically while the vortex interacts with the ground plane. Once the vortex is ejected from the surface the stress reduces close to the time-average value. Just downstream of the impact, the stress is reduced significantly below the time-average as the counter rotating vortex decelerates the local flow. The high-speed jet formed between the primary and secondary vortices is just downstream of the peak wall stress. The tractive stress serves to mobilize the particles along the bed surface, but this jet may be responsible for the suspension of the particles once they are in motion. Although the flow contains significant stochastic fluctuations as the vortex begins to break down, these fluctuations are far from the wall and cause a significantly lower stress.

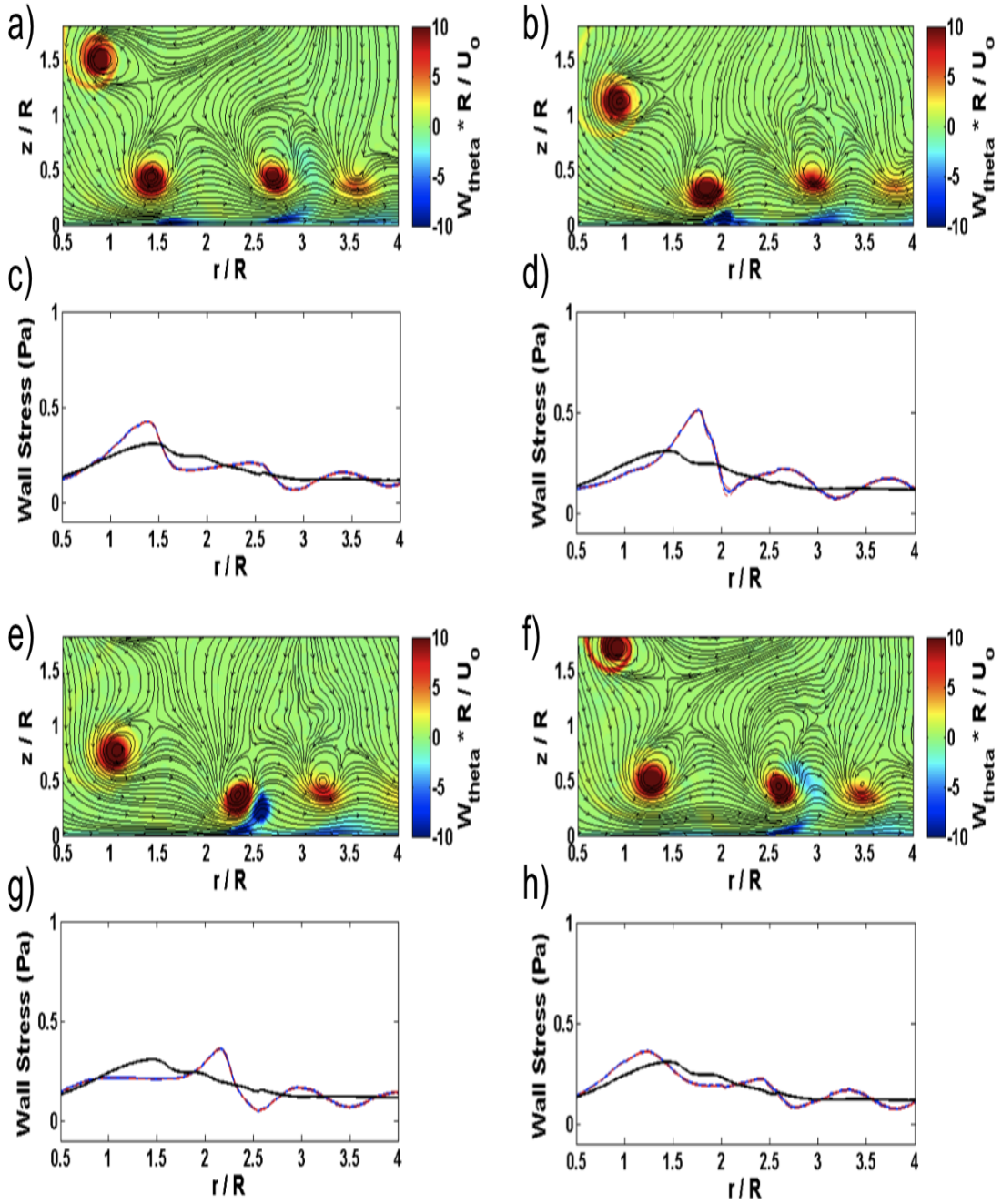

Figure 4.12: Contours of the phase-averaged vorticity (a,b,e,f) and the corresponding time-averaged (black solid lines) and phase-averaged (blue solid lines) components of the wall stress (c,d,g,h). The dashed red lines show the standard deviation within each phase.

These qualitative features of the flow field are similar for all six forced flow conditions. Trends emerge with each set of cases. In cases A-C the periodic component of the stress remains similar in magnitude for all cases, while the time-averaged component increases. This follows with the scaling, as each of these cases contains dimensionally similar vortices, but an increasing mean flow component. It is interesting to note the development of a second peak in the periodic stress component of flow case C around $r/R = 2.5$, which is not seen in the previous cases. The vortex trajectory for this case showed that the primary vortex remains close to the wall; in the other cases it showed a more significant rebound. For Cases D-F, the vortex scaling is evident as both the mean flow and periodic component of the stress increase self-similarly.

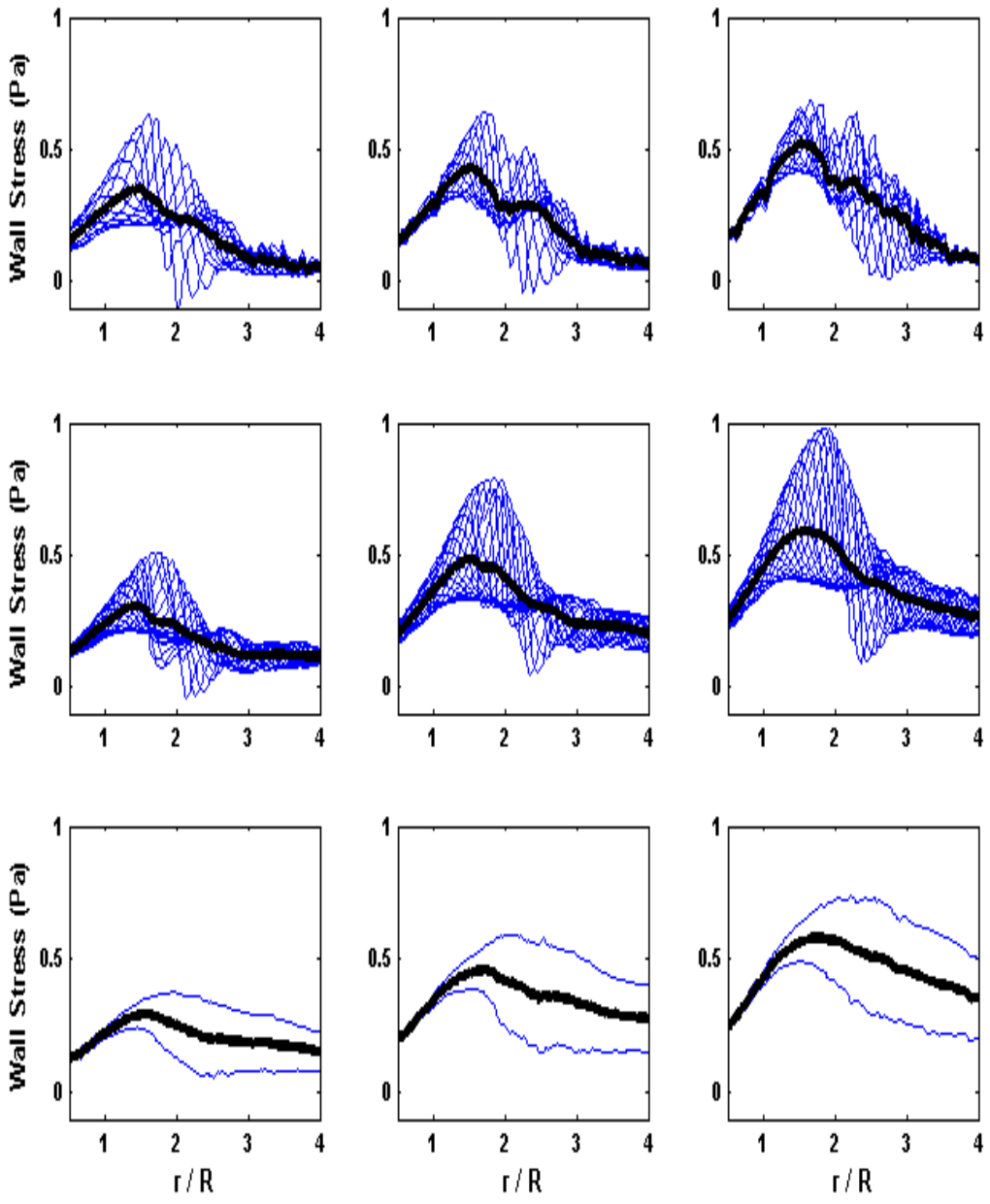

Figure 4.13: Plots of the time-average (black solid lines) and phase-averaged (blue solid lines) components of the effective wall stress (Labeled according to case, with g,h,i being the unforced flows). For the unforced flow, the phase-averaged stress is replaced with one standard deviation from the mean

4.2 Critical Conditions for Motion

Sediment transport cannot be predicted by the wall shear stress alone, it also requires a critical threshold for particle motion. The threshold stress is the maximum force a particle can resist before following the flow, so stresses below this threshold do not result in mobilization.The critical condition is very difficult to predict empirically as it varies greatly with particle properties and their orientation within the bed. For this reason, a series of PIV measurements of the flow are used to determine the wall stress sunder the critical flow. The critical flow was determined based on quantitative and qualitative observations of the sediment bed.

With the introduction of particles, the stresses can be non-dimensionalized by use of the Shields parameter:

$$\theta = \frac{\tau}{(\rho_p - \rho_f) g d_p} \tag{4.1}$$

Here τ is the wall stress, ρ_f is the fluid dentisty, ρ_p, and d_p being the particle diameter and density respectively. Alternatively the shields parameter can be expressed in terms of the friction velocity, however with the combination of the simulation and PIV calculation of the wall shear stress this form is more useful.

One method for interperting the threshold stress is taking the maximum of the time-average Shields parameter; however this neglects the highly unsteady nature of the flow. Qualitatively the mobilization of sediment is not constant, but is linked to the vortex/wall interactions. The averaging process removes the peaks in the stress

caused by vortex/wall interaction, leading to an under prediction of the maximum local stress the bed experiences for any instantaneous realization. For this reason, it is more reasonable to look at the maximum local stress of each instantaneous measurement.

Shown in Figure 4.14, the maximum of each realization (regardless of position) is overlapped with the time average. By taking the average of the maxima a new threshold value is obtained, which is 20% greater than the maximum of the time-averaged stress. Taking this value as the threshold follows the qualitative observations of the sediment transport more closely because some of the realizations now contain stresses below the mean.

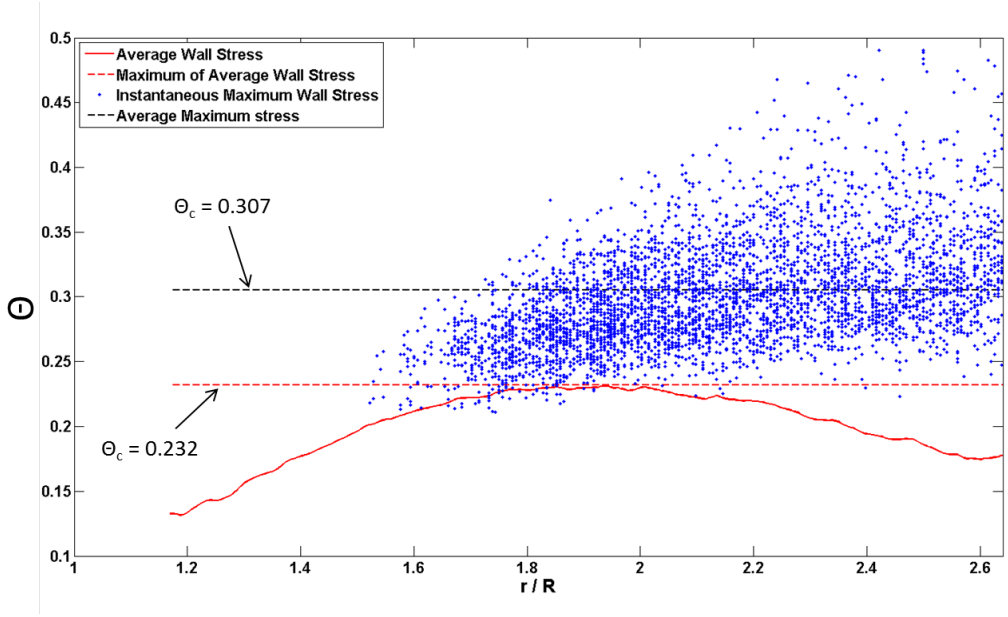

Figure 4.14: Comparison of the methodologies for calculating the critical stress for the 54 μm particles. The time-averaged (solid red line) has a maximum well below the instantaneous maxima (blue dots).

As the particle size increases the stress required to mobilize it also increases, however θ_c actually decreases. This suggests that although the larger particles re-

quire more force to move them, the effect of their increased mass is greater. Table 4.1 details the three particle classes.

Table 4.1: Threshold conditions for particles considered

D_p (μm)	v_s (m/s)	u_* (m/s)	Re_p	Θ_c
54	0.154	0.51	3.29	0.305
82.5	0.813	0.6	11.5	0.201
105	0.4184	0.6	6.96	0.255

The Stokes settling velocity, v_s, is estimated numerically based on the mean particle diameter and an empirical drag correlation (Morrison (2013)). Re_p is calculated as:

$$Re_p = \frac{v_s d_p}{\nu} \tag{4.2}$$

The friction velocity, u_*, is based on the critical stress calculated from the experimental data. Bagnold (2005) argued that for a mixture of particles, the sizes are quickly sorted and that the threshold value of the largest particles should be taken as the threshold for the mixture so the threshold stress is taken as the same for the large and mixed particles.

The commonly used model for predicting the critical stress is the Shields diagram (Shields (1936)). This classical diagram relates the wall shear stress to Re_p and an empirical curve for the threshold condition is found from experimental data. Figure 4.15 shows the measured values are systematically greater than the predicted values, however they present a similar trend. Widberg and Smith (1987) found that

the threshold curve varies significantly with the surface roughness, k_s. From their data, it can be observed that, the curve representing a surface roughness three times greater than the particle diameter shows a good agreement with the measured values. An evenly packed bed will have a ratio of D_p / $k_s = 1$, so this implies that the bed surface is not completely uniform on the scale of individual particles initially and that some particles are sheltered by their surrounding neighbors. The resolution of the surface height measurement is not sufficient to prove this, but since the particles are not completely uniform in size it is a reasonable explanation. The line of best fit for the measured values has a slope of -0.32, which agrees well with the -0.37 found by Bethke and Dalziel (2012).

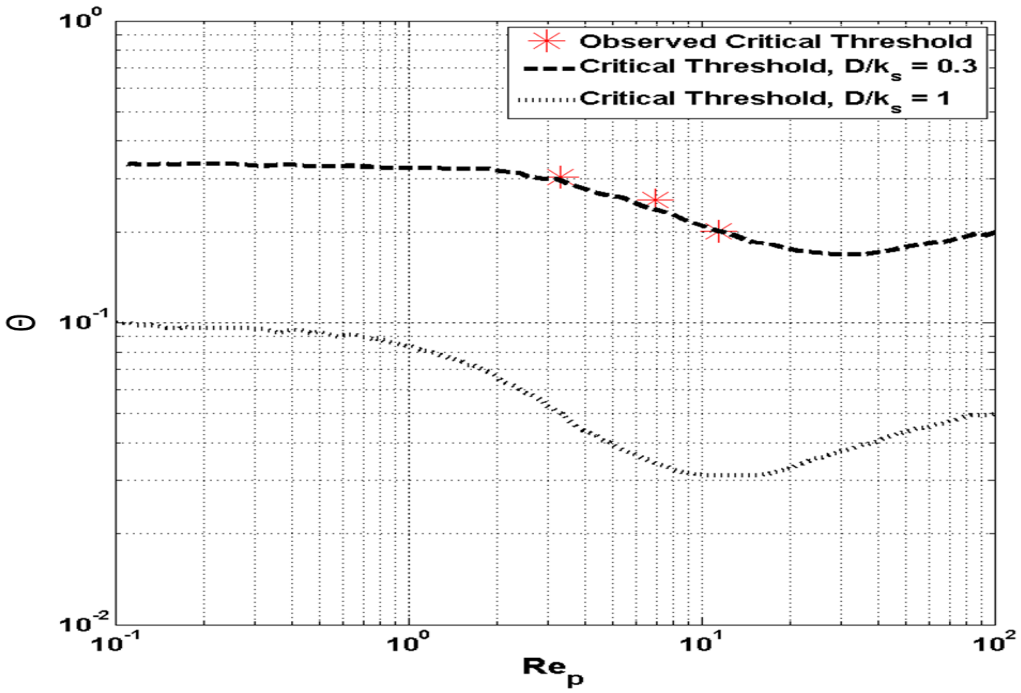

Figure 4.15: Shields diagram with measured θ_c (red stars) and the predicted curves by Widberg and Smith (1987)

Several methods have been proposed for relating the angle of repose of the particles to the critical stress required for motion. These models are based on the idea that the interparticle friction capable of maintaining the slope of a mound of particles is related to the stress required by a fluid to separate a grain from the bed. White (1940) measured the transport of particles in a channel flow and developed an empirical model for predicting the critical stress based on the angle of repose:

$$\tau_c = 0.18(\rho_p - \rho_f)gd_p tan(\phi) \tag{4.3}$$

Where ϕ is the angle of repose. In this study, the angle of repose was measured by allowing particles to settle into stationary mounds and then processed similarly to the elevation profiles in the next section. This method proposed by White (1940) however under predicted the measured values by an order of magnitude, similarly with the results of Bethke and Dalziel (2012). Julien (1995) later updated this model to include a stronger dependence on the particle size, resulting in:

$$\tau_{critical} = 0.25d_*^{-0.6}g(\rho_p - \rho_f)d_p tan(\phi) \tag{4.4}$$

Where:

$$d_* = d\left[\frac{(s-1)g}{\nu^2}\right]^{\frac{1}{3}} \tag{4.5}$$

Where ϕ is the angle of repose of the particles. This model however, under predicts the measured value by a factor of three and shows a decrease in the critical stress with increasing particle size. Even though the model is within the correction

factor for calculating the wall shear stress with the current PIV resolution, there is a clear trend in the current data that the stress required for motion increases with particle size.

The critical stress threshold is assumed to be constant with radial position, because the bed is nominally flat initially. As the bed deforms, particles on the lee slope will be easier to mobilize because a portion of their weight acts in the direction of the drag force exerted by the fluid. By the same reasoning, particles on the stoss slope are more difficult to mobilize. This suggests that the threshold value will vary along the bedforms and in time as the bedforms evolve. In the current work this effect cannot be quantified because the stresses are calculated for flow on a solid boundary in the absence of the mobile sediment bed.

The porosity of the bed presents another difficulty for comparing the stresses from a solid boundary. The solid boundary prevents flow penetration and imposes a global no-slip condition on the surface, either of which can play a significant role in the mobilization of sediment. Bethke and Dalziel (2012) found that for a bed of 90 μm particles there is an apparent slip velocity of the top layers that manifests as a free-slip condition at the macroscopic scale and that the low permeability of the bed limits the flow penetration. The data in the current work cannot discern the onset of bed load motion, so the results of Bethke and Dalziel serve as an explanation for the calculated values being higher than the empirical models.

4.3 Stress Available for Mobilization

Once the critical threshold has been exceeded, the additional stress imposed by the fluid acts to transport sediment. For this reason, typical sediment transport models are piecewise, with the predicted transport rate to be zero when the average stress does not exceed the critical conditions. This approach presents a problem when it is applied to flows, such the ones in the current work, with large fluctuations about the mean. Averaging the flow removes these large fluctuations and may yield a poor representation of the stress experienced by the bed.

This is made clear by Figure 4.16, which shows that for case D the time average stress lies below the critical stress calculated in section 4.2. Based on the traditional models, this flow would predict no sediment transport, however it will be shown in the next section it does cause significant transport. Looking at t/T=0.33, corresponding to the vortex/wall interaction, the phase-averaged stress peaks and exceeds the critical stress suggesting there would be sediment transport, which agrees with the results in section 4.5.

The onset of particle motion is an instantaneous process, so if at any point in time the stress exceeds the threshold value a particle will begin to move. Once motion has begun, the process becomes significantly more complicated by the suspension or bombardment of the particle onto the surface freeing others for suspension. Because of this, the determination of the stress available for transport must also be done instantaneously. Although the phase-averaged stress maintains most of the details of the vortex/wall interaction, the ensemble averaging process removes

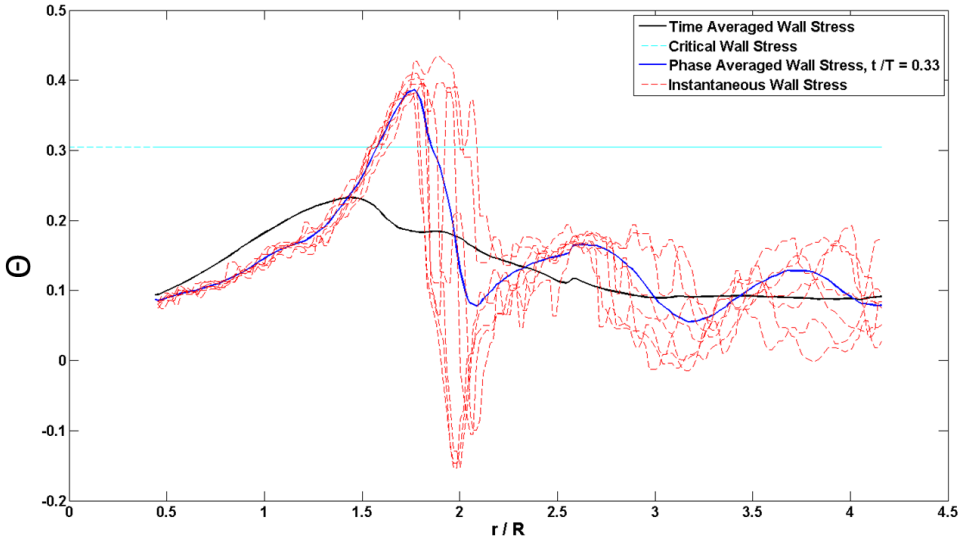

Figure 4.16: The time-averaged (black solid line) wall stress compared to the ensemble-averaged (blud solid line) and ten instantaneous (red dashed lines) wall stress profiles for t/T=0.33 of case D, overlapped by the critical stress for the 45-63 μm particle class(cyan dashed line).

the random fluctuations in the stress caused by the jitter in the vortex location and any smaller-scale structures that may be present. This presents a similar problem to the calculation of the circulation, which must also be done instantaneously.

Shown in Figure 4.17, all three low speed flow conditions produce time-averaged stresses that are below the threshold for the small particles. This highlights the need for a sediment transport model of near threshold condition flows to consider the role of the large-scale unsteady structures.

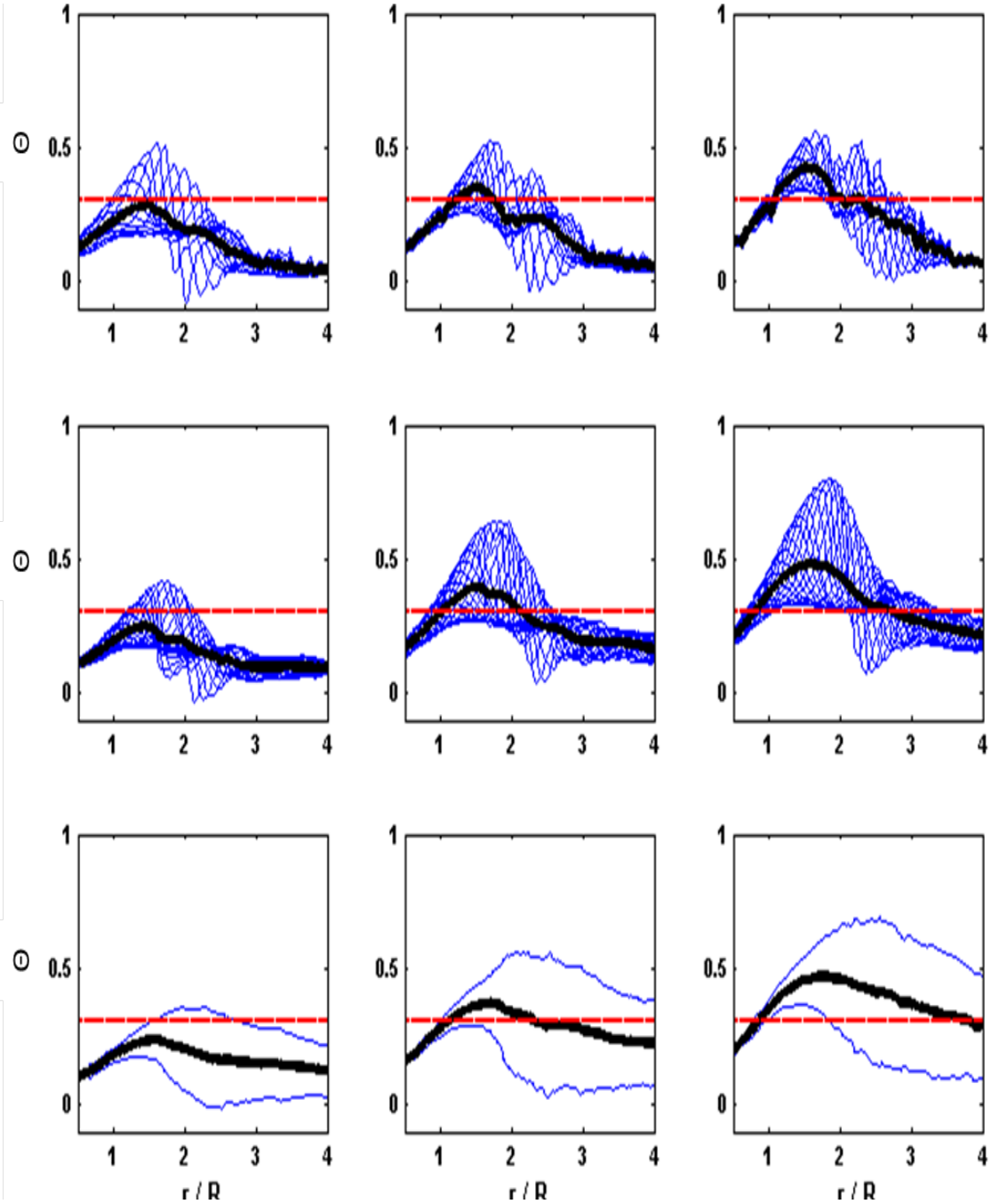

Figure 4.17: Profiles of the time-averaged (black solid lines), phase-averaged (blue solid lines) θ compared to the critical stress for the 45-63 μm particles. The plots are labeled according to the flow case, with g, h, i being the unforced flows. (The blue lines for the unforced cases represent stochastic fluctuations, as the data is not phase locked)

4.4 Prediction of Sediment Transport

Bagnold (1966) proposed a model for relating the rate of work done by the fluid on the sediment to transport it from the bed surface. The model is derived from the general form of the power equation:

$$i_t = (\rho_p - \rho_f) g V U_p = \omega_f \epsilon \tag{4.6}$$

Where i_T is the total net energy transport rate, V is volume of particles, U_p is the velocity of the transported particles, ω_f is the available fluid power, and ϵ is the efficiency at which the fluid power is converted to work on the particles. Equation 4.6 states that the total net energy transport, i_T it, is equal to the product of the available flow power (ω) and an efficiency. The available flowstream power is given by:

$$\omega_f = (\tau - \tau_c) \delta A u_f \tag{4.7}$$

Where $(\tau - \tau_c)$ is the available excess bed shear stress applied to unit area δA and u_f is the fluid velocity just above the bed. This equation is true only for $\tau > \tau_c$ and is taken as zero for $\tau \leq \tau_c$. The thresholding operation is a nonlinear process, and as was shown in the previous section, it should logically be applied to each instantaneous measurement of the bed shear stress to account for the periodic and stochastic fluctuations within the flow. When combined with equation 4.6 the equation becomes:

$$(\rho_p - \rho_f) g V U_p = \epsilon (\tau - \tau_c) \delta A u_f \tag{4.8}$$

Given the difficulty in resolving the U_p and u_f, Bagnold argued to arrange them in the form of a slip ratio (U_p/u_f). This ratio is likely greater than one because the transfer of stress from the fluid to solids involves a local dissipation of energy, in other words, for equilibrium conditions assumed, the particles do not on average travel faster than the fluid surrounding them. This is not the case if there is a significant relaxation region in which the inertia of the already mobilized particles causes them to move faster relative to the surrounding flow. Bagnold proposed this ratio should be approximately equal to one in the absence of particle-particle or particle-bed interactions.

Bagnold proposed separate efficiency coefficients for the bed load and suspended load contributions. Quantifying both efficiency coefficients is not possible in the current work, as the measurements are conducted with a stationary surface elevations being used to represent the transport rate of sediment. As a result, , the two coefficients are replaced with a single empirical constant . Reducing the transport to a single mode simplifies the flow model considerably. Finally, the slip ratio will also be assumed constant, and combined with the efficiency, into one coefficient C, which will be empirically fit from the data. The equation then takes on the form of a force balance:

$$(\rho_p - \rho_f)gV = C(\tau - \tau_c)\delta A \tag{4.9}$$

The left hand side represents the weight of the particles and the right is the excess fluid force available on the exposed bed surface, reducing the equation to a force balance. The volume of particles can be expressed as the exposed surface area δA

times an incremental layer of thickness δh. Only a portion of the incremental layer is comprised of particles, due to the loose packing, so the weight of this layer is scaled by the packing factor ϕ. For loosely packed spheres an estimate of $\phi = 0.5$ is typically used, however the true packing factor is not known for the bed in the current work. On a local basis, the equation is rearranged to solve for delta and becomes:

$$\delta h = \frac{C(\tau - \tau_c)}{\phi(\rho_p - \rho_f)g} \tag{4.10}$$

The incremental thickness, δh, represents the thickness of particles expected to be transported by the available excess stress, $(\tau - \tau_c)$. This equation is then averaged over one cycle, representing one vortex pass and given an overbar to indicate it is a time-average. This departs from the original application of the model by Bagnold, in which he applied an empirical form for the fluid stress:

$$\tau = a(\overline{u} - u_c)^n \tag{4.11}$$

Where a and n are empirically fit constants. As was shown in the previous section, comparing the time-averaged velocity, $\overline{u}$, to the threshold velocity, u_c, is insufficient in this flow because the time-averaged velocity may not exceed the threshold but the phase-averaged or instantaneous velocities do. For this reason, equation 4.10 is evaluated for each instantaneous measurement of the bed shear stress, non-dimensionalized into Shields parameter, and then averaged over the number of realizations (N) and the number of phase angles (PH). The equation then takes the

form:

$$\overline{\delta h} = \frac{C d_p}{\phi} \frac{1}{PH} \sum_{ph=1}^{PH} \left[\frac{1}{N} \sum_{i=1}^{N} (\theta - \theta_c) \right] \tag{4.12}$$

The result has the units of length, however by averaging over one vortex cycle it can be viewed as the local thickness of particles that can be removed by one vortex. The quantity $\overline{\delta h}$ can be multiplied by the forcing frequency, f, to get a dimensional (i.e. per second) scour rate, which can then be non-dimensionalized similarly to traditional channels flows by:

$$\overline{\delta h_i^*} = \frac{\overline{\delta h_i} f}{d_p \sqrt{\left(\frac{\rho_p}{\rho_f} - 1\right) g d_p}} \tag{4.13}$$

This treatment of the averaging process reatains a more meaningful contribution of the stresses caused by each vortex, resulting in a higher predicted transport rate. Figure 4.18 compares the predicted erosion rates by for cases D-F, calculated by instantaneous thresholding (denoted by the subscript i) and the time-averaged thresholding (denoted by the subscript t), given by:

$$\overline{\delta h_t^*} = \frac{C f}{\phi \sqrt{\left(\frac{\rho_p}{\rho_f} - 1\right) g d_p}} (\overline{\theta} - \theta_c) \tag{4.14}$$

As expected the time-averaged thresholding is always less than the instantaneous, however there are regions of the flow for which the time-averaged threshold fails to predict any erosion. In the low speed case, as noted in the previous section, the time-averaged

thresholding also fails to capture regions of excess stress downstream of r/R=2, where the stochastic components due to the vortex breakdown become dominant.

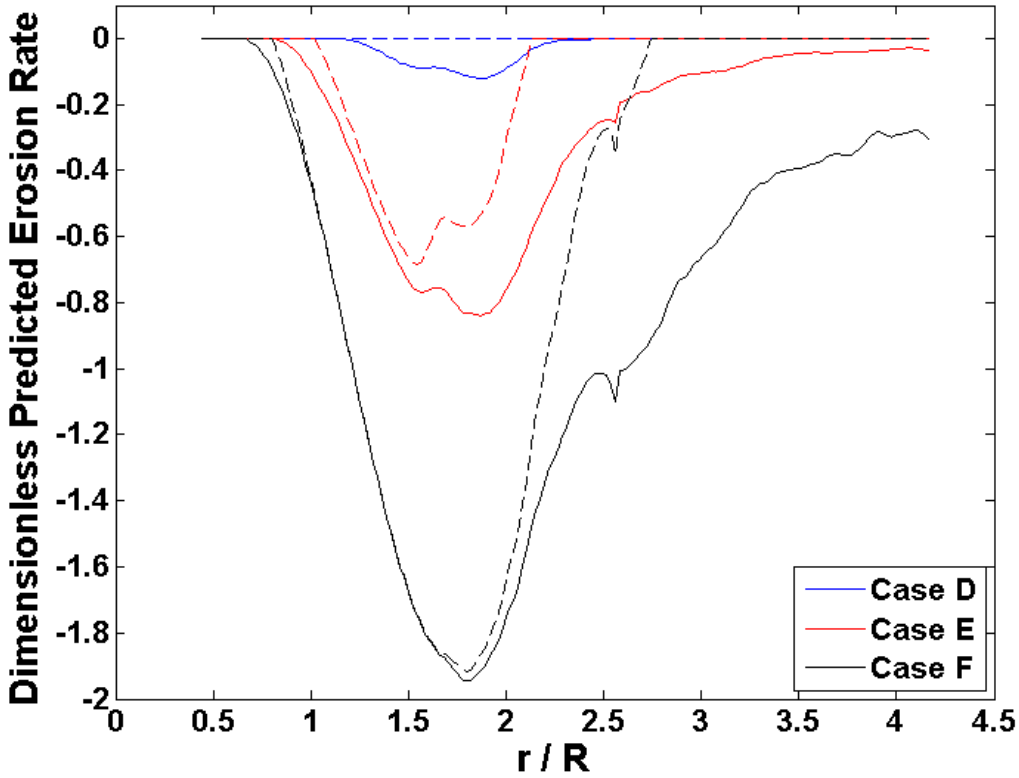

Figure 4.18: Predicted local erosion rate profiles comparing the instantaneous (solid lines) and time-averaged (dashed lines) thresholding methods.

The quantity $\overline{\delta h_i^*}$ can be integrated over the domain to yield the total predicted change in volume, or the non-dimensional net erosion rate:

$$\overline{\Phi^*} = 2\pi \int_{r=0}^{R} \overline{\delta h^*} r \delta r \tag{4.15}$$

The bulk dimensionless erosion rates predicted by the two thresholding methods for each case are displayed in Table 4.2.

Several observations can be made from Table 4.2. For five out of the twelve

Table 4.2: Predicted erosion rates for all test conditions

Flow Case	Particle Size	Θ_c	$\bar{\Phi}_t$ (x 10^{-6} m^3 / s)	$\bar{\Phi}_i$ (x 10^{-6} m^3 / s)	$\bar{\Phi}^*_t$	$\bar{\Phi}^*_i$	Θ_{range}
A	54 μm	0.305	4.28	7.50	0	0.1322	[0.51, -0.08]
B	54 μm	0.305	6.61	21.30	0.1165	0.3755	[0.52, 0.03]
C	54 μm	0.305	44.20	78.61	0.7794	1.386	[0.56, .05]
D	54 μm	0.305	0.00	4.28	0	0.0755	[0.42,-0.03]
E	54 μm	0.305	26.20	55.69	0.4619	0.9820	[0.64, 0.04]
F	54 μm	0.305	112.13	174.74	1.977	3.081	[0.80, 0.08]
$D_{Unforced}$	54 μm	0.305	0.00	0.52	0	0.0091	[0.24, 0.10]
$E_{Unforced}$	54 μm	0.305	13.99	40.92	0.2466	0.7215	[0.38, 0.15]
$F_{Unforced}$	54 μm	0.305	109.74	144.11	1.935	2.541	[0.47, 0.19]
E	105 μm	0.201	0.00	18.65	0	0.1213	[0.64, 0.04]
F	105 μm	0.201	18.08	59.44	0.1176	0.3865	[0.80, 0.08]
E	87.5 μm	0.256	0.00	19.33	0	0.1741	[0.64, 0.04]

conditions tested the time-averaged stress does not exceed the threshold, so there is no predicted erosion. In the cases which the time-averaged stress does exceed the threshold, $\overline{\delta h_t^*}$ is up to a factor of two less than $\overline{\delta h_i^*}$. The relative strength of each flow is given as a range of stress experienced throughout one cycle:

$$\theta_{range} = [max(< \theta(r, i, ph) >), min(< \theta(r, i, ph) >)] \tag{4.16}$$

The relative strength of a flow can be used to predict the types of bedforms it will produce. For flows with $\theta_c < \theta < 0.8$, bedforms resembling vortex ripples are expected to be present, however for $\theta > 0.8$ the bedforms are rapidly eroded and the surface begins to resemble sheet flow (Amoudry (2008)). However this flow exhibits a range of θ so this is likely not a simple comparison, but it does show that sheet

flow conditions may be present during some of the cycle even though the surface resembles vortex ripples.

4.5 Erosion Measurements

The results presented so far have shed light on the stresses available for sediment transport throughout the vortex/wall interaction, and served to predict the erosion. To establish how effectively this model predicts the erosion, a series of complimentary experiments were performed to capture the surface evolution and the rate at which the surface is eroded.

he surface profile measurements for case SP_E are shown in detail in Figure 4.19. The erosion begins around r/R = 2.1, just downstream of the peak tractive stress (r/R = 1.9), with a crest and a second trough forming downstream of the first. The reduced depth of the second trough is to be expected due to both the reduced coherence of the primary vortex ring and the deceleration of the axisymmetric wall jet as it expands radially. The wavelength of the initial crater is λ/R = 1.5 and grows throughout the development to λ/R=2 as progressive scouring of the trough moves the crest downstream. The lee slope of the crater remains nominally constant throughout the development, and remains significantly below the angle of repose of the particles. If the slope was close to the angle of repose, there would be significant errors in measuring the surface elevation in the absence of the flow due to the particle settling to an equilibrium position.

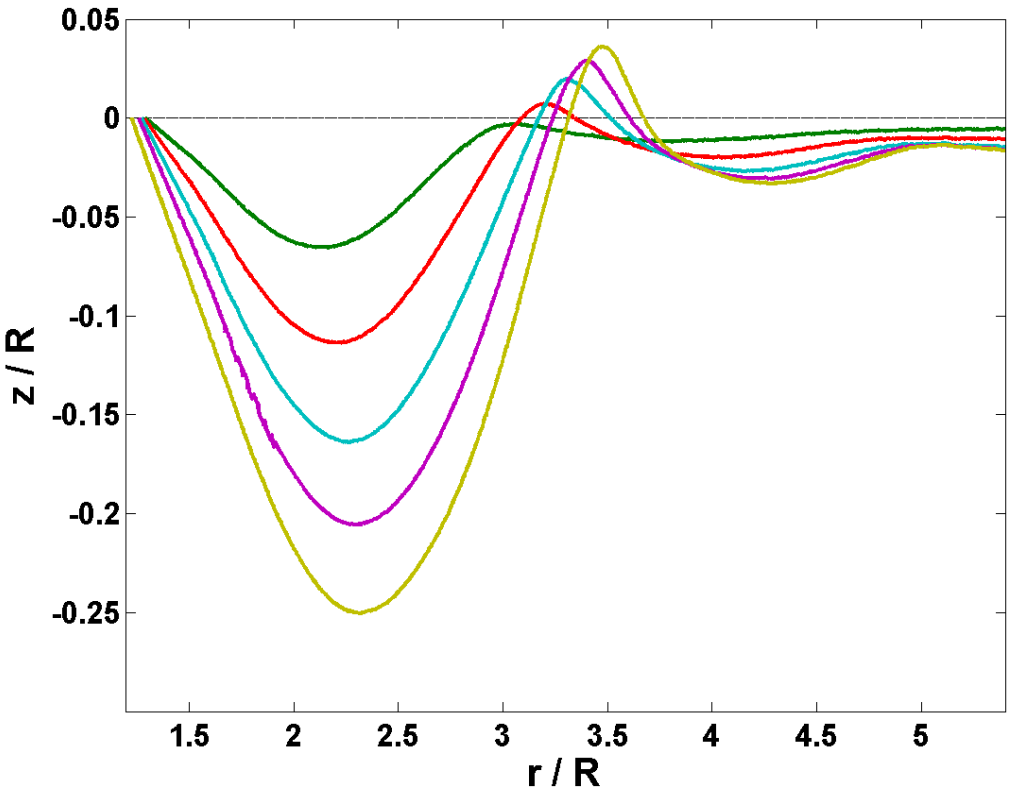

Figure 4.19: Time evolution of the bed surface profile for case SP_E, there 750 vortex passes between each progressive profile.

This development is similar for cases $SP_E - SP_F$, shown in Figure 4.20 with case SP_D stopped early. As expected, the self-similar development of the bed forms mirrors the self-similar stress profiles. For cases $SP_A - SP_C$ the end-of-run bed profiles are significantly different, showing a significantly longer wavelength for the high- speed case.

For case SP_C, the extended wavelength of the final crater could be explained by the relative strength of the vortex to the mean flow being the weakest or by the increased vortex spacing altering the trajectory and keeping the vortex further from the wall for a longer period. Thus the mean flow is responsible for the majority of the downstream scouring.

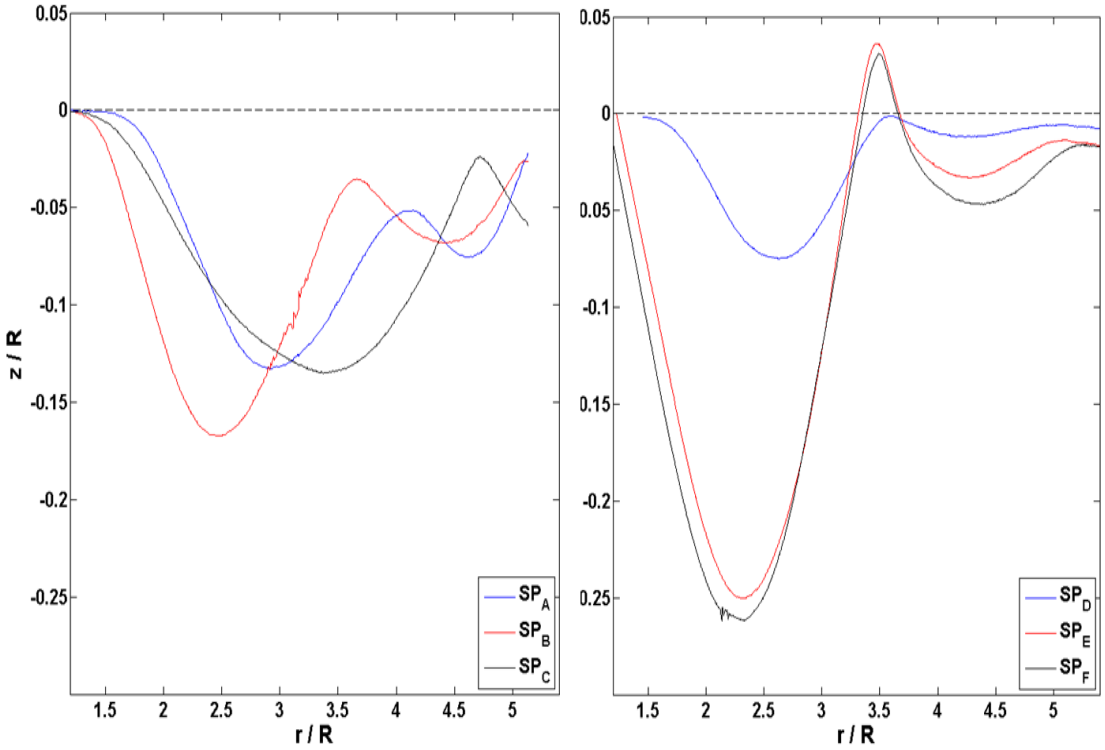

Figure 4.20: End-of-run elevation profiles for $SP_A - SP_C$ (left) and $SP_D - SP_F$ (right)

Comparing the end-of-run profiles (taken at similar times) for cases SP_E and SP_{Eu} (Figure 4.21) reveals that the forcing results in a similar initial crater, but a significantly reduced depth of the second crater. This is also seen in the profiles of the excess stress seen in the previous section, in which the stress in the forced case drops off significantly beyond r/R=2.6, while the stochastic component of the unforced flows remains significant downstream of this point. This is likely due to the stable rebound of the vortex in the forced cases, while the vortex trajectories in the unforced flow have a greater variability and do not display significant rebound.

The denudation rate is defined simply as the rate of removal of particles from the bed surface, and is calculated locally by subtracting successive profiles to find

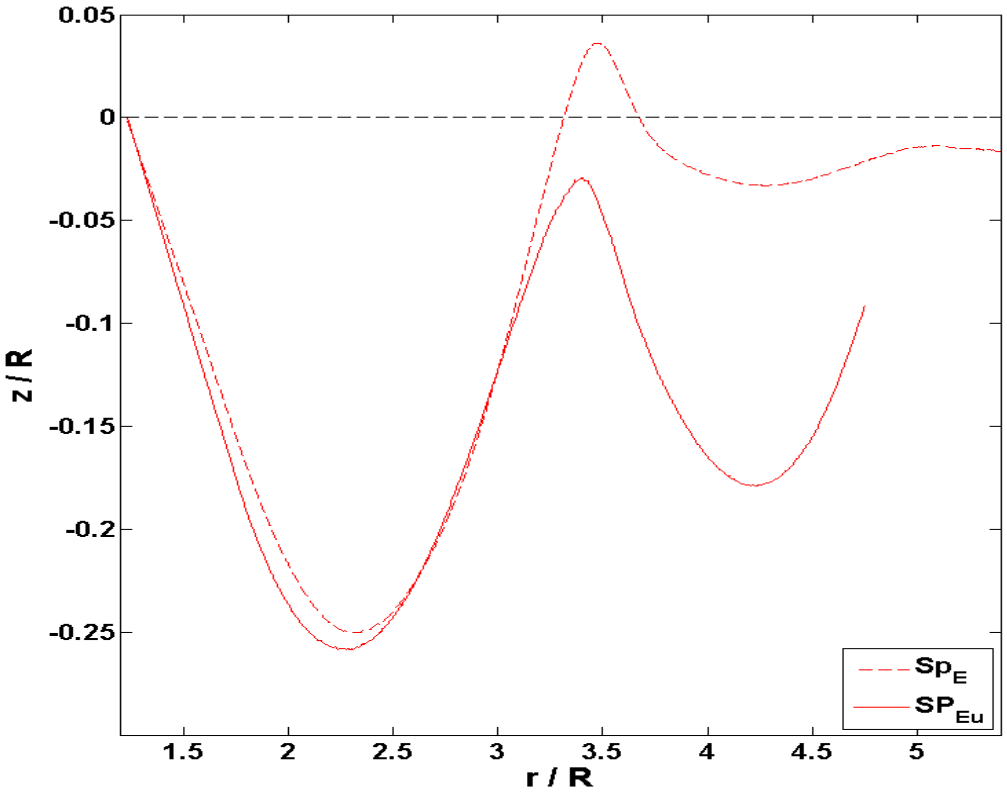

Figure 4.21: End-of-run profiles for cases SP_E and SP_{Eu}, highlighting the significant reduction in erosion downstream of the first crest in the forced flow

the difference in the elevation divided by the number of vortices that have passed during that time interval (Figure 4.22). The denudation is non-dimensionalized by:

$$\Delta^* = \frac{\delta h}{tfR} \tag{4.17}$$

Non-dimensionalizing the denudation rate by the forcing frequency indicates the amount of sediment transported per vortex. This clearly reveals two maxima in the surface erosion rate at the earliest times located near the center of the nascent forming troughs (r/R=2.2 and r/R=4). After the initial bed form is created, the scour remains nearly constant for the upstream crater suggesting the scouring pro-

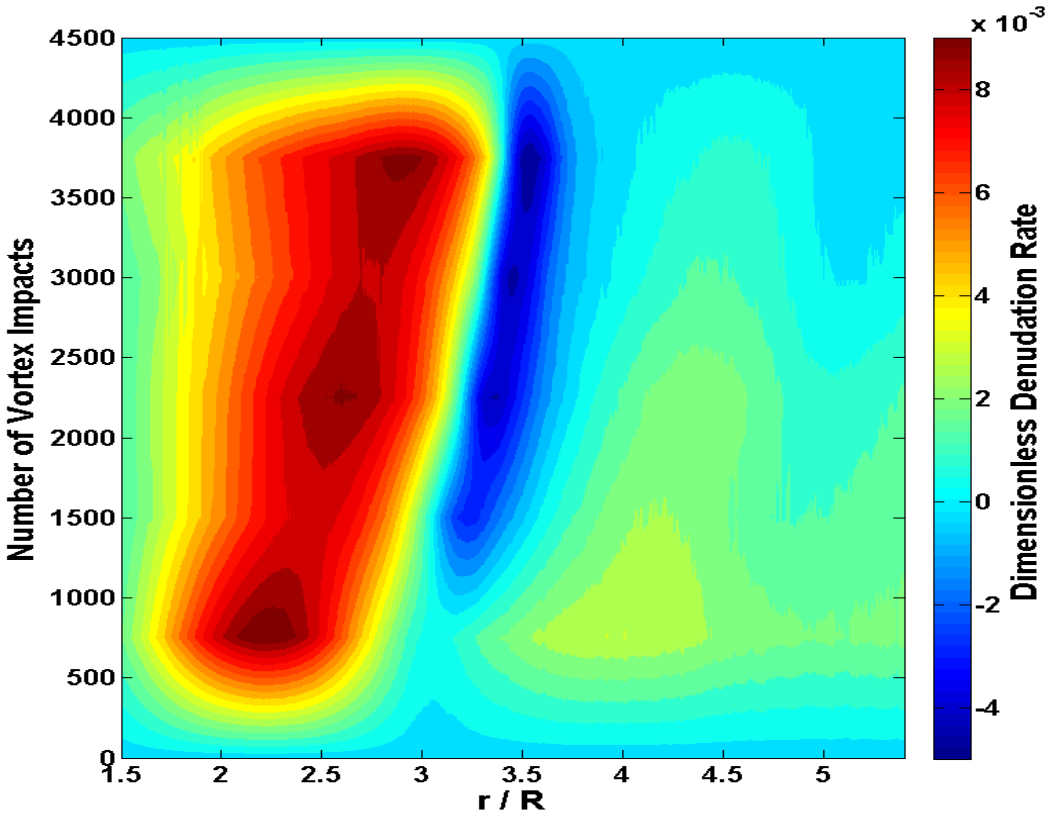

Figure 4.22: Contours of the denudation rate (Δ^*) for case SP_E

cess reaches an equilibrium rate. There is a slight reduction in the scour of the downstream crater throughout the evolution, however the magnitude of the scour downstream is small compared to that of the initial crater.

The difference between the elevations of the surface after a number of vortices have passed and the initial surface can be integrated over the radial direction to get the net amount of sediment removed by the vortex passes. As shown in Figure 4.23, there is a constant removal rate of particles after the initial transient period, which is observed in all forced flow conditions. This period is associated with the initial development of the craters, but the temporal resolution of the elevation measurements does not allow for a more detailed explanation for the initial transient. After

this period however, the slope of the line of best fit can be extracted as the erosion rate, Φ_V. The repeatability of the surface profile heights from test-to-test propagate to variability ($\delta\Phi$) in the erosion rate of up to 30%, although the mean of all tests is closer to 15%.

The erosion rate is representative of the transport rate of sediment away from the surface per vortex pass, but does not allow for the separation of bed and suspended load contributions. Kiger *et al.* (2014) found that for an initially flat bed of sediment exposed to a similar flow the transport layer is much thinner than for a previously eroded bed, suggesting that either the primary erosion had not yet occurred or was occurring too close to the bed to resolve with PIV, suggesting primarily bed-load transport.

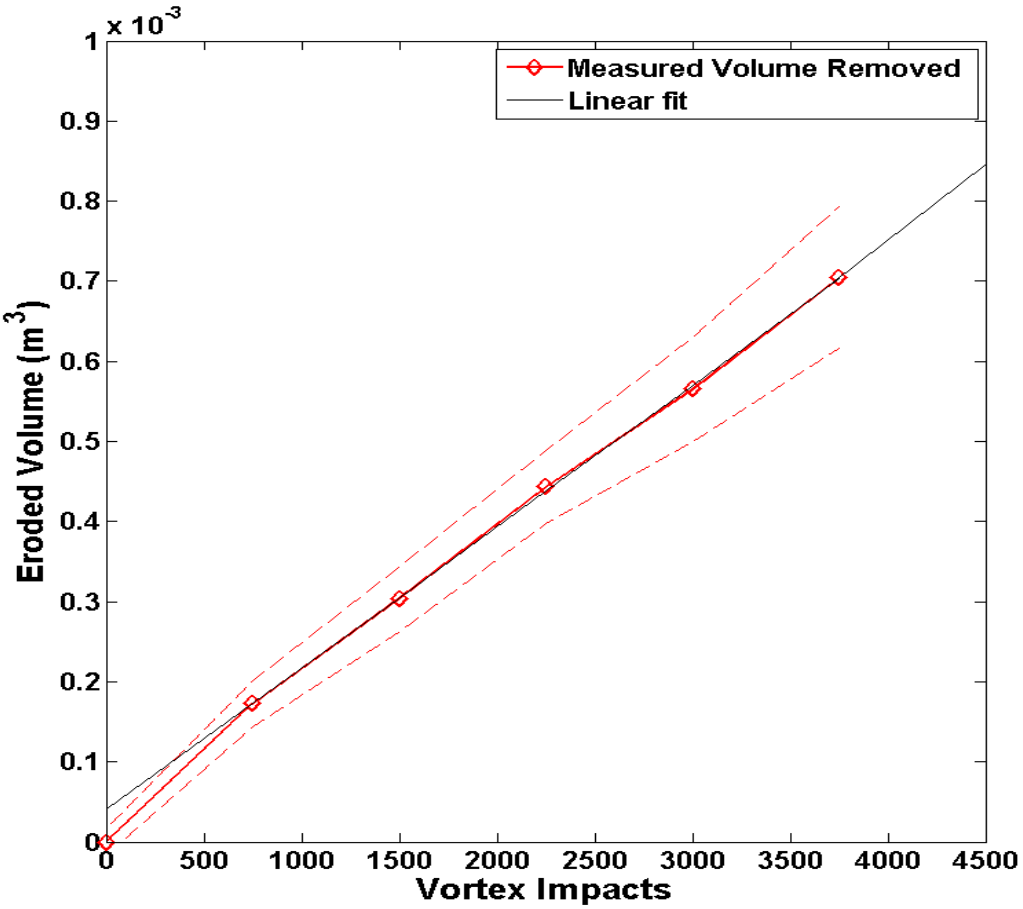

Figure 4.23: Total volume removed throughout evolution of the bed forms showing the development of a quasi-equilibrium condition with a constant removal rate. Dashed lines show the range of possible values, based on one standard deviation from 10 repeated trials.

The non-dimensional erosion rates for all cases are calculated and detailed in Table 4.3. The erosion rates for case SP_C is a factor of five greater than that of case SP_A (Figure 4.24), while the circulation is held constant and the mean flow only increases by a factor of two. For case SP_F, the erosion rate is a factor of fifteen greater than that of SP_D, while both the circulation and the mean flow are increased by a factor of two. This suggests that there is a nonlinear relationship between the flow quantities and the transport of particles and that the roles played by the mean

flow and the vortex are intrinsically coupled.

Table 4.3: Erosion rates for all test conditions

Case	Φ_V (x 10^{-6} m^3/vortex)	$\Phi_t = \Phi_V f$ (x 10^{-6} m^3/s)	Φ_t^*	$\delta\Phi$ (%)
SP_A	0.0800	2.79	0.148	13.75
SP_B	0.1180	6.50	0.344	12.46
SP_C	0.1890	14.20	0.751	11.41
SP_D	0.0170	0.59	0.031	18.17
SP_E	0.1770	8.83	0.467	10.87
SP_F	0.2720	17.68	0.935	7.54
SP_{Du}	0.0056	0.99	0.052	37.72
SP_{Eu}	0.0538	15.61	0.826	13.92
SP_{Fu}	0.0734	24.675	1.305	11.63
LP_E	0.1180	5.92	0.313	27.87
LP_F	0.2640	17.15	0.907	2.62
MP_E	0.0830	4.13	0.218	11.16

Although the eroded volume per vortex for the unforced cases is a factor of 2.5 less than the corresponding forced cases, the increased shedding frequency results in more erosion per second than in the forced cases. This suggests that the forcing acts to reduce the overall transport of sediment compared to the random shedding events associated with the unforced jet. This is exacerbated by the increased erosion downstream of the edge of the field of view, which is not included in the measured erosion rate. This is an interesting result because the unforced flow contains weaker vortices that shed more frequently at a similar mean flow to the corresponding

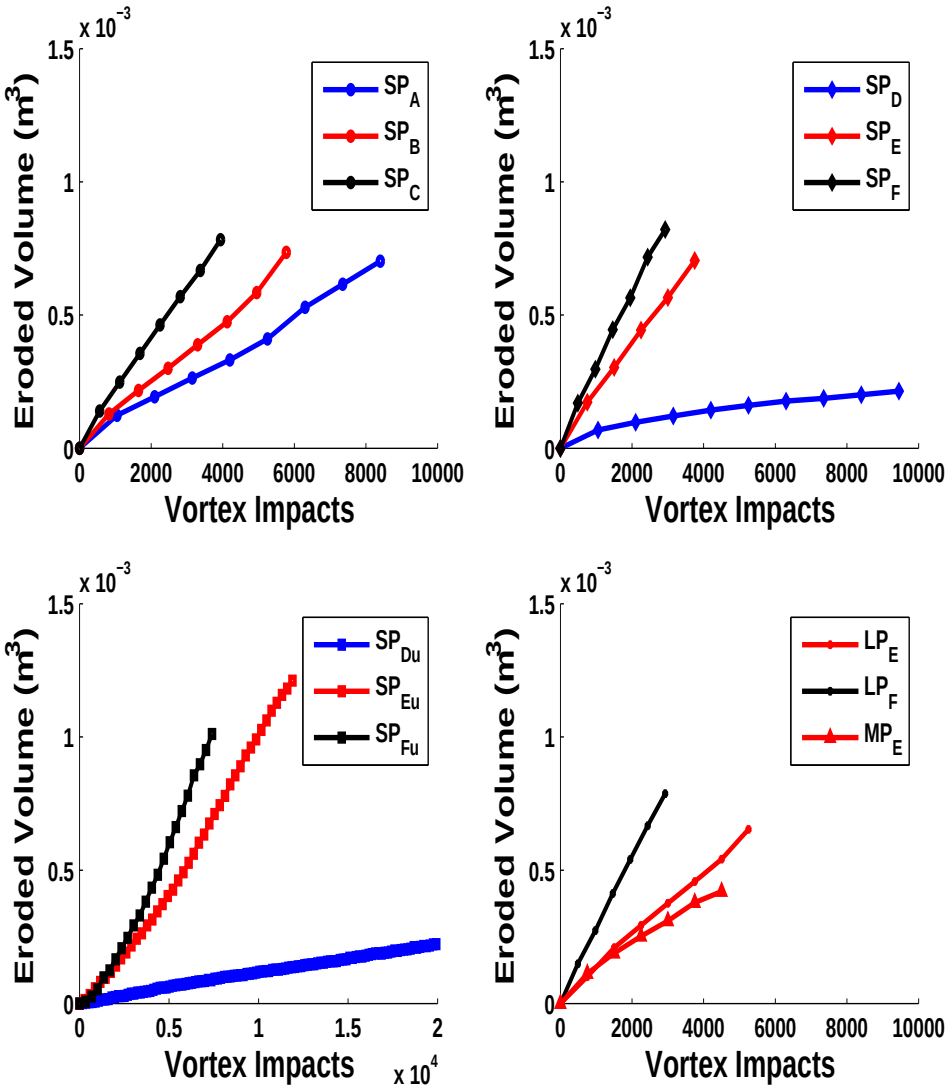

Figure 4.24: Removed volume over time for test conditions $SP_A - SP_C$ (top-left), $SP_D - SP_F$ (top-right), $SP_{Du} - SP_{Fu}$ (bottom-left),$LP_E - LP_F$ and and MP_E (bottom-right).

forced condition. This is most likely caused by the reduced loss of coherence of the primary vortices in the unforced jet resulting in greater stresses on the bed further downstream, which is weightly more heavily in a cylindrical coordinate system.

The effect of increasing particle size can be seen in Figure 4.25 showing the net eroded volume for two particle sizes with the same imposed flow conditions.

Interestingly the net dimensional erosion rate for the high speed case is similar for both particle sizes. Although the imposed stress is the same in both cases, the threshold stress for the larger particles is greater, resulting in a reduced excess stress available for sediment transport. This result suggests that there exists a saturation limit as the additional available stress for the smaller particles at the highest speed case does not result in additional erosion . The larger particles also show a reduced initial transient.

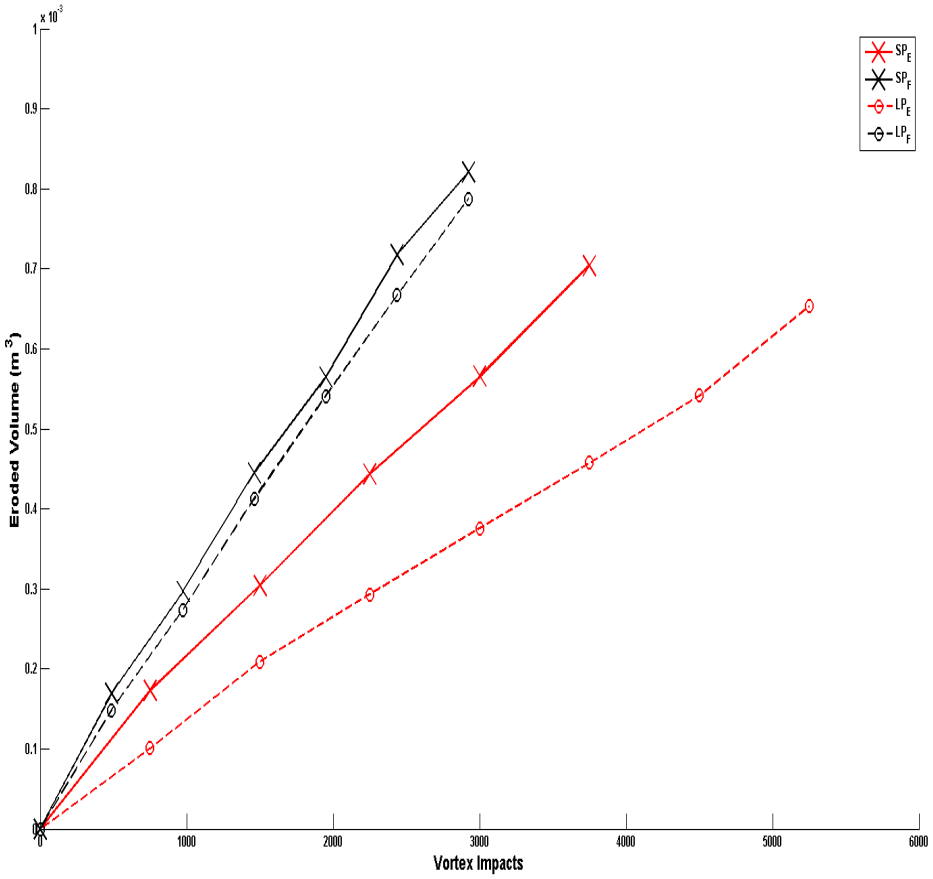

Figure 4.25: Net eroded volume comparing the smaller particle size (solid lines marked with xs) and the larger particles (dashed lines marked with open circles).

4.6 Single-Phase Measurements on Bedforms

This section details the single-phase PIV measurements on the prototype bedform, showing the changes in the fluid dynamics when imposed on a non-unform surface. The time-averaged flow remains nominally similar on the prototype bedformr with an acceleration of the flow away from the stagnation point, which gives way to deceleration due to radial expansion (Figure 4.26). The region just beyond the initial crest is sheltered, resulting in lower flow velocities near the bed than in the flat plate.

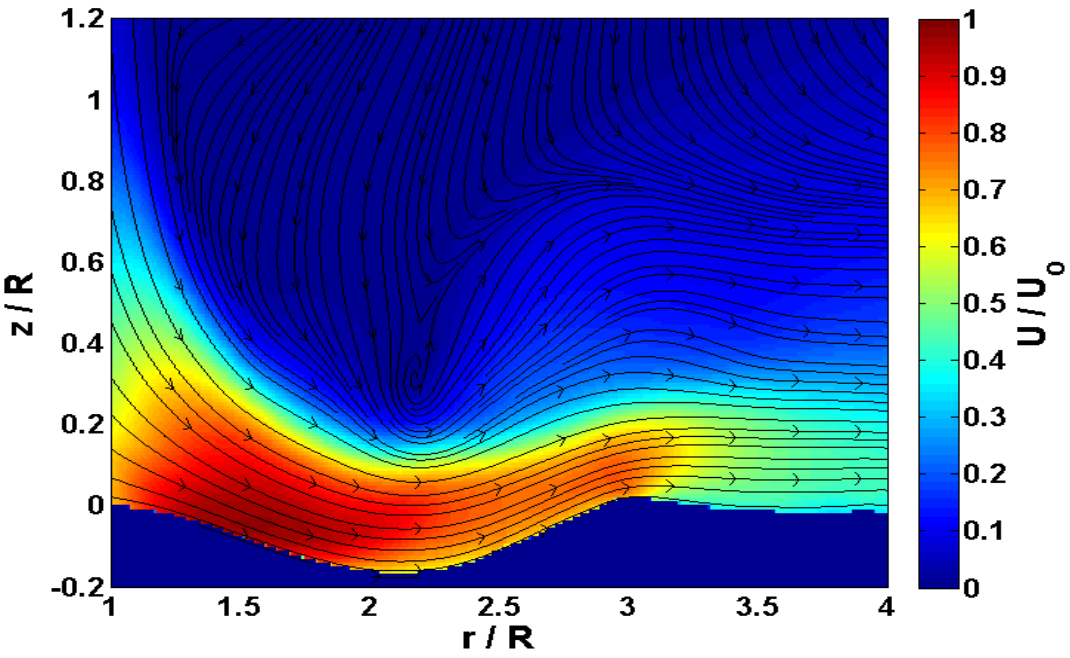

Figure 4.26: Time-averaged contours of u_r overlapped by the streamlines for the prototype bedform

The same vortex tracking algorithim was applied to find the new vortex trajectory and circulation development. Figure 4.27a, which defines the height from the local surface as opposed to a fixed reference, shows that the vortex remains close to the surface and does not rebound as significantly from the surface as in the flat plate. The secondary vortex is then pushed through the crater as opposed to lifted away from the surface and wrapped around the primary. The secondary vortex in these experiments is more difficult to track with the current method because it does not separate from the shear layer on the surface. As the primary vortex approaches the crest (r/R=3) the secondary vortex begins to lift away from the surface slightly, but does not reach as high into the flow as in the flat plate.

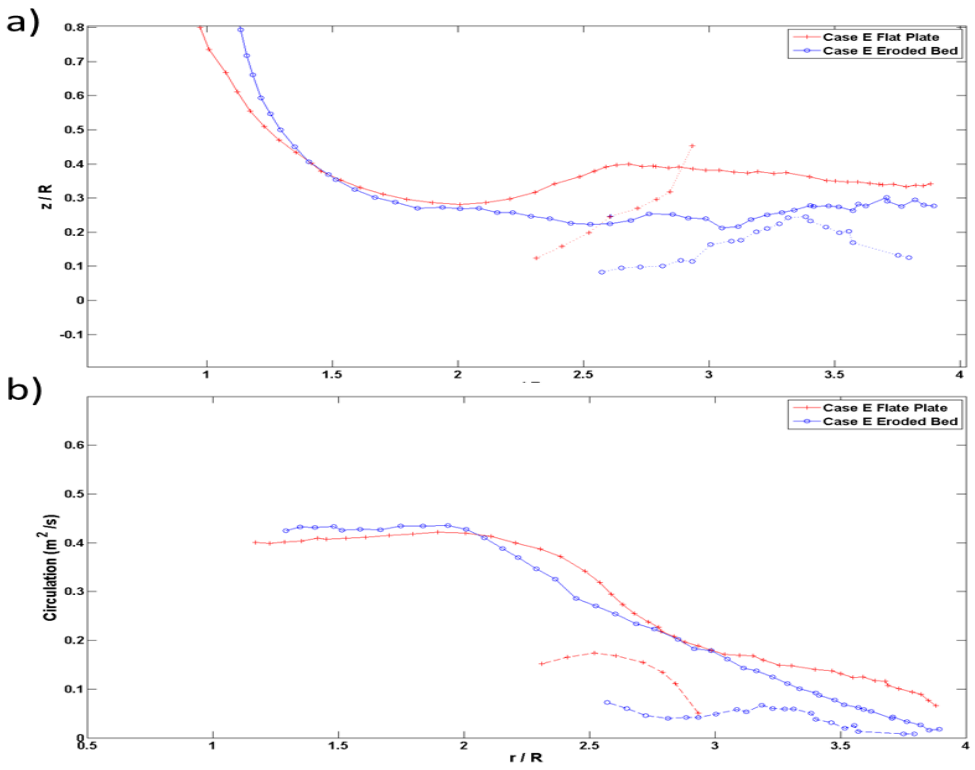

Figure 4.27: Comparison of the vortex trajectory (a) and the circulation develpement (b) for the flat plate and the eroded bed.

The circulation decays much more gradually when imposed on the eroded bed, also representative of the reduced vortex rebound. The secondary vortex is consistently weaker than in the flat bed case and remains coherent further downstream. There is a region just downstream of the crest (r/R=3) where the secondary vortex is strengthened briefly. This may shed some light on the development of the second crater, which cannot be explained by the flat plate measurements.

The phase-averaged vorticity and stress are shown in Figure 4.28. The primary vortex begins interacts with the ground at about the same point as the flat plate, with the secondary vortex becoming coherent around r/R=2. The peak stress induced on the surface throughout the interaction is reduced by 16%. However because the primary vortex remains close to the surface further downstream the stress does not decay as much as in the flat plate.

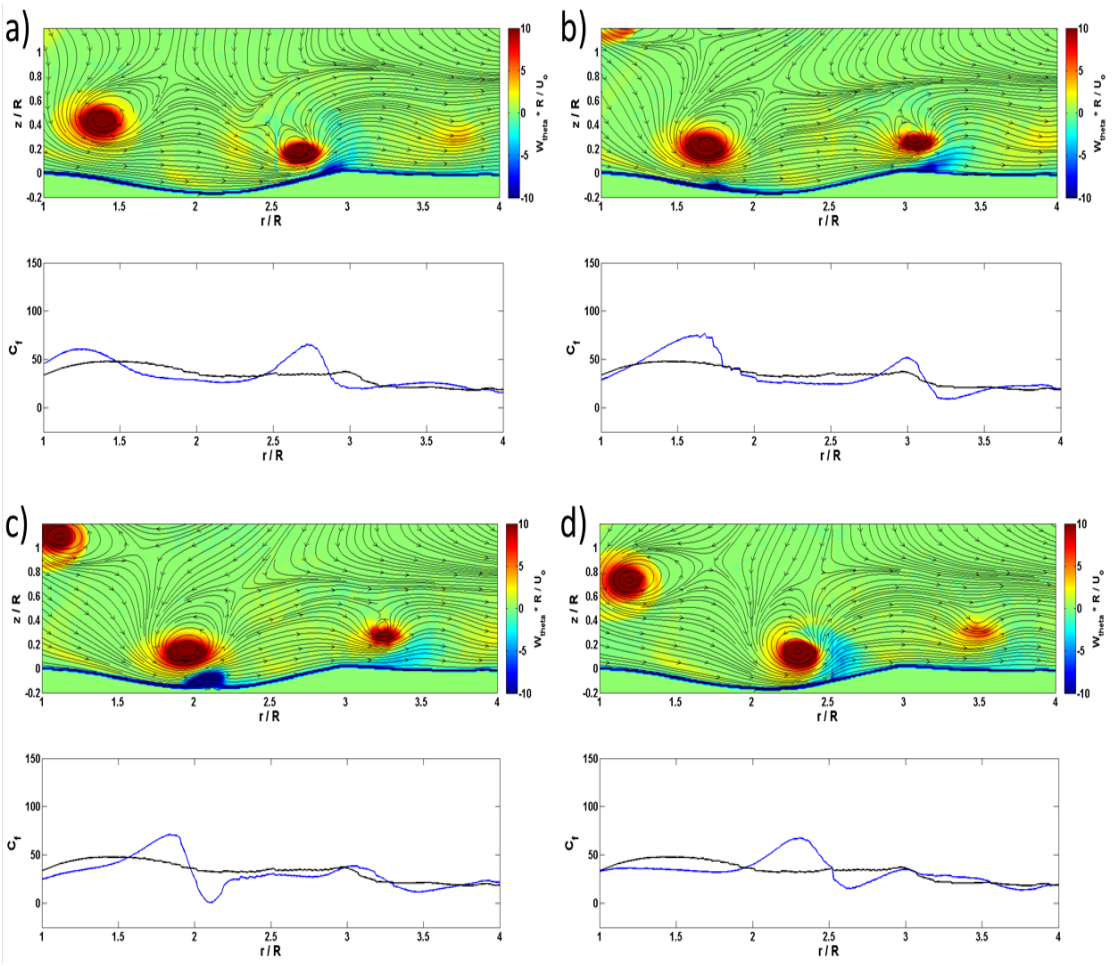

Figure 4.28: Contours of phase-averaged vorticity with overlapped streamlines and the corresponding wall stress profiles for t/T = 0.06 (a), 0.33 (b), 0.61 (c), 0.89 (d)

The reduced phase-averaged stress can be seen in Figure 4.29. Although the peak value is less, the stress is more evenly distributed remaining significantly above the time average for $1 \geq r/R \leq 3$. In the flat plate the stress has begun to drop off by about r/R = 2.5. Downstream of r/R = 3, the stress on the eroded bed decreases significantly as the primary vortex passes over the crest.

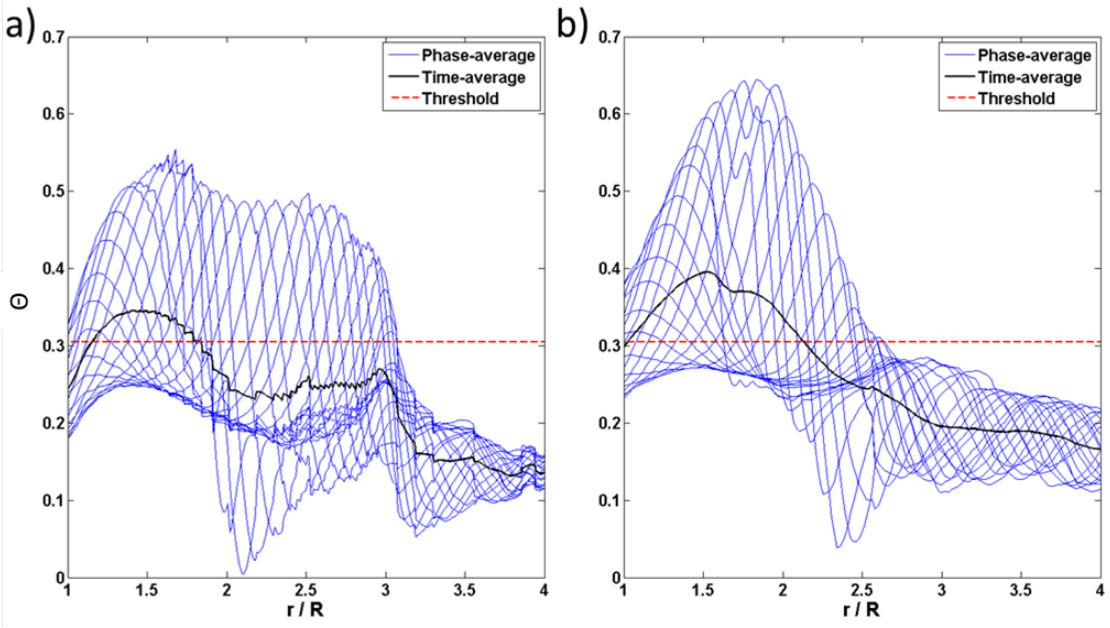

Figure 4.29: Profiles of the phase-averaged (blue lines) and time-averaged (black lines) stress profiles comparing the flow over the prototype bedform (left) and flat plate (right), with θ_c (red dashed lines)

Interestingly the integrated excess stress on the eroded bed is 35% greater than the flat plate because it is more evenly distributed over the bed with a weaker peak value but persists further downstream (Figure 4.29). This is unexpected as the erosion measurements suggest that the erosion rate decreases after the bedforms develop. Traditional time-averaged thresholding methods result in the opposite trend, because the integrated excess time-average stress is less than in the forced case.

4.7 Evaluation of the Proposed Model

To evaluate the effectiveness of the model proposed in section 4.4, the predicted values are compared to the observed erosion rates from table 4.3. For comparison to the other models discussed in Chapter 2, Φ_t is non-dimensionalized similarly to δh. Figure 4.30 shows that the model performs well for the cases with lower excess stress, i.e. the lower speeds and the larger particles. The empirical constant C representing the efficiency of momentum transfer from the fluid to the particles and the slip ratio is left as unity for the values in Figure 4.30. This is because as the excess stress increases, the model begins to significantly over predict the observed erosion rate suggesting a linear fit is not appropriate. This kink in the trend appears within each scaling set of conditions, with the highest speeds significantly over predicting the erosion rate compared to the corresponding low speed.

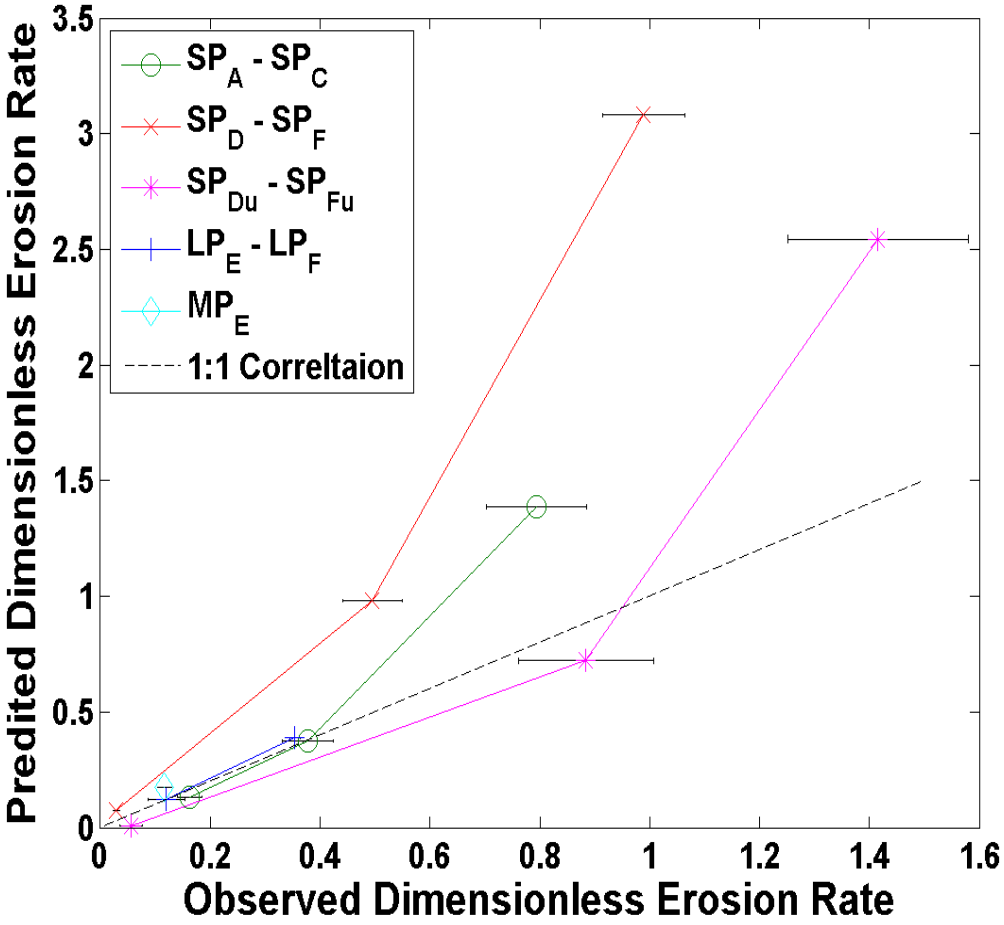

Figure 4.30: Comparison of the predicted and observed bulk erosion rates, with error bars representing the repeatability of the observed erosion rates. (The error bars assocated with the uncertainty in the predicted stress measurements are neglected as they are an order of magnitude smaller than the observed erosion rates)

One possible explanation for this is flow saturation. The similarity of the erosion rates for the high speed flow (case F) for both particle sizes suggests that the additional excess stress available for the transport of the smaller particles does not result in more erosion. Alternatively the excess stress could cause the already mobilized particles to accelerate, but this cannot be quantified with the current data. Based experimental data of statistically steady flows presented by Durán and Andreotti (2011), the mass flux of particles approaches a saturation limit proportionally by u_*^2. The saturation limit was also found to vary with particle size. Since the current work presents the single-phase flow independent of the sediment, this effect is not accounted for in the predicted erosion rate and may result in the over prediction of the highest speed cases.

Another possible explanation for the kink in the data is the choice of the θ_c. In section 4.2 it was shown that there is a range of possible values that may exist. The choice of θ_c has a nonlinear effect on the predicted erosion rate so a range of θ_c is tested to quantify it. A range of 20% was chosen because it represents the difference in the methodologies presented in section 4.2. As shown by Figure 4.31, the range of predicted erosion rates greatly increases for the highest speed cases, ranging by a factor of 1.5 for only a 20% change in θ_c. The lower cases are less sensitive to θ_c, however taking a significantly higher value results in a prediction of no erosion.

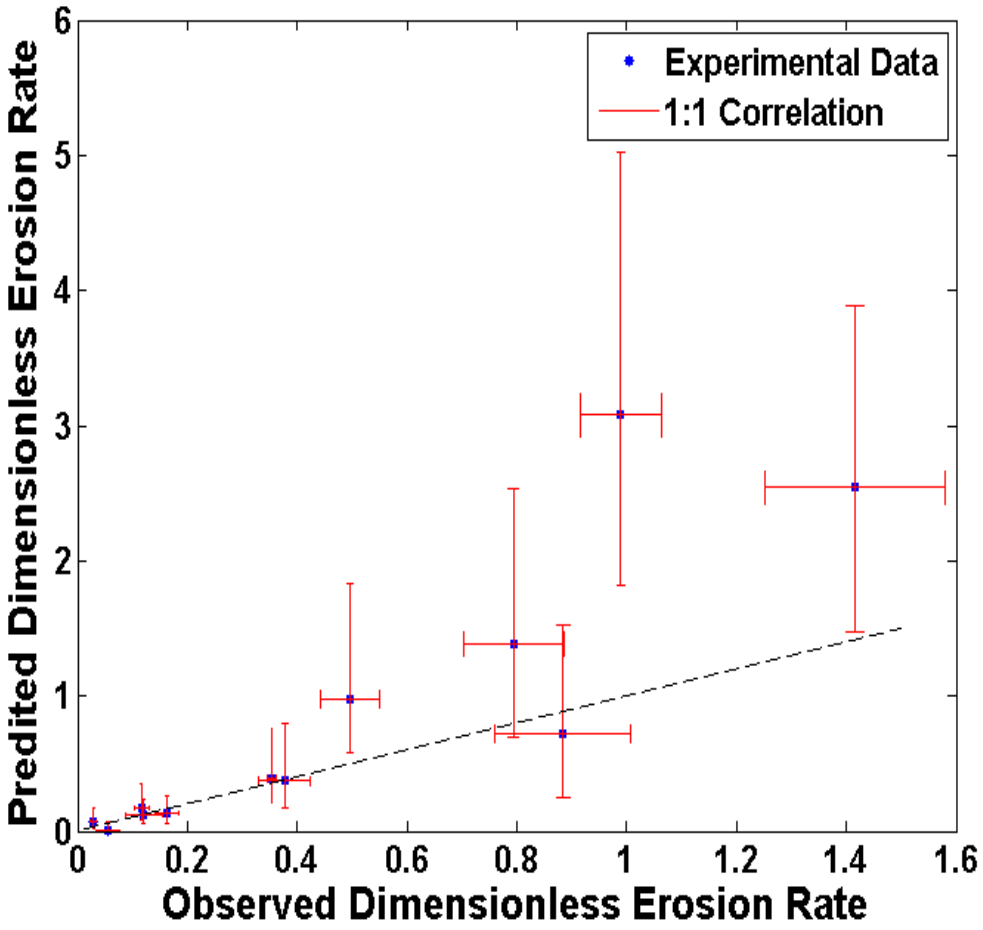

Figure 4.31: Effect of varying θ_c on the predicted erosion rates

The proposed model is compared to some of the models discussed in Chapter 2 (Figure 4.32). It does a better job of predicting the erosion rates for the cases with a lower excess stress, but departs from the observed value for higher speed cases. For these cases the other models perform quite well, however most of them are based on the time-averaged thresholding process and thus predict no erosion for the other cases and contain a similar kink. For these reasons, the proposed model is shown to be a better fit for this unsteady and spatially developing flow, but more work is needed to resolve the prediction of the higher speed cases.

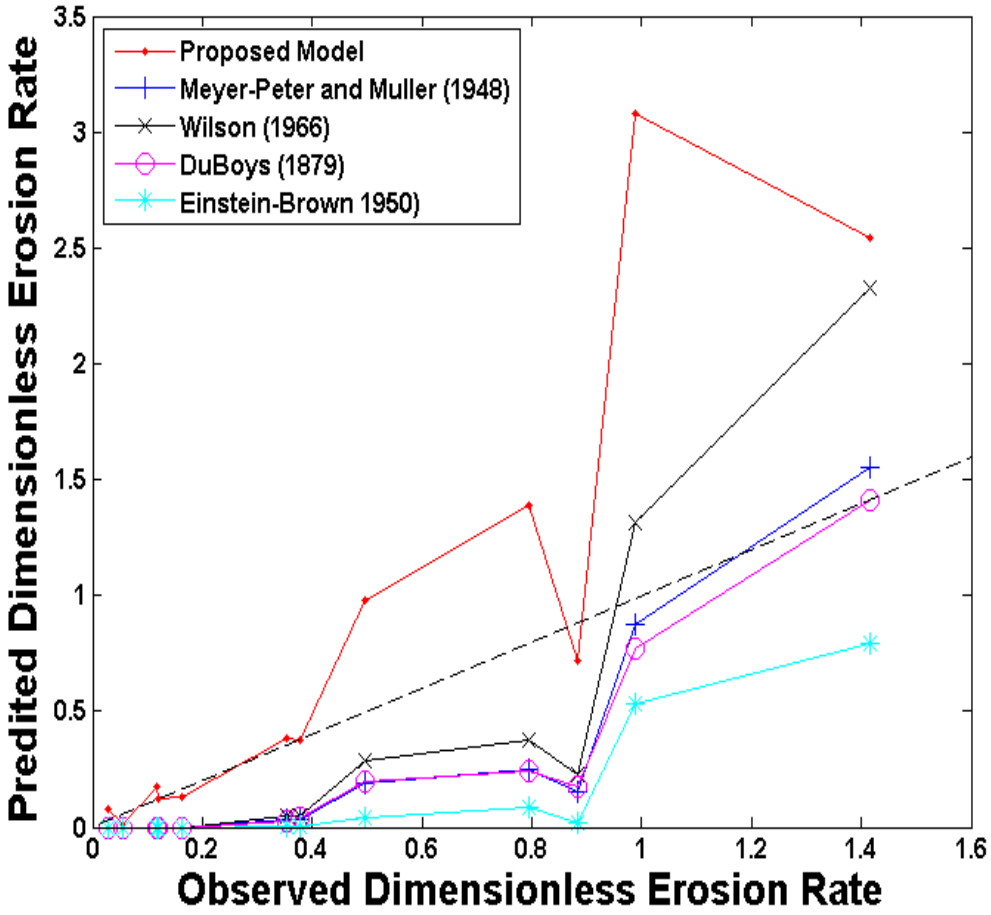

Figure 4.32: Comparison of the proposed model and other classical sediment transport models for predicting the erosion rate

Chapter 5: **Conclusion**

The sediment transport by a series prototype rotorcraft flows were studied to further the understanding of the mechanicisms driving rotorcraft brownout. The prototype flows, ranging in Reynolds number from 1.7 x 10^4 to 3.36 x 10^4, were generated through the acoustic forcing of an impinging jet, providing the basic features of a rotorcraft wake near the ground. Single-phase PIV measurements were used to produce phase-locked planar velocity data, which quantified the stress induced on the surface. The experimental resolution was insufficient to properly calculate the wall stress, so a correction factor was estimated based on an LES simulation of a similar flow. The threshold stress was found experimentally through PIV measurements at a flow condition that was observed to incite motion. A new model was developed, based on the work transport model by Bagnold (1966), for the proper treatment of the thresholding operation used to predict sediment transport. A series of surface elevation profiles were then used to quantify the development of bedforms and to calculate the net erosion rate. This observed rate was used to evaluate the proposed model, as well as other classical models for predicting sediment transport. The data was analyzed to provide to produce several conclusions for the sediment transport.

First, the qualitative features of the single-phase flow were compared to the

resulting evolution of surface bedforms. The self-similar scaling (cases D-F) of the mean flow and the vortex circulation resulted in self-similar kinematics and similar trends in the stress on the wall throughout the vortex/wall interaction, which resulted in similar surface bedform shapes. The scaling of the mean flow with a constant circulation (cases A-C) resulted in a reduced vortex rebound with increasing mean flow velocity due to the increased vortex spacing and reduced velocity induced by the vortex on the wall, which resulted in an increased variability in the bedform wavelenth and shape. The unforced flow although qualitatively similar to the forced flows, showed a reduced circulation and increased variability in trajectory resulting in an increased stress downstream. This was also seen in the resulting bedforms, which developed a significantly deeper second crater.

Second, the augmentation of the flow due to the evolution of the bedforms was found to reduce the vortex rebound, as a result it remained close to the surface throughout the interaction. Although this reduced the peak value of the stress, the bedform caused the stress induced by the vortex/wall interaction to become more unifrom spatially. The increased downstream stress on prototype surface resulted in an increased predicted erosion. This is contrary to erosion measurements which showed a decrease in the erosion rate once the process reaches a quasi-equilibrium state.

Third, the thresholding operation typically used in traditional sediment transport models was found to lead to an under prediction of the stress associated with the periodic or stochastic fluctuations. The proposed model was developed to more accurately account for these fluctuations, by thresholding instantaneously and was

shown to be in good agreement with the observed erosion rates for conditions with stresses close to the threshold. Several physically-based theories were explored to help explain the divergence from the observed values seen at higher flow velocities.

The implications for rotorcraft brownout mitigation techniques illuminated by this study are:

- There is a coupling effect between the tip-vortices and the downwash which results in a repeatable crater shape and erosion rate
- After an initial transient period, the process reaches a quasi-equilibrium state as the crater shape remains nominally similar
- Reducing the circultion of the tip-vortices by forcefully shedding them more frequently may not result in less erosion, as shown by the unforced flow results

The development of the quasi-equilibrium state coupled with the spatial uniformity of the stress on the prototype bedform pose an interesting problem for rotorcraft brownout. In order to provide a better understanding of this process and at what stages in the development the proposed model is valid, several bedforms and crater depths need be tested. Additionally a wider range of particle sizes and flow conditions need to be tested, in order to increase the robustness of the model. To improve the models performance further, a numerical study, with the experimental results as inputs to an unsteady RANS simulation, could be used to calculate the wall stress directly and remove the correction factor.

Appendix A: Propogation of Uncertainty of Velocity Measurements to Vorticity

The vorticity is calculated as the second order finite difference:

$$\frac{\partial U_i}{\partial x_j} \cong \frac{\delta U_i}{\delta x_j} = \frac{U_i(x_j + \delta x_j) - U_i(x_j - \delta x_j)}{2\delta x_j} \tag{5.1}$$

where δx_j is the spacing between two vectors and U_i is the measured velocity. The central differenec method results in a truncation error, which addd to the uncertainty of the reported vorticity. This results in a total uncertainty of:

$$\left| \frac{\partial U_i^*}{\partial x_j} - \frac{\delta U_i}{\delta x_j} \right| = O(\delta x^2) + O(\frac{\Delta U_i}{\delta x_j}) \tag{5.2}$$

where U_i^* is the true velocity and ΔU_i is the uncertainty in the velocity measurement. **?** estimated the value of this truncation error. After accounting for it, the true uncertainty can be expressed as:

$$\Delta \frac{\delta U_i}{\delta x_j} = \frac{\delta x_j^2 \partial^3 U_i}{3! \partial x_j^3} + 0.71 \frac{\Delta U_i}{\delta x_j} \tag{5.3}$$

where the third derivative is approximated by:

$$\frac{\partial^3 U_i}{\partial x_j^3} \cong \frac{\delta^3 U_i}{\delta x_j^3} = \frac{U_i(x_j + 2\delta x_j) - 3U_i(x_j + \delta x_j) + 3U_i x_j - U_i(x_j - \delta x_j)}{\delta x_j^3} \tag{5.4}$$

On average, the truncation error is about 15% of the SEM (2%) and is therefore deemed insignificant to the final reported value of vorticity. The vorticity is calcu-

lated by:

$$\vec{\omega} = \frac{1}{2}\nabla x\vec{U} = \frac{\delta U_j}{\delta x_i} - \frac{\delta U_i}{\delta x_j} \tag{5.5}$$

Leading to an estimate of the error in the vorticity that is:

$$\Delta\vec{\omega} = \Delta\frac{\delta U_i}{\delta x_j}\sqrt{2} \tag{5.6}$$

Appendix B: Surface Elevation Measurements for All Test Conditions

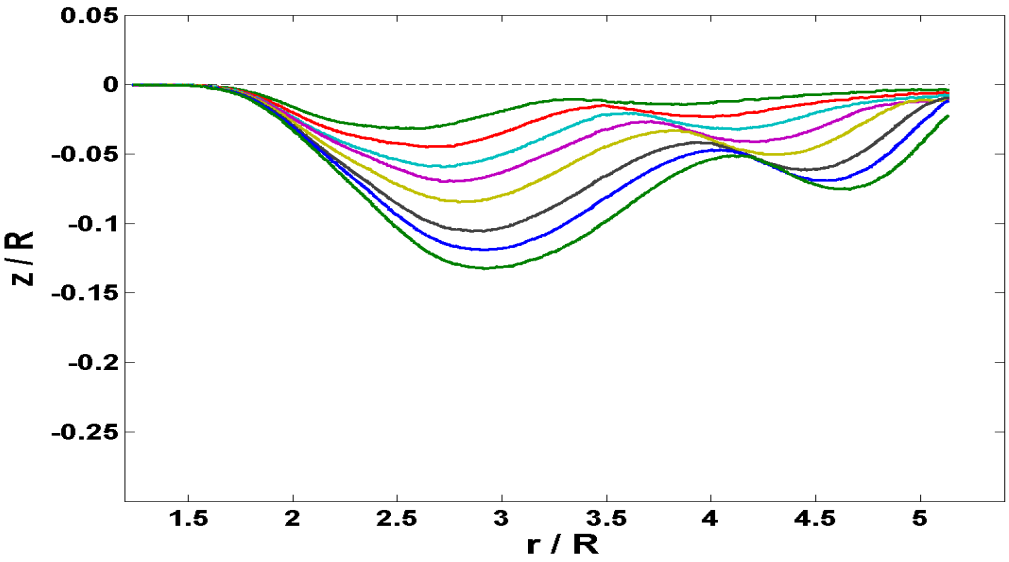

Figure A.1: Mean surface elevation profiles for case SP_A

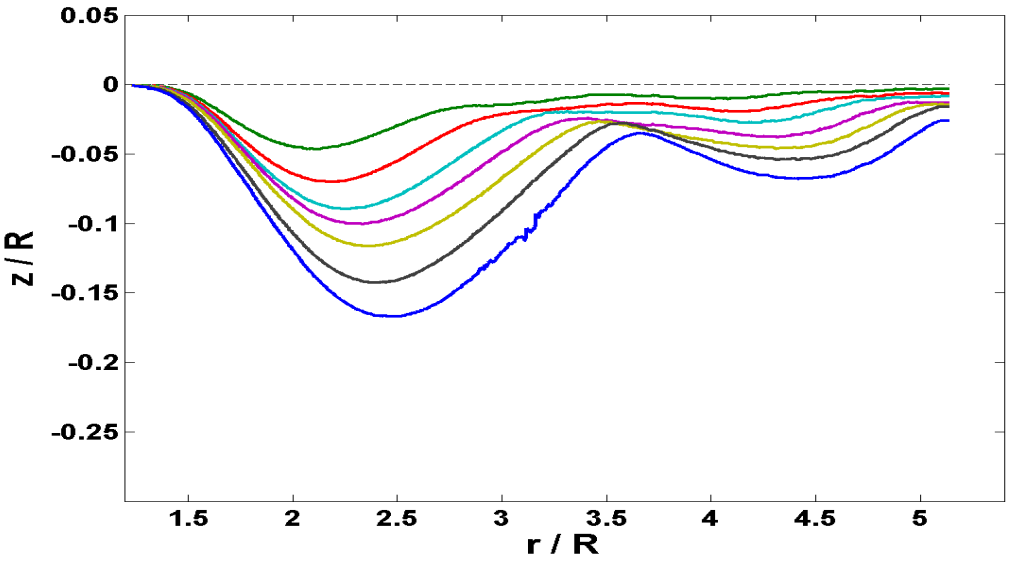

Figure A.2: Mean surface elevation profiles for case SP_B

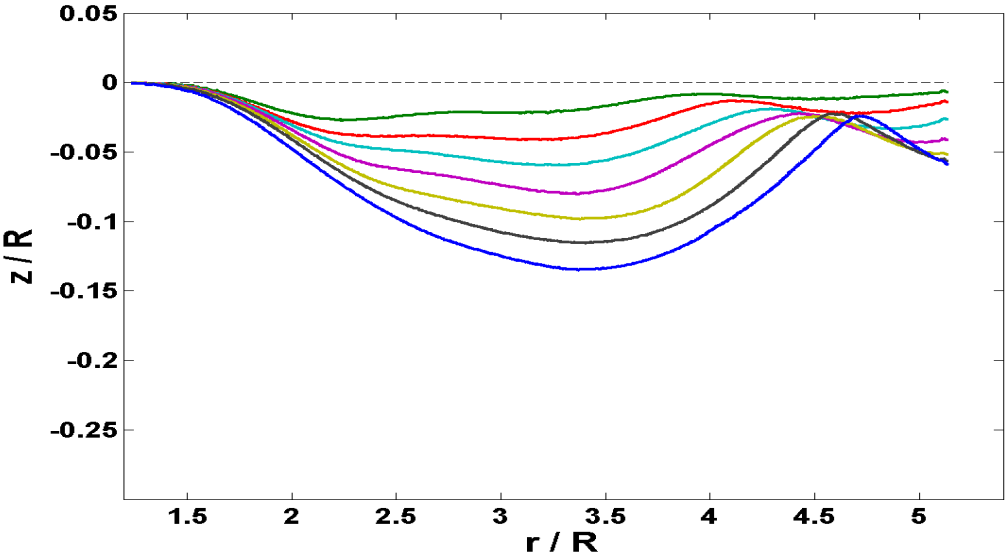

Figure A.3: Mean surface elevation profiles for case SP_C

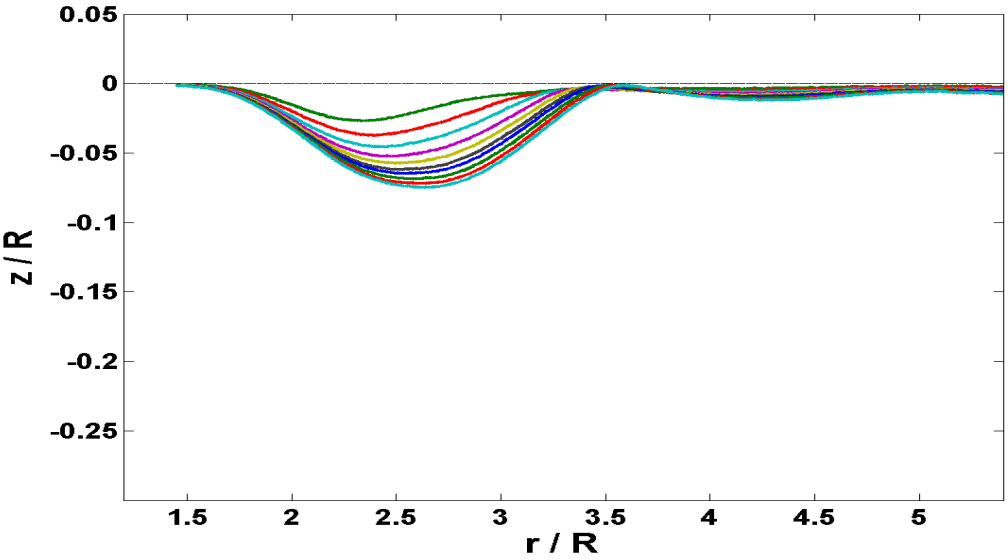

Figure A.4: Mean surface elevation profiles for case SP_D

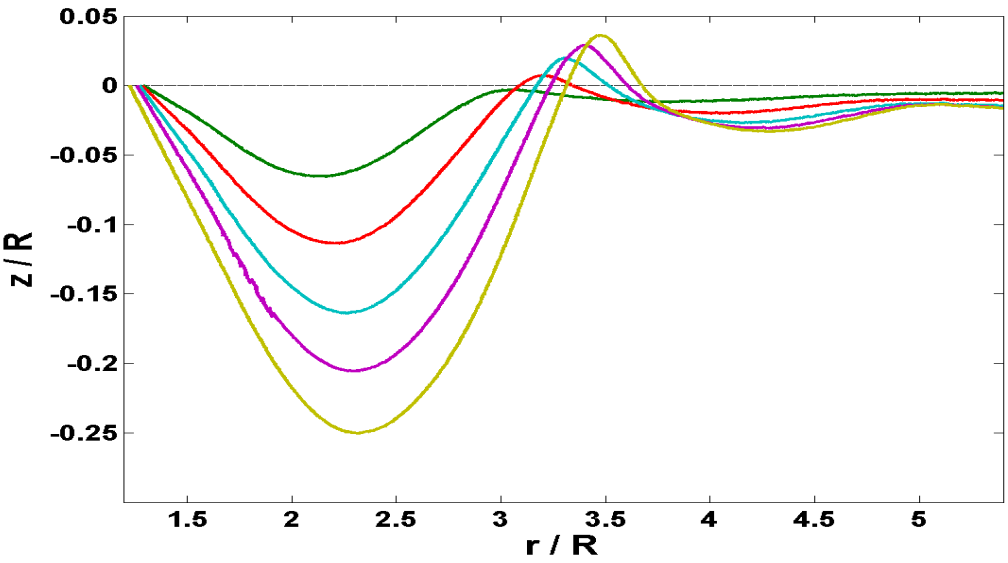

Figure A.5: Mean surface elevation profiles for case SP_E

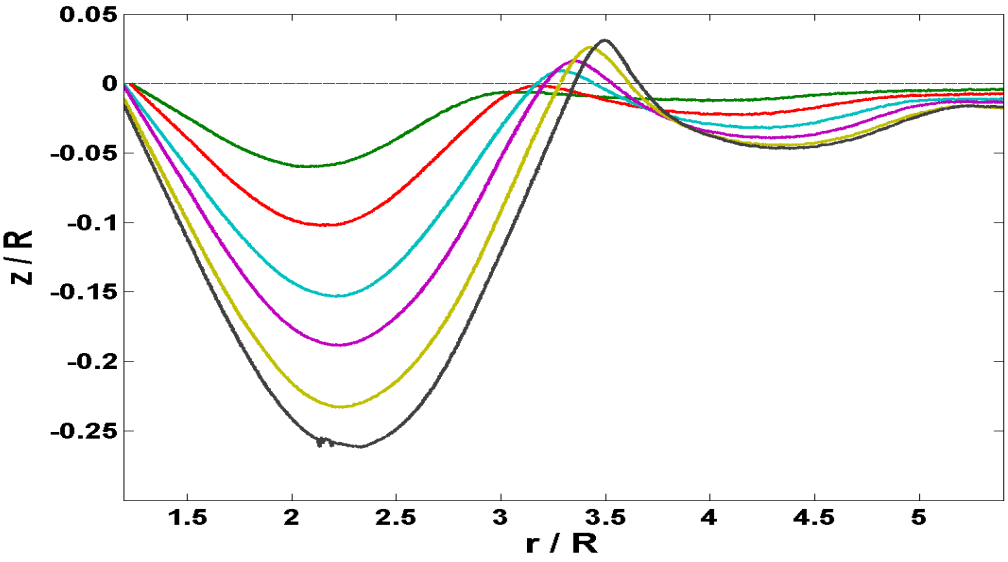

Figure A.6: Mean surface elevation profiles for case SP_F

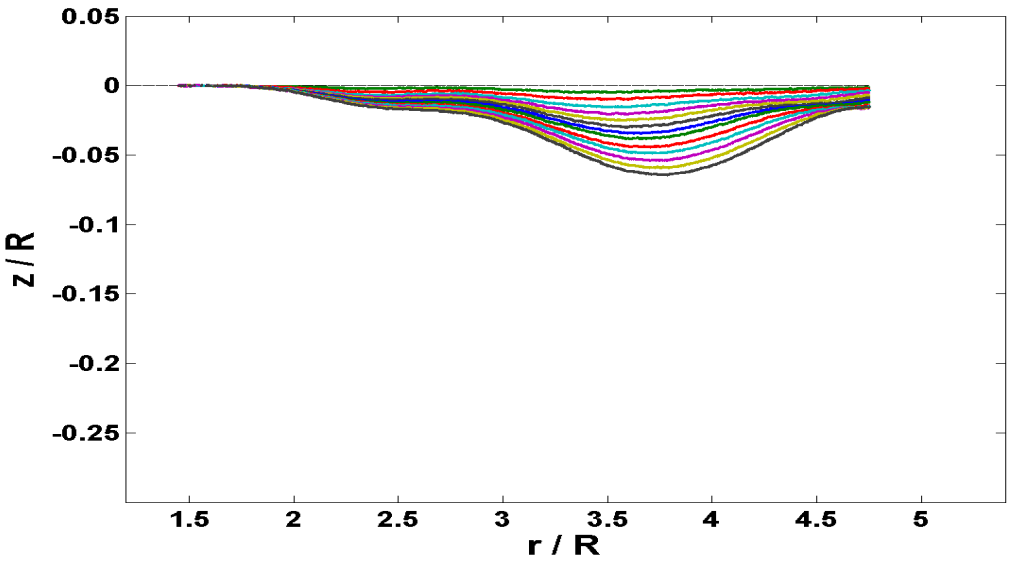

Figure A.7: Mean surface elevation profiles for case SP_{Du}

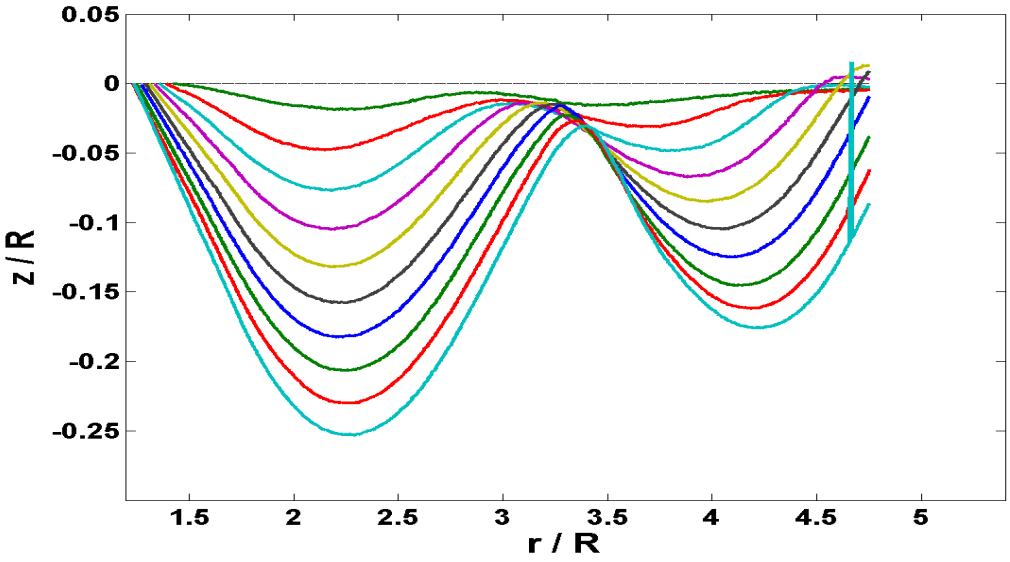

Figure A.8: Mean surface elevation profiles for case SP_{Eu}

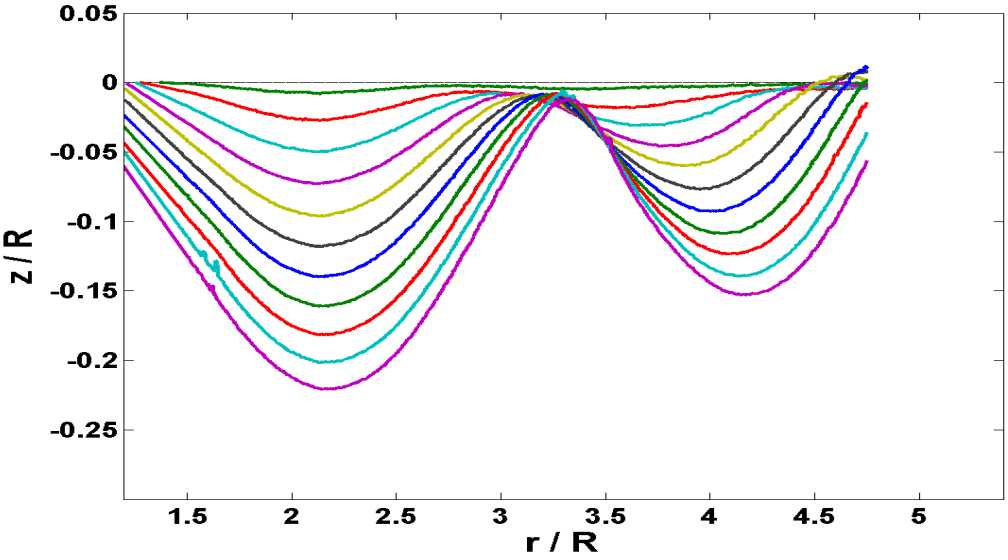

Figure A.9: Mean surface elevation profiles for case SP_{Fu}

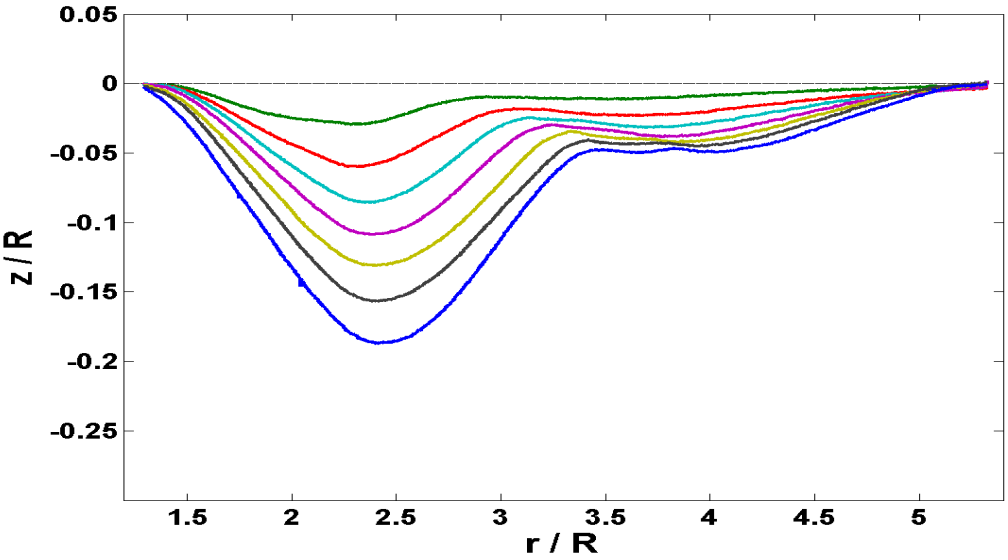

Figure A.10: Mean surface elevation profiles for case LP_E

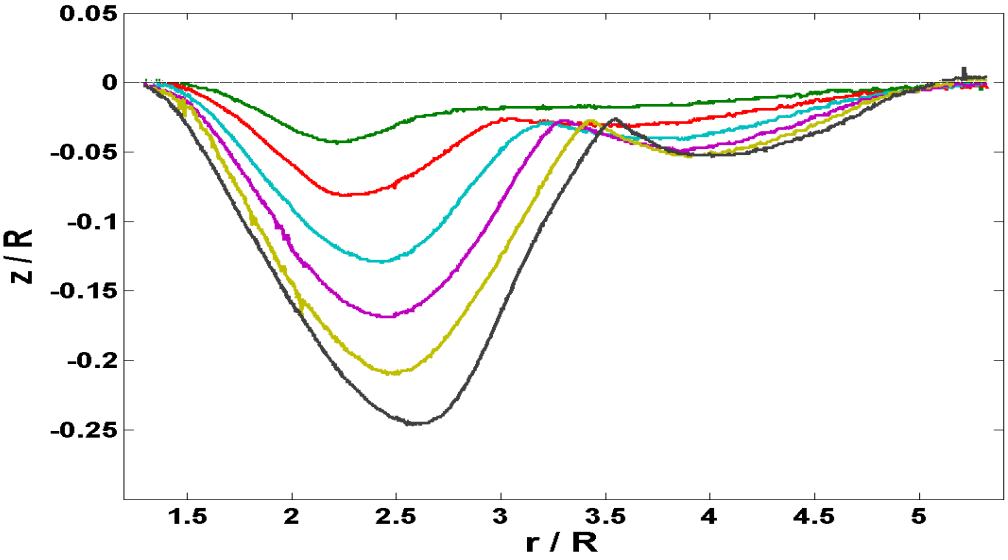

Figure A.11: Mean surface elevation profiles for case LP_F

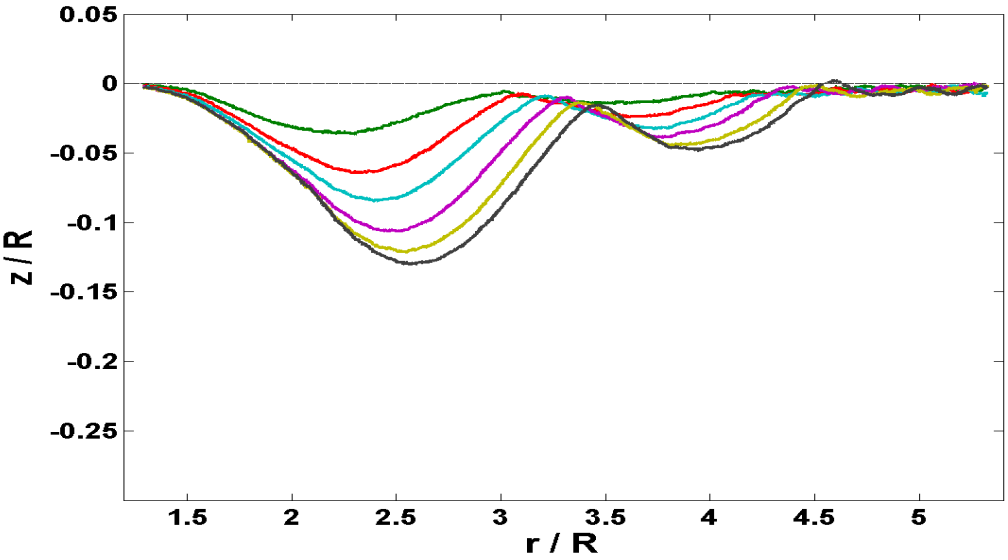

Figure A.12: Mean surface elevation profiles for case MP_E

Bibliography

Amoudry, L. O., Two-Phase Modeling of Granular Sediment for Sheet Flows and Scour, Ph.D. thesis, Cornell University, 2008.

Ayedimer, E. *et al.*, "The formation of vortex rings in a strongly forced round jet," Experiments in Fluids, 2010, pp. DOI 10.1007/s00,348–011–1110–6.

Bagnold, R. A., "An approach to the sediment transport problem from general physics," Geological Survey Professional Paper, 1966, pp. 422–I.

Bagnold, R. A., Physics of Blown Sand and Desert Dunes, Dover Publications, 2005.

Bethke, N. and Dalziel, S. B., "Resuspension onset and crater erosion by a vortex ring interacting with a particle layer," Physics of Fluids, Vol. 24, 2012, p. 063,301.

Brown, C. B., "Sediment transportation," Engineering Hydraulics.

Brown, R. E. and Houston, S. S., "Modeling rotor wakes in ground effect," Journal of the American Helicopter Society, Vol. 49, 2004, pp. 238–249.

Couch, M. and Lindell, D., "Study on rotorcraft safety and survivability," Proceedings of the American Helicopter 66t̂h Annual Forum, Phoenix, Arizona, 2010, pp. 1–10.

DuBoys, M. P., "Le rhone et les rivieres a lit affouillable," Annales de Ponts et Chausses, Vol. 18, 1879, pp. 141–195.

Durán, P., O. Claudin and Andreotti, B., "Review article on aeolian transport: Grain-scale interactions, dynamical mechanisms, and scaling laws," Aeolian Research, 2011, pp. 243–270.

Einstein, H. A., "Formulation for the transportation of the bed-load," Transactions of the ASCE, Vol. 107.

Johnson, B. *et al.*, "Investigation of sediment entrainment using dual-phase, high-speed particle imaging velocimetry," Journal of American Helicopter Society.

Julien, P. Y., Erosion and Sedimentation, Cambridge University Press, New York, 1995.

Kahler, C. J., Sammier, B., and Kompenhans, J., "Generation and control of tracer particles for optical flow investigations in air," Experiments in Fluids, Vol. 33, 2002, pp. 736–742.

Kiger, K., Mulinti, R., and Corfman, K., "Effect of bed form evolution on sediment erosion and suspended load transport in an impinging jet," Proceedings of the 17th Annual International Symposium on Applications of Laser Techniques Lisbon, Portugal, 2014, pp. 7–10.

LaVision, Product Manual for DaVis FlowMaster Software 7.2, Lavision GmbH, Göttingen, Germany, 2007.

Leishman, J. G., "Rotorcraft brownout: Advanced understanding, control, and mitigation," DTIC Document.

Meyer-Peter, E. and Müller, R., "Formula for bed-load transport," Proceedings of International Association of Hydraulics Research, 2nd meeting, Stockholm, Sweden, 1948, p. 1135.

Morel, T., "Comprehensive design of asixsymmetric wind tunnel contractions," Journal of Fluids Engineering, Vol. 97, 1975, pp. 225–233.

Morrison, A. F., An Introduction to Fluid Mechanics, Cambridge University Press, New York, 2013.

Munro, R. *et al.*, "Sediment resuspension and erosion by vortex rings," Journal of Fluid Mechanics, Vol. 21, 2009, p. 046,601.

Nairn, B. J., Incipient Transport of Silt-Sized Sediments, Ph.D. thesis, California Insititute of Technology, 1998.

Nepf, M. H., "Hydrodynamics of vegetated channels," Journal of Hydraulic Research, Vol. 50, 2012, pp. 262–279.

Shields, A., "Anwendung der ahnlichkeitsmechanik und turbulenz forschung auf die gescgiebebewegung," Mitteil. Preuess. Versuchsnasnt. Wasser, Schiffsbau, Berlin, 1936, p. Nr. 26.

Straub, L. G., "Missouri river report," 73rd congress, 2nd session, Washington, D.C., 1935, p. 1135.

Sutherland, J. A., "Proposed mechanism for sediment entrainment by turbulent flows," Journal of Geophysics Research, Vol. 72, 1967, pp. 61–83.

Syal, M., "Development of lagrangian-lagrangian methodology to predict brownout dust clouds," PhD Dissertaion, University of Maryland.

White, C. M., "The equilibrium of grains on the bed of a stream," Proceedings of the Royal Society of London. Series A, Mathematical and Physical Sciences, London, England, 1940, pp. 322–338.

Widberg, L. P. and Smith, D. J., "Calculations of the critical shear stress for motion of uniform and heterogeneous sediments," Water Resources Research, 1987, pp. 1471–1480.

Wiggs, G. *et al.*, "Thresholds of aeolian sand transport: Establishment of suitable values," Journal of Sedimentology, Vol. 51, 2004, pp. 95–108.

Wilson, K. C., "Bed-load transport at high shear stress," Journal of the Hydraulics Division, Vol. 92(HY6), 1966, pp. 49–59.

Wu, W. and Piomelli, U., "Large-eddy simulation of impinging jet with embedded azimuthal vortices," Journal of Turbulence, Vol. 16:1, 2015, pp. 44–66.